Ph.D. Thesis

Mohamed Fathy Hasaneen

Budapest
2013

Effect of Oxygen Doping on Titanium Nitride Thin Films Prepared by Reactive Unbalanced Magnetron Sputtering

Ph.D. Thesis

Mohamed Fathy Hasaneen

Doctoral School of Physics
Head: Prof. László Palla

Doctoral Program of Material Science and Solid State Physics
Head: Prof. János Lendvai

Supervisor Prof. Péter B. Barna

Hungarian Academy of Sciences
Research Centre for Natural Sciences
Institute for Technical Physics and Materials Science

Eötvös Loránd Tudományegyetem

BUDAPEST

2013

Contents *Pages*

	Abstract	1
	Introduction	3
Chapter 1	***Fundamentals of thin films growth***	7
1.1.	Introduction	7
1.2.	Nucleation	8
1.2.1.	Orientation of nuclei	10
1.3.	Crystal growth	11
1.3.1.	Growth of individual single crystalline the substrate	11
1.3.2.	Growth of crystals as a parts of a polycrystalline matrix	12
1.4.	Grain growth	13
1.4.1.	Grain growth in the coalescence stage	13
1.5.	References	16
Chapter 2	***Structure zone models(SZM)***	19
2.1.	Introduction	19
2.2.	The Structure Zone Model	20
2.2.1.	Derived temperature structure zone model (TSZM) of elemental, high purity films	20
2.2.2	Structure Zone Models of multicomponent and multiphase films	26
2.2.3	Compositional structure zone model	29
2.2.4	3-D inclusion developed in co-deposited films	31
2.3.	References	33
Chapter 3	***Experimental methods***	35
3.1	Introduction	35
3.2.	Thin film deposition methods	35
3.2.1.	Thermal evaporation technique	37
3.2.2.	Molecular Beam Epitaxial (MBE) technique	37
3.2.3.	Electron beam gun evaporation technique	38
3.2.4.	Pulsed Laser Deposition (PLD)	38
3.2.5.	Sputter system	38
3.2.5.1.	Principle of sputtering source operation	38
3.2.5.2.	Sputtering yield	39
3.2.5.3.	Processes at the target	40
3.2.5.4.	Magnetron sputtering	41

3.2.5.4.1.	Unbalanced magnetron sputtering	42
3.2.5.5.	Reactive sputter deposition	42
3.3.	X-ray diffraction	44
3.3.1.	Basic operation	44
3.3.2.	Bragg-Brentano (θ-2θ) geometry	45
3.3.3.	Grain size estimation	46
3.3.4.	Determination of texture X-ray diffraction	46
3.3.5.	Pole figure	48
3.4.	Transmission Electron Microscopy (TEM) for thin film for microstructure analysis	49
3.5.	Precession electron diffraction PED-ASTAR technique	50
3.6.	Principle of operation of Ultra micro –indentation system (UMIS)	52
3.7.	Atomic force microscopy (AFM)	55
3.8.	Auger electron spectroscopy	55
3.9.	X-ray photoelectron spectroscopy (XPS)	56
3.9.1.	Depth profiling using AES and XPS	57
3.10.	References	58
Chapter 4	***Literature survey***	63
4.1.	Motivation of the present work	63
4.1.1.	Effect of substrate temperature on structure evolution of TiN thin film	63
4.1.2.	Effect of substrate bias on structure evolution of TiN thin film	64
4.1.3.	Effect of oxygen doping on structure evolution of TiN thin film	65
4.2.	Motivation and the main aim of the present work	68
4.3.	References	70
Chapter 5	***Experimental results***	75
5.1.	Thin film preparation and measurements	75
5.2.	Structure of undoped Titanium nitride (TiN) thin film (sample TO_4)	77
5.2.1.	X-ray diffraction	77
5.2.2.	ProcessDifraction analysis of SAED	78
5.2.3.	X-ray photoelectron spectroscopy (XPS) and Auger electron spectroscopy (AES) analysis	79
5.2.4.	Cross section transmission electron microscopy (X-TEM)	80
5.2.5.	Nanoidentation measurements	82
5.3.	Structure of oxygen doped $Ti_{0.45}O_{0.20}N_{0.35}$ thin film (sample TO_12)	83
5.3.1.	X-ray diffraction	83

5.3.2.	X-ray photoelectron spectroscopy(XPS) and Auger electron spectroscopy (AES) analysis	84
5.3.3.	Determination of phase composition by 'ProcessionDiffraction' analysis of SAED	86
5.3.4.	Cross section transmission electron microscopy for oxygen doped $Ti_{0.45}O_{0.20}N_{0.35}$ oxynitride film	87
5.3.5.	Precession electron diffraction analysis for oxygen doped $Ti_{0.45}O_{0.20}N_{0.35}$ oxynitride film	88
5.3.6.	Nanoidentation measurements	90
5.4.	Substructure in the columnar crystals of the $Ti_{0.45}O_{0.20}N_{0.35}$ oxynitride thin film	90
5.5.	Oxynitride film prepared at varying oxygen concentration (TO_11)	95
5.5.1.	X-ray diffraction	95
5.5.2.	Cross section transmission electron microscopy for oxynitride films prepared at varying oxygen concentration	96
5.5.3.	X-ray photoelectron spectroscopy(XPS) and Auger electron spectroscopy (AES) analysis	99
5.5.4.	Precession electron diffraction analysis of oxynitride film prepared at varying oxygen concentration	99
5.5.5.	Nanoidentation measurements	100
5.6.	Reference	101
Chapter 6	***Discussion***	103
6.1.	In which states (phases) is the oxygen incorporated in to the film with 001 texture?	104
6.2.	What is the characteristics of the microstructure of the <001> oriented film making possible to select between the mechanisms of texture evolution?	105
6.3.	What are the specific structural characteristics of the <001> oriented film which could be used at considering the possible growth mechanisms?	108
6.4.	What is the real structure of the film deposited at varied oxygen concentration having a crossover between the 001 and 111 textures?	109
6.5.	References	112
Chapter 7	***Conclusion and new scientific results***	115
7.1.	Summary of the results	115

7.2.	New scientific results	117
7.3	Publication of our results	118
7.3.1	Scientific papers	118
7.3.2	Lecture presented at conferences	119
Acknowledgements		121

ABSTRACT

TiN thin films have a broad range of application. Oxygen is used as a doping material to develop oxinitride, but it can also affect the structure evolution as unintentional contaminant. In the present study the effect of the oxygen doping on the structure evolution of TiN films deposited by unbalanced magnetron sputtering on oxidized Si wafers was investigated. The films were prepared at 400˚C substrate temperature and $3x10^{-1}$Pa argon-nitrogen atmosphere. Admission of oxygen gas was manually controlled by using a high precision needle valve. The microstructure was investigated by θ-2θ XRD, bright and dark field transmission electron microscopy (TEM) and selected area electron diffraction (SAED), the chemical composition by EDS and XPS applying also depth profiling. The V-shaped columnar morphology as well as the development of the textures was demonstrated at first by PED-ASTAR technique in the TEM. At oxygen doping lower than 15at.% the 111 texture dominated which turned to 001 texture beyond 15at.%. It has been shown that both the 111 and 001 textures are developing by competitive crystal growth. Terminating the high level oxygen doping (20at.%) during the film deposition the growth of <001> oriented crystals became limited and the growth of <111> oriented ones became promoted developing a crossover between the two textures. The pathway of this structure evolution is discussed in details.

Introduction

Background

Titanium Nitride (TiN) is one of the most widely applied surface coatings. TiN coatings are generally prepared by PVD (Physical Vapor Deposition) techniques. The structural and morphological properties of TiN films depend mainly on the preparation parameters and type of contamination which can be incorporated during the film growth, such as Oxygen. Veprek has shown that a minute amount of Oxygen contamination hinders the formation of stable nanostructure during the thin film growth ***[Veprek, 2011].*** Wu et al (2008) pointed out that at oxygen contamination beyond 15at.% the 111 texture is changing to 001 ***[Wu et al, 2008].*** On the other hand, Oxygen is used as additive to prepare oxynitride thin films. Therefore, it is important to understand the detrimental role of oxygen contamination in the structure evolution.

Objective

The aim of this work is to follow the effect of oxygen additive on the structure and the texture evolution in TiN films deposited by reactive unbalanced magnetron sputtering. Experiments were carried out in the 0 < 20 at.% Oxygen contamination range. The structure and structure evolution were investigated in details both in undoped films and in films with 20 at.% oxygen content to be able to understand the influence of oxygen on the fundemental phenomena of film growth and to propose a pathway of the structure evolution of oxynitride thin films of 001 texture.

For realizing a more comprehensive characterization of the film structure various methods were applied:

1. Cross-section (X-TEM), plane view transmission electron microscopy and selected area diffraction (SAED),
2. PED-ASTAR techinque,
3. Energy dispersive X-ray microanalysis (EDX),
4. X-ray diffraction (XRD)
5. Auger (AES) and X-ray photoemission spectroscopy (XPS),

6. Atomic force microscopy (AFM),
7. Ultra-Micro-Indentation system (UMIS),
8. ProcessDiffraction computer program.

The thesis is built up in the following chapters:

Chapter 1: Explains the fundamentals of thin film growth such as nucleation, crystal growth, and grain growth.

Chapter 2: Gives a survey of the previous literature on structure zone models (SZM).The role of the contamination and temperature will be explained on this model.

Chapter 3: Describes the applied experimental methods (sample pereperation, and invistigation methods).

Chapter 4: Will review only some selected publications discussing the effect of oxygen contamination, substrate temperature and substrate bias - as the most important parameters - on the structure and structure evolution of TiN thin films and to show why I have selected to study the effect of oxygen.

Chapter 5: In this chapter we will explain the methods which are used in the thin film preparation (by more details) and summarize the experimental results.

Chapter 6: In this chapter we will explain the effect of varying the oxygen contamination on the mechanism of texture change

Chapter 7: Contains a summary of the main results presented in this thesis

References

Veprek S., Recent attempts to design new super-and ultrahard solids leads to nano-sized and nano-structured materials and coatings, Journal of Nanoscience and Nanotechnology, 11(2011)14–35.

Wu Y., Wu X., Li G. and Li G., Microstructure and mechanical properties of reactively sputtered Ti (O, N) coatings, International Journal of Refractory Metals and Hard Materials, 26(2008)461-464.

Chapter 1

Fundamentals of thin film growth

1.1. Introduction

Growth of thin films, as all phase transformation, involves the process of nucleation and growth on the substrate or growth surface. The nucleation process plays an important role in determining the crystallinity and microstructure of the resultant film. For the deposition of thin films with thickness in the nanometer region, the initial nucleation process is even more important. The size and shape of the initial nuclei are assumed to be solely dependent on the change of Gibbs free energy, due to supersaturation, and on the combined effect of surface and interface energies governed by Young's equations ***[Tadmor, 2004].*** No other interaction between the film or nuclei and substrate were taken into consideration. In practices, the interaction between film and substrate plays a very important role in determining the initial nucleation and film growth. On substrates there are three modes of film growth related to the ad-atom and surface interaction as shown in Figure 1.1 ***[Venables et al, 1984], [Greene, 2010]:***

- Volmer-Weber (VW) growth takes place when ad-atom-ad-atom interactions are stronger than those of the ad-atom with the surface, leading to the formation of three-dimensional ad-atom clusters or islands ***[Oura et al, 2003], [Pimpinelli and Villain, 1998].*** That is the case for metal films deposited on insulators or contaminated single crystal surfaces. Film growth can start both by randomly oriented or epitaxially grown nuclei depending on the kind of substrate and deposition temperature (Figure 1.1a).
- In case of Frank-Vander growth the interaction between ad-atoms and substrate surface is stronger than the ad-atom ad-atom interaction- consequently the nuclei are growing in monolayer islands. This will result in a layer by layer growth mode of the film indicating that a complete monolayer forms prior to the nucleation and growth of the subsequent layers (Figure1.1b). The growth of many amorphous layers can be considered as such growth modes.
- Stranski–Krastanov (SK) growth is an intermediary process characterized by both 2D layer and 3D island growth. Transition from the layer-by-layer to

island-based growth occurs at a critical layer thickness which is highly dependent on the chemical and physical properties, such as surface energies and lattice parameters, of the substrate and film (Figure 1.1c) ***[Venables, 2000].***

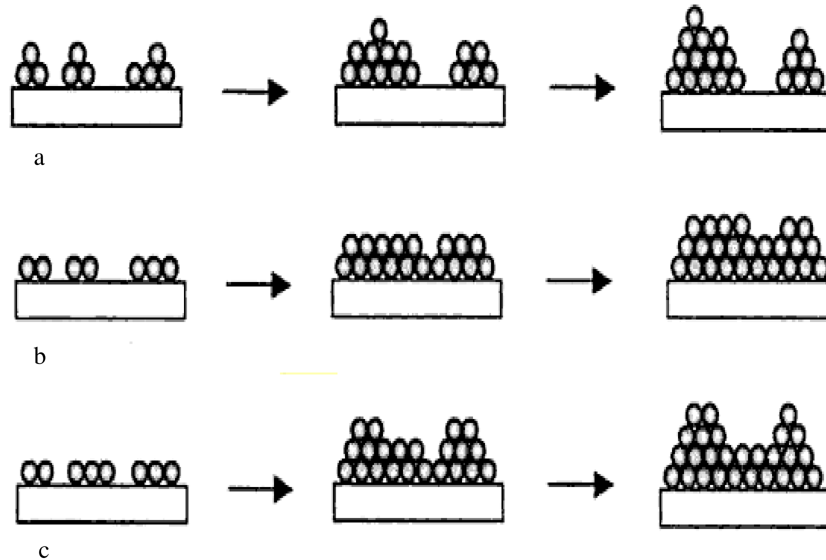

Figure 1.1. Schematic illustrating three basic modes of initial nucleation in the film growth ***[Guozhong, 2004]****.*

1.2. Nucleation

In the beginning the impinging ad-atoms hits the clean substrate surface and as you can imagine, one or more of the following behaviors will be happen as shown in Figure 1.2:

- The ad-atoms can be reflected from the surface and then runs away to infinity.
- The ad-atom can be reflected but then hits an incoming ad-atom and is redirected to the substrate surface.
- The ad-atoms can be sticked and migrate along substrate surface until the density of ad-atoms are high enough, and then ad-atoms can join together to form the nuclei. This process is called "primary nucleation".

The nucleation initiates the growth of a condensed phase on a foreign material surface. The number density of nuclei increases in time up-to the saturation density determined by the adsorption energy, deposition rate and by the substrate temperature. That is the number density of nuclei at which the collection areas of the individual

nuclei start to overlap. The nucleation is controlled by the structure and chemical properties of the substrate surface (structural preconditions). The distribution of nuclei is statistical and homogenous if the adsorption energy is the same over the surface. Sites of higher or lower binding energy (embedded foreign atoms or defects in crystal lattice, monolayer steps, GBs) or surface domains with different binding energy (as bulk or surface segregates, contamination) modify the nucleation density, shape and orientation of crystals locally.

Nucleation on a foreign substrate is a short term phenomenon and can take place in various stages of polycrystalline film growth.

- Primary nucleation is the initial formation of crystals where there are no other crystals present (Figure 1.2) i.e. at the very beginning of film deposition.
- Secondary nucleation takes place in the coalescence stage of film growth on the open substrate surface area developing during the fast, liquid-like coalescence of the impinging neighbor individual crystals or polycrystalline islands (Figure 1.3).
- Repeated nucleation continues the growth of an already existing phase when its crystals have been encapsulated by the layer of a second (e.g. tissue) phase surface covering layers, SCL (Figure 1.4).

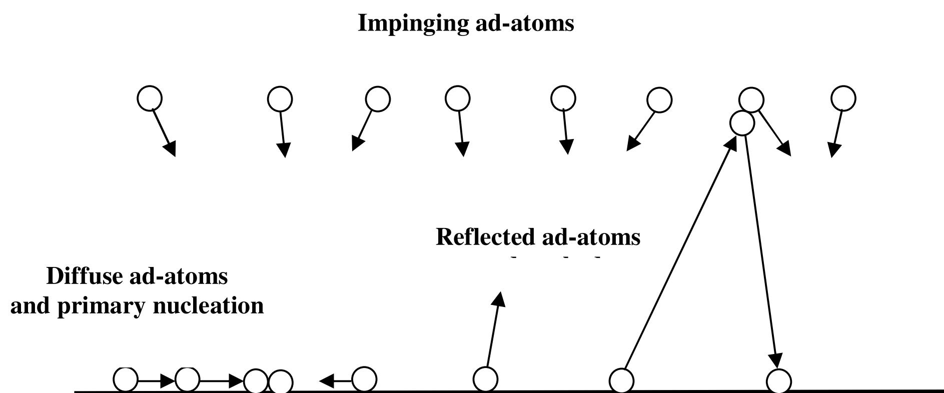

Figure 1.2. The possible behavior for impinging ad-atoms on substrate surface.

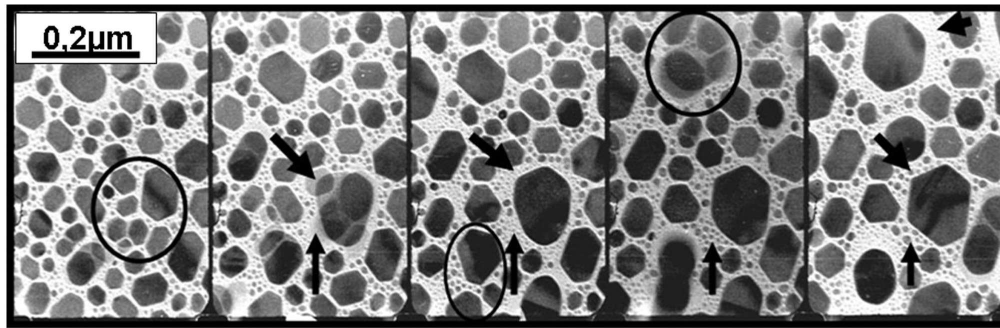

Figure 1.3. Plane view TEM micrographs illustrating the secondary nucleation on the denuded surface area (marked by arrows) developed after the liquid-like coalescence of In crystals. Contours of crystals before and after the coalescence and the fast recovering of the faceted crystal shape after the coalescence are clearly shown. Frames of a cine film showing the growth of an In film deposited on a-C layer at 330 K substrate temperature ***[Pócza, 1967].***

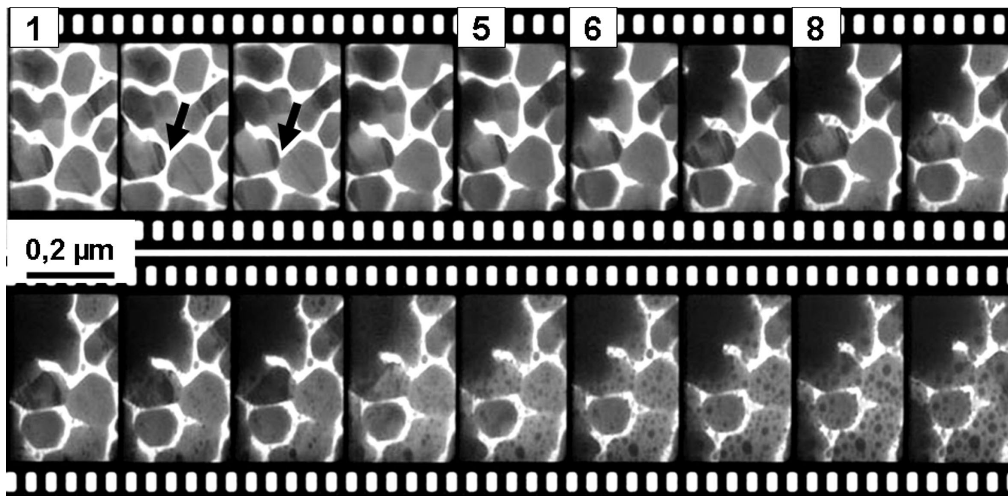

Figure 1.4. Section of the cine film illustrating the incomplete coalescence of contacting crystals due to the carbon SCL marked by arrows (frames 1-5) and the gradual encapsulation of the growing In crystals by carbon layer and repeated nucleation of In starting at frame 8. Co-deposition of In and carbon at $T_S = 0.8T_m$ ***[Barna et al, 1967].***

1.2.1. Orientation of nuclei

Crystalline nuclei forming on amorphous substrates are randomly oriented ***[Pócza et al, 1969], [Thompson and Carel, 1995]*** while on crystalline substrates they are coherent with two axis texture beyond the epitaxial temperature. Below but near to

the epitaxial temperature nuclei can be partly oriented in two axis texture or in fiber texture. Axiotaxy ***[Detavernier et al, 2003]*** can also develop.

1.3. Crystal growth

The ad-atoms condensing directly from the vapor and by the flux of ad-atoms adsorbed on the bare substrate and diffusing to the nuclei contribute to the growth of crystals (Figure 1.5). The crystal growth proceeds by re-entrant nucleation and growth of monolayers on the crystal faces. The most active sites of binding-incorporating the ad-atoms are the monolayer steps. Because the surface energy of the various crystal faces and the adsorption energy of ad-atoms on them is different, the rate of monolayer nucleation and their growth rates are also different. Crystal growth develops faceted crystal forms in every stages of film growth in case of strictly elemental or mono-phase (clean) thin films. Two main cases of crystal growth are to be considered. The growth of individual single crystals situated on a substrate (Figures 1.6 a and b) and the growth of crystals as parts of an already developed polycrystalline matrix (Figures 1.6c and d).

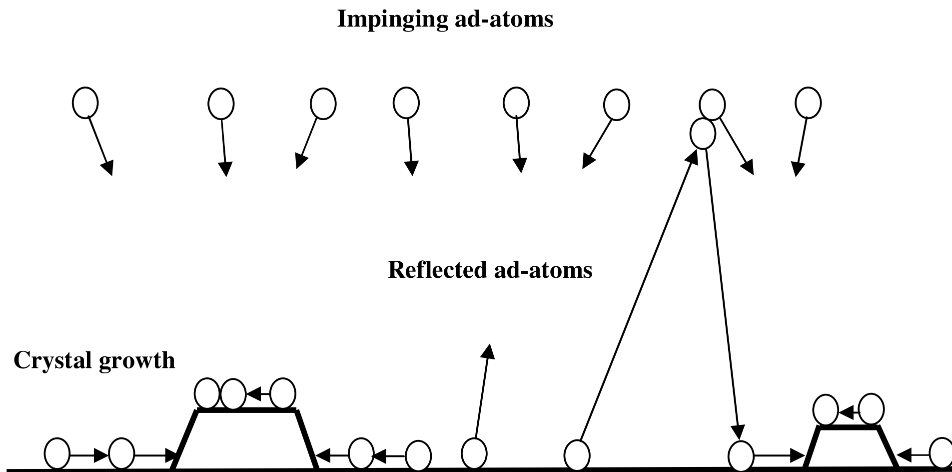

Figure 1.5. Growth phenomena of individual crystals dispersed on the substrate.

1.3.1. Growth of individual single crystals on the substrate

In the early stages of film growth the nucleation is followed by the growth of discrete faceted single crystals dispersed on the substrate. Individual single crystals develop also by the complete coalescence in the later stages of film growth as shown

in Figure 1.3. The intersection lines of the crystal side faces and the substrate present a structure precondition specific for the growth of these crystals. The intersection lines can be active or passive in the monolayer nucleation on the side crystal faces. In the first case, the movement of the monolayer growth steps proceeds from the intersection line to the top of the crystal as shown in Figure1.6a, while in the second case, the movement of the growth steps proceeds to the direction of the intersection line as shown in Figure 1.6 b ***[Barna and Adamik 1998].***

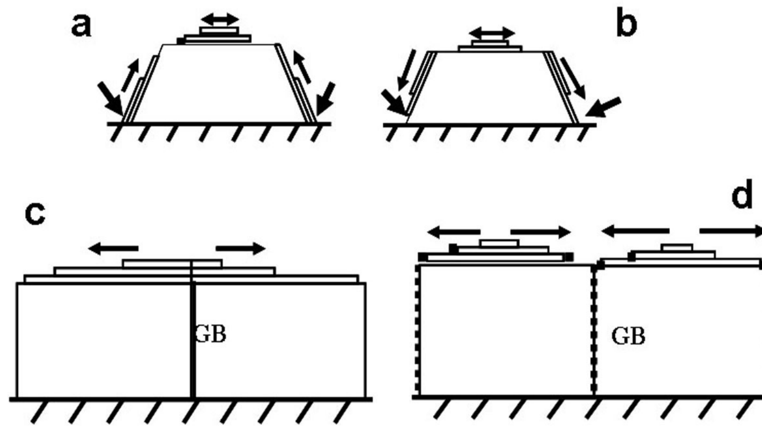

Figure 1.6. Two main types of crystal growth taking place during the deposition of polycrystalline thin films and related preferential sites of monolayer nucleation: a) and b) individual crystals situated on the substrate: intersection lines between substrate and crystal faces are active (a) or passive (b) in the monolayer nucleation; c) and d): role of grain boundaries in the growth of neighbor crystals in a polycrystalline matrix: pure GB is active in the monolayer nucleation (c), contaminated GB is passive in the monolayer nucleation (d) ***[Barna and Adamik 1998].***

1.3.2. Growth of crystals as parts of a polycrystalline matrix

When a crystal becomes part of a polycrystalline structure, it might have various sizes and orientations as well as surface conditions. Formation of polycrystalline islands by incomplete coalescence, percolation of islands and filling up of the channel results in the development of a continuous film with polycrystalline structure. It is important to recognize that the surface structure (type and orientation of crystal faces building the surface plane of the film, the structure and purity of GBs, the presence of SCL) of this continuous film is related to the bulk and surface

structure of the film developed by the precedent growth phenomena. These are the structural preconditions which control the pathway of atomic processes and fundamental phenomena in the next thickness growth regime. Thickness growth means the interdependent growth of the neighbour crystals and a possible restructuring (grain growth) in the bulk (Figures 1.6 c and d). The bulk restructuring results also in the restructuring of the surface. Dependence of the interdependent growth of crystal on the surface structure is discussed in details in chapter 2.

1.4. Grain growth

At high substrate temperature ($T_s > 0.3T_m$) the grain growth related to the movement of the boundary separating the grains. The GB movement takes place by the diffusion of single atoms from one grain across the boundary to the other grain. This motion results in the migration of the boundary in the opposite direction to the diffusion direction. During the structure evolution two types of grain growth take place. At first, in the coalescence stage, the grain growth is realized in the complete coalescence of the neighbor single crystal islands. In later stages of film growth the grain coarsening takes place in the bulk of already developed polycrystalline islands or in the continuous film by GB motion as abnormal or normal grain growth ***[Thompson, 1990], [Frost, 1994].***

1.4.1. Grain growth in the coalescence stage

The coalescence sets in when the growing crystals will touch each other. This is the grain growth phenomenon discussed by the sintering phenomenon ***[Pashley, 1964], [Pashley, 1975] [Barna, 1992], [Barna and Adamik, 1996].*** Accordingly, the main processes of coalescence are: (i) the neck formation, (ii) filling the necks by surface self-diffusion, (iii) formation of intergranular structure (grain boundary), (iv) moving out of the grain boundaries(GB) by diffusion controlled grain boundary migration (recrystallization) as shown in Figure 1.7. The coalescence can be "complete" when all the above mentioned processes have taken place and "incomplete" when recrystallization has not taken place ***[Barna, 1983].*** In the last case polycrystalline islands are developing in which both the size and orientation of the coalescing crystals are preserved.

During the complete coalescence process crystals with lower energy per atom consume their neighbor islands as the system attempts to minimize the overall surface and interface energy. This process results in single-crystal islands of increased size. Since nucleation on amorphous substrates leads to randomly oriented crystals ***[Pócza et al, 1969], [Thompson and Carel 1995]*** this restructuring/grain coarsening during complete coalescence is the first and most active phenomenon leading to selection of preferred crystal orientation due to lowering of the free energy per atom. This orientation selection takes place stepwise through a series of complete coalescence processes. The developing "restructuring" growth texture related to the minimization of substrate-crystal interface/surface energy is the <111> in case of fcc metals, the <110> in case of bcc metals and the <0002> in case of hcp metals ***[Vitos et al, 1998].*** Experiments carried out in the transmission electron microscope made possible to investigate these processes in details ***[Pashley et al, 1964], [Pócza et al, 1969], [Paschley and Stowell, 1966].***

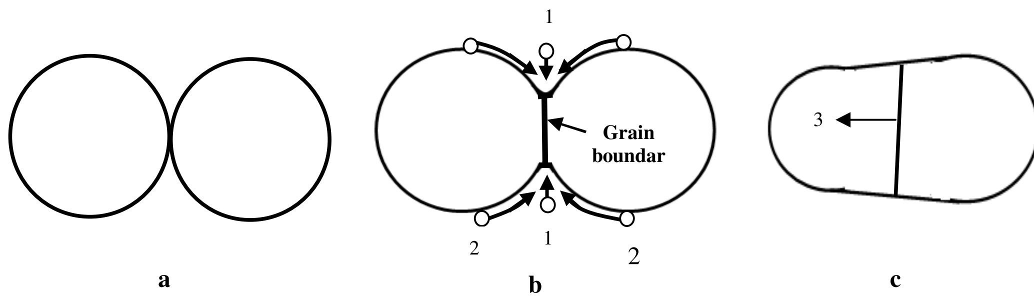

Figure 1.7. Steps of sintering phenomena: (a) neck formation, (b) filling the necks by surface self-diffusion, (c) moving out of the grain boundaries (GB) by diffusion controlled grain boundary migration.

The complete coalescence can be very fast, so called "liquid like" (Figure 1.3) proceeding either by rapid surface diffusion and GB migration or by melting upon contact followed by crystallization ***[Pócza et al, 1969].*** The fast, liquid-like coalescence results in the formation of 3D single crystals creating new open substrate surface area for secondary nucleation marked by arrows in Figure 1.3. The other type of the complete coalescence is a slower one and takes place in solid phase according to the well known sintering process of small grains ***[Pashley et al, 1964].*** This processes of coalescence can be followed in Figure 1.8 in case of epitaxial Au film

growing on air cleaved hexagonal MoS_2 <0002> platelet ***[Stowell, 1969].*** The contrast difference is related to the different orientation of the crystals. The coalescence starts by the formation of a neck between the coalescing neighbour crystals and proceeds by filling up of the neck by surface diffusion. At favourable geometry the coalescence can be completed by GB motion before a next coalescence sets in. The reorientation proceeding during the GB motion can be clearly seen by following the contrast changes. This complete coalescence results in the development of more 2D single crystals.

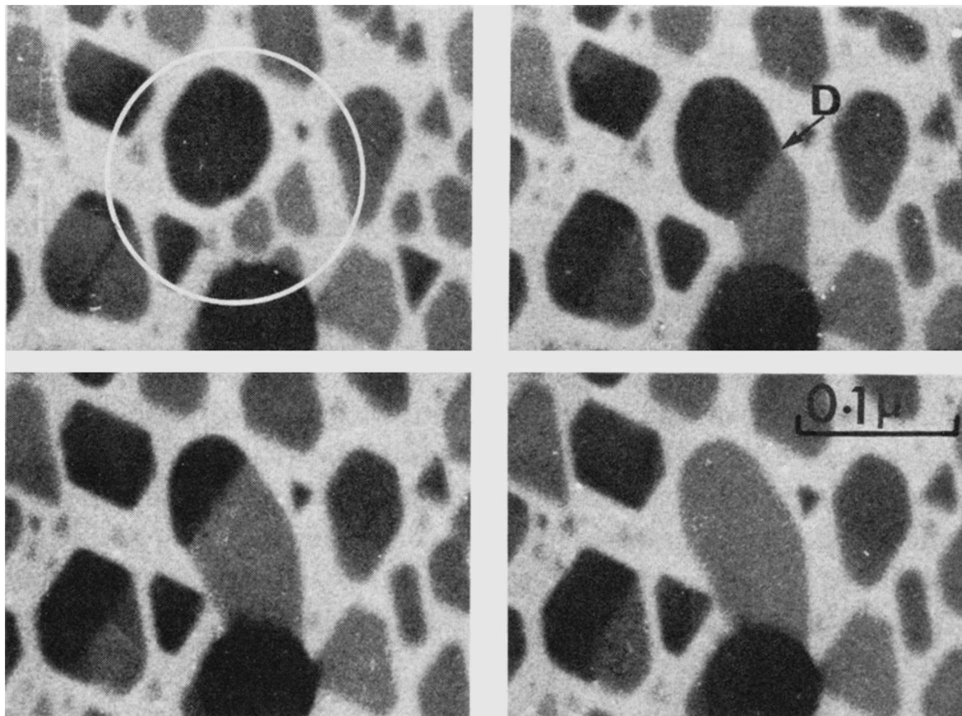

Figure 1.8. A series of TEM images from a movie showing coalescence of Au islands on air cleaved hexagonal MoS_2 (0002) crystal plate during in situ deposition at 670 K. The contrast difference is related to different orientation of the contacting crystals. Processes of solid phase coalescence and reorientation of one partner crystal can be clearly seen ***[Stowell, 1969].***

1.5. References

Barna Á., Barna P. B. and Pócza J. F., Design of a new vacuum deposition specimen holder for an electron microscope operatind at 10^{-8} Torr, Vacuum, 17 (1967)219-221.

Barna P. B., Crystal growth and recrystallization during structure evolution of thin films in Diagnostics and Application of thin films (Ed. L.Eckertova, I.Ruzicka) Institute of Physics Publishing, Bristol, (1992) pp. 295-309.

Barna P. B. and Adamik M., formation and characterization of the structure of surface coating, in "Protective coating and thin films synthesis, Characterization and Applications", ed. Y. Pauleau and P. B. Barna, NATO Science Partnership Sub-Series: 3: High Technology, Volume 21 (1996) page 284.

Barna P. B. and Adamik M., Fundamental structure forming phenomena of polycrystalline thin films and the structure zone models, Thin Solid Films, 317 (1998) 27-33.

Barna P. B., Impurity effects in the structural development of thin films, in de Segovia J. L., Proceedings of the 9th International Vacuum Congress and 5th International congress on solid surfaces, Madrid, Espanole el Vacio, Madrid, (1983) 382-396.

Detavernier C., Özcan A. S., Jordan-Sweet J., Stach E. A., Tersoff J., Ross F. M. and Lavoie C., An off-normal fiber-like texture in thin films on single-crystal substrates, Nature 426 (2003)641- 645.

Frost H. J., Microstructure Evolution in thin films, Material Characterization, 32(1994)257-273.

Greene J. E., Thin Film Nucleation, Growth, and Microstructural Evolution: An Atomic Scale View, in Martin P M, Handbook of deposition technologies for Films and coatings science, Application and Technology, Elsevier, (2010) 554-620.

Guozhong G., Nanostructures and Nonmaterial: Synthesis, Properties and Applications, Imperial College Pr, (2004) page 175.

Oura K., Lifshits V. G., Saranin A. A., Zotov A. V., and Katayama M., Surface Science: An introduction, Springer Berlin (2003) ISBN 3-540-00545-5.

Paschley D W and Stowell M, Nucleation and growth of thin films as observed in the electron microscope, Journal of Vacuum Science and Technology 10(1966) 156-166.

Pashley D. W., Epitaxial growth, ed J W Mathews (new York: Acad. Press1975) Part B p1.

Pashley D. W., Stowell M., Jasobs M. and Law T., The growth and structure of gold and silver deposits formed by evaporation inside electron microscope, Philosophical Magazine10 (1964) 127-157.

Pimpinelli A. and Villain J., Physics of Crystal Growth, Cambridge: Cambridge University Press (1998) ISBN 0-521-55198-6.

Pócza J. F., Barna Á. and Barna P. B., Formation processes of vacuum-deposited indium films and thermodynamical properties of submiucroscopicparticlesonserved by in situ electron microscopy, Journal of Vacuum Science and Technology, 6(1969) 472-475.

Pócza J. F., Forming processes of directly observed vacuum-deposited thin films, in Hahn E, Proc Second Colloquium on Thin Films, Budapest, Akadémiai Kiadó, (1967) 93-108.

Stowell M. J., Surface processes in thin-film growth, in Drauglis E, Gretz R D and Jaffee R I, Molecular processes on solid surfaces, New York, McGraw-Hill Book Co., (1969) 461-477.

Tadmor R., Line energy and the relation between advancing, receding and Young contact angles, Langmuir 20 (18) (2004): 7659. doi:10.1021/la049410h, PMID 15323516.

Thompson C. V. and Carel R., Texture development in polycrystalline thin films, Materials Science and Engineering B32 (1995) 211-219.

Thompson C. V., Grain growth in thin films, Annual review material, Science, 20(1990) 245-268.

Venables J A, introduction to Surface and thin film pprocesses, Cambridge, Cambridge University Press (2000) ISBN 0-521-62460-6.

Venables J. A., Spiller G. D. T. and Hanbucken M., Nucleation and growth of thin films, Reports on Progress in Physics, 47(1984) 399-459.

Vitos L., Ruban A. V., Skriver H. L. and Kollár J., The surface energy of metals, Surfuce Scince 411(1998)186–202.

Chapter 2

Structure Zone Model (SZM)

2.1. Introduction

Polycrystalline thin films are applied in advanced technologies and in a wide range of devices and components including magnetic storing, optics, sensors, hard surface coating, etc ***[Barna, 1992]***. The coatings are often considerably different from bulk materials of the same composition and have highly anisotropic properties due to their anisotropic microstructures, since the coating flux approaches the substrates from a restricted range of directions and ad-atom mobility is relatively low at low deposition temperatures. However, as the deposition temperature increases and ad-atom mobility is enhanced, denser equiaxed coatings are produced ***[Mellor, 2006]***.

The first efforts to characterise the structures of PVD coatings by Movchan and Demchishin ***[Movchan and Demchishin, 1969]*** recognized that there are three different structure zones as a function of homologous deposition temperature T/T_m (where T is the substrate surface temperature and T_m bulk melting temperature of the film material). The low-temperature ($T/T_m < 0.3$) zone 1 structure corresponds to low ad-atom mobility and consists of tapered columns with domed tops. In zone 2 ($0.3 < T/Tm < 0.5$), surface diffusion becomes important and the structure is a straight columnar region with smooth surface topography. At higher temperatures ($T/T_m > 0.5$), bulk diffusion is the dominant process and the zone 3 structure produced is characterized by equiaxed grain (Figure 2.1a). Later work by Thornton ***[Thornton, 1974]*** demonstrated that the presence of a sputtering gas could modify the model and a further region identified as zone T was inserted between zones 1 and 2 (Figure 2.1b) we will explain this in more detail later. According to that the structure is synthesized by the production technology and the pathway of atomic processes and structure evolution is controlled directly by the technology parameters.

In the present chapter a possible synthesized view of thin film structure evolution will be discussed from nucleation to the thicknesses of continuous films which include also the structure related to the oriented growth regime. It is attempted to consider the structure evolution in its entirety and as a history (pathway) of fundamental phenomena of structure formation (nucleation, crystal growth and grain growth) which are related to atomic processes (adsorption-desorption, surface and bulk diffusion, atomic interactions on and with the growing surface). The pathway is strongly related to the self-organizing nature of the phenomena. That means that the actual course of atomic processes and, consequently that of the fundamental phenomena are varying steadily during the deposition because they are controlled directly by the instantaneous structure (surface and bulk structure as structural pre-conditions (SPC)) developed during the precedent growth stages. It has to be underlined that the fundamental phenomena and the synthesized view hold both for elemental and multi-component films but the atomic processes and the fundamental phenomena are more complex in the second case.

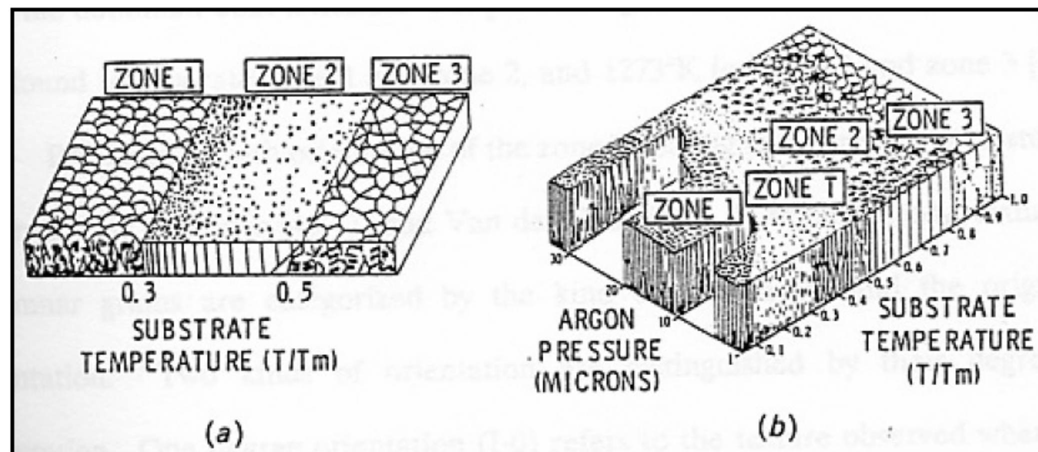

Figure 2.1. Structural zone models for coating growth. (a) ***[Movchan and Demchishin, 1969]****, (b)* ***[Thornton, 1974]****.*

2.2. The structure zone models

2.2.1. Derived temperature structure zone model (TSZM) of elemental, high purity films

The temperature structure zone model (TSZM) derived for elemental high purity metallic films growing on amorphous substrate are shown in Figure 2.2. This

figure illustrates the cross sectional structure at increasing film thicknesses in the various temperature intervals. The active atomic processes and related fundamental phenomena of structure formation in the characteristic temperature intervals are included. Out of the generally very complex atomic processes and interactions characterizing the structure evolution of functional thin films only the surface and bulk diffusion are active and control the operation of the fundamental phenomena in case of high purity elemental films.

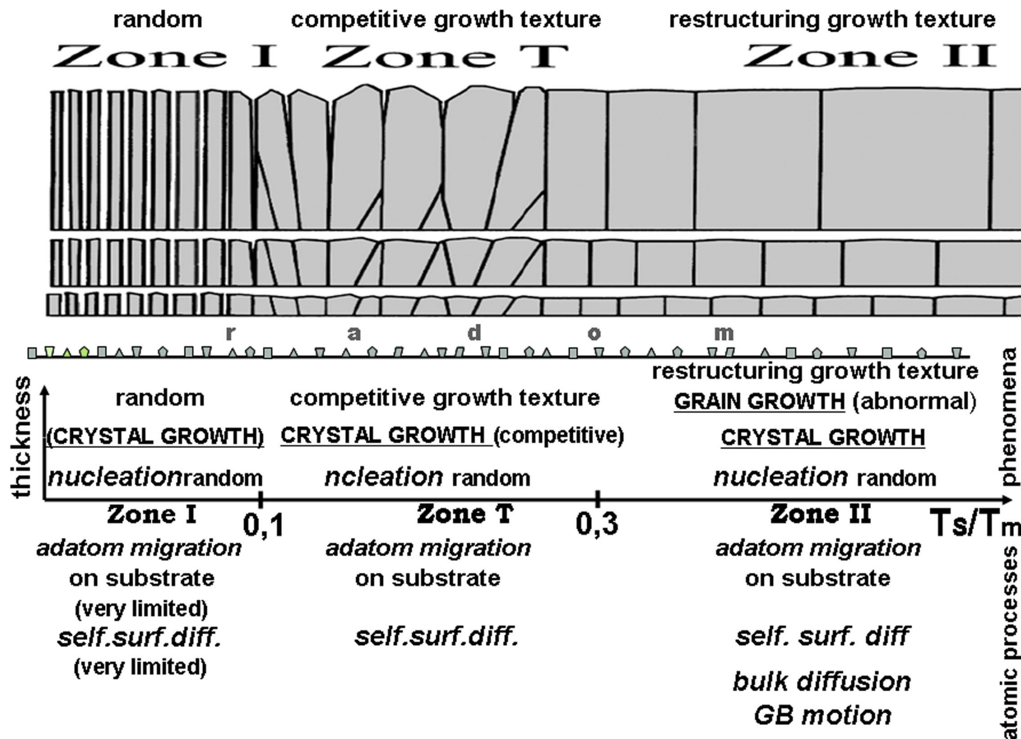

Figure 2.2. Derived temperature structure zone model (TSZM) of elemental polycrystalline films grown on amorphous substrate. Atomic processes operative in the characteristic temperature ranges and the related fundamental phenomena of structure formation are included ***[Barna and Adamik, 1998]***.

One can identify immediately that in contrast to the CTSZMs as shown in Figure 2.3 the derived TSZM consist only of three zones ***[Barna and Adamik, 1998], [Petrov et al, 2003], [Radnóczi and Barna, 2006***]: zone I at $T_S < 0.1T_m$), zone T at $0,1T_m < T_S < 0.3$ Tm and zone II at $T_S > 0.3\ T_m$. Characteristics and the pathway of the evolution of these structures are summarized in the following.

Zone I

The number of impinging ad-atoms condensed on a foreign material surface (referred as substrate) and their number are increasing by the time. If the density of condense ad-atom is high enough the primary nucleation is formed when two ad-atoms impinging each other.

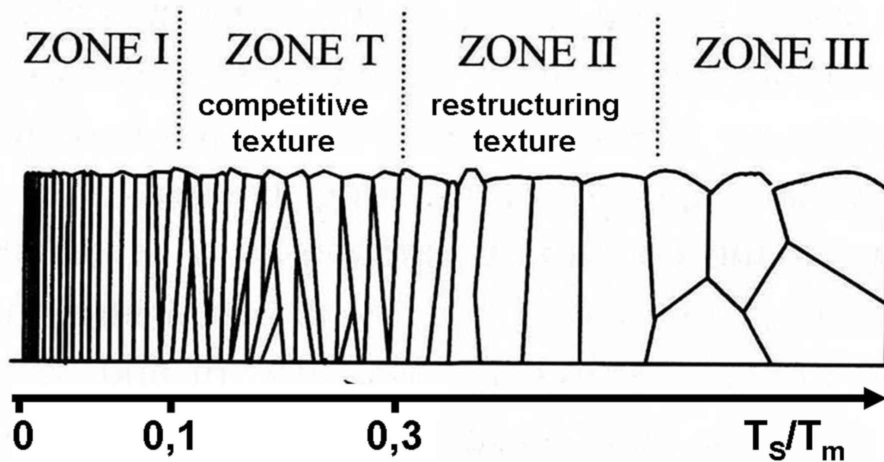

Figure 2.3. Main characteristics of the structure zones of the conventional temperature structure zone models (CTSZM) published in the literature (From ***[Barna and Adamik, 1998)]****.*

The nuclei are growing according to the ballistic deposition models ***[Dirks and Leamy, 1977]***. This mean the impinging ad-atom hit the nuclei and stick on the same position. This is due to the fact that the self surface diffusion is very limited in this Zone. By this way the underdense structure with fiber morphology is formed and composed of smaller domains with crystal structure. The structure is homogenous along the film thickness and preserves the random orientation of the nuclei. The in-plane grain size at the substrate is determined by the saturation nucleation density which is very high. Only local rearrangement of joining ad-atoms and some relaxation of the grown structure can be considered. Atomic shadowing plays important role in the development of fiber morphology and surface roughness as shown in Figure 2.*4*.

Zone T

The structure is changing along the film thickness. At the substrate a small grained structure exists with random orientation of crystals. That is followed by a V-shaped columnar structure with increasing column size. The random orientation is gradually deceasing while a preferred orientation due to the V-shaped crystals intensifies. That is the competitive growth regime. The third thickness domain shows columnar morphology with the preferred orientation developed in the precedent thickness range. This third thickness domain is the oriented growth regime.

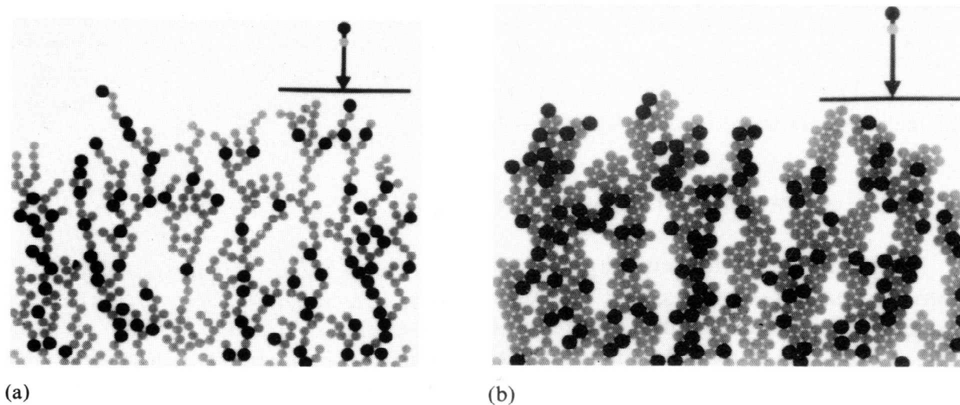

Figure 2.4. Ballistic model of structure formation (a) without relaxation (b) with relaxation models ***[Dirks and Leamy 1977].***

The evolution of this structure is described by the following pathway. In this temperature range ($0.1T_m < T_S < 0.3\ T_m$) the ad-atom mobility is significant while the bulk diffusion and grain growth are negligible. Thus the main phenomenon which governs the structure evolution in the post-nucleation ranges is the crystal growth. The crystals are growing by two ways either the impinging ad-atom hit the substrate surface and migrate to stick on the nuclei or the impinging ad-atom hit directly the nuclei and stick. By any way the nuclei grown and form the discrete crystals on substrate. The first growing crystals are randomly oriented on the amorphous substrate. The crystal increased in size through growth on the lateral until touch each other. The coalescence of crystals is incomplete because of the lack of bulk diffusion. Consequently the continuous film developing at first on the substrate is composed of randomly oriented crystals.

The film surface has low roughness due to the small grain size. In the next thickness domain the structure evolution is governed by the orientation controlled growth competition of the randomly oriented neighbour crystals resulting in orientation selection. Crystal with faster growing faces (low ad-atom mobility, fcc-001 crystal face) accumulates more ad-atoms by surface diffusion from the neighbour high ad-atom mobility faces (fcc -111 face) and will grow over them ***[Vand der Drift, 1967], [Knuyt et al, 1995], [Barna and Adamik, 1998], [Petrov et al, 2003].*** Both the size and shape of columns and the orientation of crystals are changing with thickness. The competitive growth texture develops gradually with the fastest growing crystals developing the V-shaped columns. That is the competitive growth regime. The surface is composed of crystal faces terminating the columns and the roughness is increasing with thickness due to the increasing size of columns with changing orientations. When the competitive growth is completed, the growth surface is composed by crystal faces of the same Miller indices terminating all columns with the same orientation. From this stage the structure evolution is continued by the growth of oriented columns (oriented growth regime). The size (diameter) of columns is not changing with thickness and the distribution of columns diameter is monomodal in this thickness domain.

Figure 2.5 shows the computer simulation of the process of competitive growth.

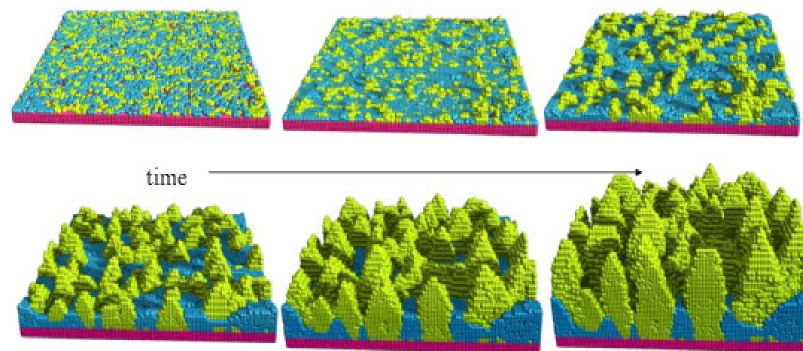

The blue crystals indicated the 111 crystals

The yellow crystals indicated 100 crystals

Figure 2.5. Competitive growth of aluminum crystals on amorphous substrate at Ts=100K ***[Bauman et al, 2001].***

Zone II

At $T_S > 0.3T_m$ the structure of the continuous films is columnar and homogenous along the thickness at every film thicknesses as shown in Figure 2.6 Crystals are oriented according to the lowest substrate crystal interface energy; GBs proceed from the substrate to the top and are perpendicular to the substrate plane. The lateral size of columns is increasing with the thickness of the as-prepared film and can be larger than the film thickness. The film has a very sharp texture perpendicular to the substrate plane. The surface is smooth and composed by crystal faces with the same Miller indices parallel to the substrate plane.

The evolution of this structure is described by the following pathway. In this temperature range the bulk diffusion becomes significant and the grain growth and reorientation of crystals governed by the minimisation of the interface and surface energy dominate the structure evolution. Nuclei and the first growing crystals are randomly oriented. The orientation selection of crystals due to the minimisation of interface and surface energy takes place during the consecutive complete coalescence processes and can be completed till the end of the coalescence stage. The grain size distribution is bimodal in the coalescence stage mainly because of the presence of small crystals developed by secondary nucleation as a consequence of the liquid-like coalescence. Diffraction patterns indicate the coexistence of random and oriented crystals at these thicknesses. At higher deposition temperatures liquid phase could be also presented in the first growth stages.

The continuous film develops by the last, incomplete coalescence of the already oriented crystals. By this way the thickness growth is practically an oriented growth regime which proceeds by the continuous, uninterrupted growth of the neighbour crystals with nearly the same perpendicular orientation. The texture can be improved in the continuous film by additional abnormal grain growth while the grain size is increasing by grain growth driven by the minimisation of grain GB energy increasing during the film growth.

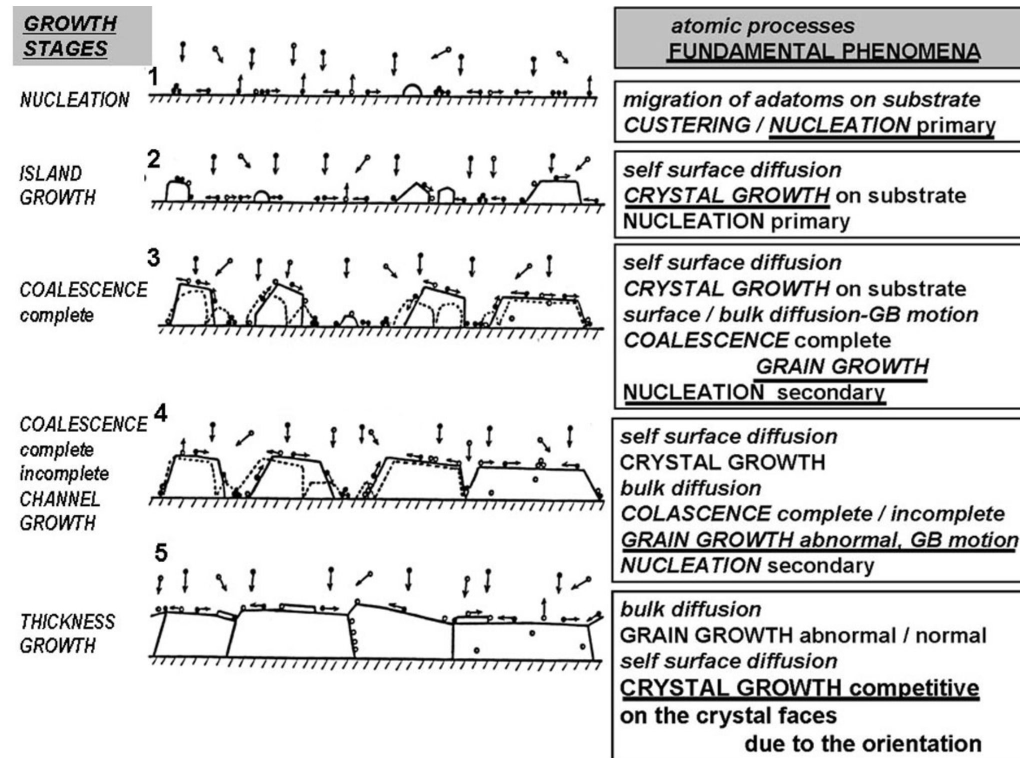

Figure 2.6. Schematic diagram illustrating the growth stages, atomic processes and fundamental phenomena controlling the microstructural evolution of polycrystalline thin films in Zone II ***[Barna 1992].***

2.2.2. Structure Zone Models of multicomponent and multiphase films

In this section the temperature structure zone models of $A_{1-X}B_X$ material systems will be discussed at various values of X in case when the A and B material constituents are not reactive and have no mutual solubility. At the co-deposition of various elements both the atomic processes and the pathway of fundamental phenomena are very complex and the pathway of structure evolution is sensitively controlled also by the competitive growth of phases.

In this respect the component forming tissue phase (grain refiner or inhibitor additive) are the most active. Namely the excess species of a tissue phase are segregated by the atomic processes of crystal growth and develop a bidimensional layer on the growth surface (surface covering layer, SCL) and on GBs. Figure 2.7 shows the temperature structure zone models (TSZM) for an $A_{1-X}B_X$ film at $X<0.15$

where *B* is the component forming tissue phase. The $TSZM_s$ were derived at various values of X by constructing the pathway of fundamental phenomena for the given concentration of the *B* component. It is to mention that a component forming tissue phase can be purposeful dopant as well as unintentional atmospheric contaminant such as water vapour, oxygen, nitrogen, and hydrocarbons. The operation of *B* grain refiner component is explained in the various temperature regimes supposing that the sticking probabilities of A and *B* species do not depend on the deposition temperature.

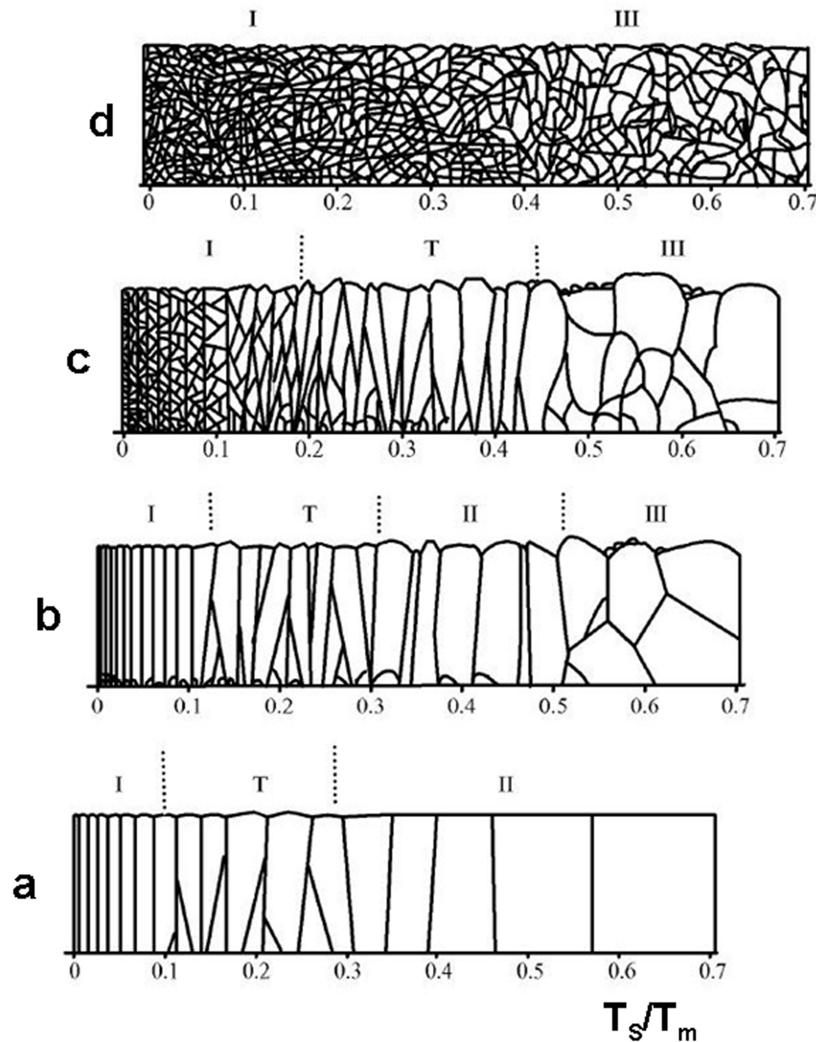

Figure 2.7. Derived temperature structure zone models (TSZM) of $A_{1-X}B_X$ film at increasing X values when the B component forms tissue phase. a) X = 0; b) ~0.02 < X < ~0.05; c) ~0.05 < X ~0.08; d) ~0.08 < X ~0.15. Zone III structure of the CTSZM shows up at X > ~0.02. ***[Barna and Adamik, 1995].***

Low level of B concentration (0.02< X<0.05)

In Figure 2.7.b, the structure zone model at low level of B concentration is shown.

Zone I

At very low temperature no segregation of the impurity species B can take place and they will be incorporated into the growing lattice of fibers. These phenomena described by the ballistic models ***[Dirks and Leamy, 1977]*** and fiber like structure develops. The structure related to zone I are frozen in structures both in high purity and in contamination films ***[Barna and Adamik, 1995]*****.**

Zone T

The segregation of impurity species B by the crystal growth increases by increasing temperature and the impurity phase is expected to be segregated mainly at the grain boundaries. Namely, due to the initially small grain size, high density of grain boundaries develops and offers large GB surface area enough to absorb all segregated B species. That means that the SCL of B will not grow over the growth surface of the neighbour crystals and do not affect their orientation related growth competition. Structure corresponding to zone T develops with GBs covered and possibly stabilized by the B tissue phase. This structure is stable against restructuring during heat treatments.

Zone II

The segregation of impurity species B are present only in the adsorption layer as ad-atoms on the surface of individual crystals growing to larger sizes in the island growth stage. The coalescence of crystals can be active in developing the restructuring texture due to the minimization of interface energy. The excess B species can be segregated also by the coalescence increasing their concentration on the surface of crystals. The complete coalescence will be terminated when the concentration of the excess B species gets the value to nucleate a solid tissue phase on the side faces of the crystals. GBs covered by tissue phase develop and will incorporate the excess B species segregated on the growth surface of neighbor crystals. If the developing GB surface area is large enough to incorporate all segregated B species, a structure corresponding to zone II develops, however with column’s size smaller than that in the pure film corresponding to the same deposition

temperature. By increasing the temperature the size of columns increases while the GB surface area decreases. If the GB surface area is not large enough to absorb all segregated excess B species, the SCL will grow over the surface of the neighbor crystals; terminate their growth and the film growth proceeds by repeated nucleation. This process can result in the fragmentation of columns and in the development of large, more equiaxial grains.

Zone III

The segregation of impurities species B by the GB movement becomes effective with increasing temperature and by this way a contamination layer can develop covering completely the surface of growing crystals. This results in the development of three dimensional large grains which are separated by contamination stabilised GBs. The grain size distribution is impurity stabilised bimodal. Texture due to the surface and interface energy minimisation can be presented because in the coalescence stage of film formation the restructuration could be effective.

Medium level of B concentration (0.05< X<0.08)

As shown in Figure 2.7c, the structure zone model at medium impurity concentration. The pathways of atomic processes and phenomena are the same as discussed before. But SCL can be formed already at smaller island size and the complete coalescence could be also limited at lower grain sizes. Consequently the zone II structure will be missing in the TSZM. The temperature range in which zone T structure develops is broader and the size of quiaxed grains at higher temperatures is decreased. In the very low temperature range amorphous structure can develop also in metallic films by this process.

High level of B concentration (0.08<X<~0.15)

As shown in Figure 2.7 d the individual grains are encapsulated by the SCL in the whole temperature range and only zone I and zone III structures develop. Zone I is amorphous of high probability. The grain size of metallic crystals can approach the nm sizes.

2.2.3. Compositional Structure Zone Model

The compositional structure zone model is derived in the temperature regime $T_S>0.3T_{mA}$ for an $A_{1-X}B_X$ film in the composition range of $0 < X < 1$ when the *B* is a

grain refiner component (forming tissue phase) and T_{mA} is the bulk melting temperature of the A metallic component (Figure 2.8). At low concentration of *B,* crystals of A nucleate and grow at first and segregate the *B* species. The *B* tissue phase starts to be formed by delayed nucleation on the surface of A crystals. The processes are the same as discussed in the previous section and structures shown

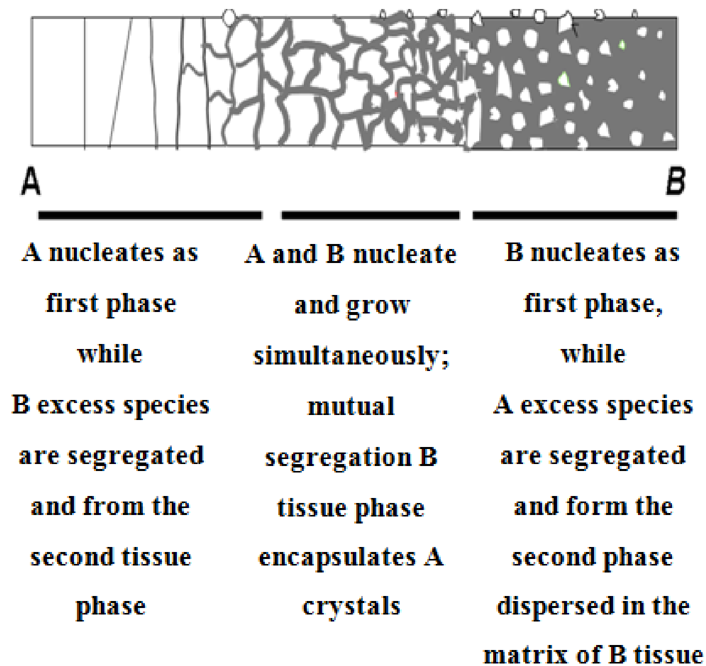

Figure 2.8. Compositional structure zone model of $A_{1\text{-}X}B_X$ film in the temperature range of zone II when the B component forms tissue phase. Dependence of the nucleation sequence of phases on the composition are given.

in Figure 2.7 are developing. There is a composition range, when both the A and *B* phases nucleate and grow simultaneously from the very beginning of condensation. Their competitive growth proceeds by mutual segregation and repeated nucleation. A globular structure develops in which the 3D crystals of the *A* phase are encapsulated by the *B* tissue phase. At higher values of X the *B* phase will nucleate at first and grow while the A species are segregated. 3D crystals of A phase will nucleate and grow repeatedly and will be embedded by the majority *B* tissue phase. A bulk structure of the tissue *B* phase is growing with 3D A crystals dispersed in the matrix of the tissue phase ***[Barna et al, 1998], [Radnóczi and Barna, 2006].*** Same compositional structure zone model (CoSZM) has been developed by ***[Patscheider et***

al, 2001] for Si doped TiN films and explained the correlation between composition, structure and hardness.

2.2.4. 3-D inclusion developed in co-deposited films

Temperature structure zone models of an $A_{1-X}B_X$ film at various concentrations when both A and B components are growing in 3D grains. B can grow by Volmer-Weber (VW) on the surface of the crystal of A phase (Figure 2.9). Figure 2.9 a illustrates the development of growth morphologies in the island growth stages. In Figure 2.9 b this structure is illustrated in co-deposited Al and Ni film ***[Radnóczi and Barna, 2006].*** The TSZMs of the $A_{1-X}B_X$ material system are shown in Figure 2.10 at various compositions.

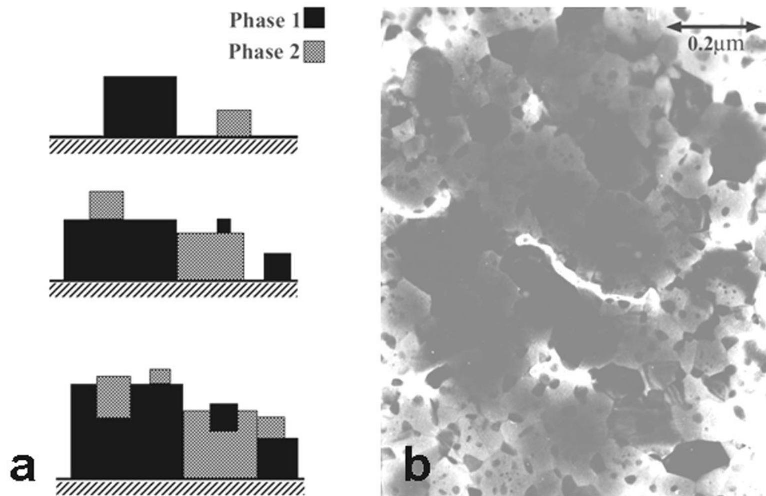

Figure 2.9 (a): schematic growth morphologies during deposition of an $A_{1-X}B_X$ thin film system when both components are growing 3D; (b): TEM image of a co-deposited Al and Ni (5 vol%) thin film ***[Radnóczi and Barna, 2006].***

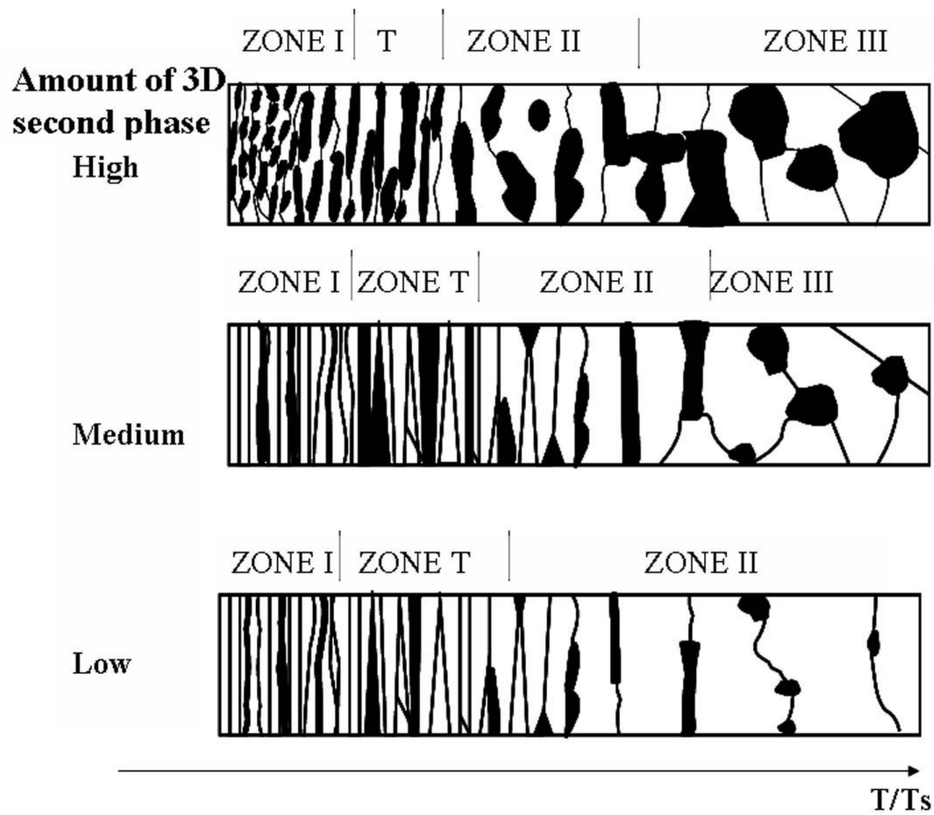

Figure 2.10. Schematic TSZM of $A_{1-X}B_X$ thin film system for different values of X when both components are growing in 3D ***[Radnóczi and Barna, 2006]***.

2.3. References

Barna P. B., Crystal growth and recrystallization during structure evolution of thin films in Diagnostics and Application of thin films (Ed. L.Eckertova, I.Ruzicka) Institute of Physics Publishing, Bristol, (1992) pp. 295-309.

Barna P. B. and Adamik M., Formation and characteristics of the structure of surface coating, in " protective coating and thin films: synthesis, characteristic, ed. Y. Pauleau and P.B.Barna, NATO ASI series, 3.High Technology, Kluwer Academic publisher, Netherlands, 21 (1998) 290.

Barna P. B. and Adamik M., Fundamental structure forming phenomena of polycrystalline thin films and the structure zone models, Thin Solid Films 317 (1998)27-33.

Barna P. B. and Adamik M., Growth mechanisms of polycrystalline thin films in, science and technology of thin films, ed. F. C. Matacotta and G. Ottaviani, world scientific publishing Co., Singapore, 1-28(1995).

Barna P. B., Barcza G., Tóth L., Vincze G., Bergauer A. and Bangert H., Structure evolution in codeposited Al-Sn thin films", Surfce Coating and Technology 57(1998) 7-11.

Bauman F. H., Chopp D. L., Diaz de la Rubia T., Gilmer G. H., Greene J., Huang H., Kodanbaka S., Sullivan P. O. and Petrov I., Multi-scale Modeling of Thin Film Deposition, Applications to Si Device Processing, MRS Bulletin, 26 (2001) 182.

Dirks A. G. and Leamy H. J., Columnar microstructure in vapor-deposited thin films, Thin Solid Films, 47 (1977)219-233.

Knuyt G., Quaeyhaegens C., Haen D. J. and Stals L. M., A quantitative model for the evolution from random orientation into a unique texture in PVD film growth, Thin Solid Films, 258 (1995)159-169.

Mellor B. G., Surface coatings for protection against wear, CRC Press, Woodhead Publishing Ltd, Cambridge, UK, (2006), Page 169.

Movchan B. A. and Demchishin A. V., Investigations of the structure and properties of thick nickel, titanium, tungsten, aluminum oxide and zirconium dioxide vacuum condensates, Fiz. Metall. Metalloved., 28(1969) 83–86.

Patscheider J., Zehndera T. and Diserens M., Structure–performance relations in nanocomposite coatings, Surfce Coating and Technolg 146–147 (2001) 201–208.

Petrov I., Barna P. B., Hultman L. and Greene J. E., Structural evolution during film growth, Journal of Vacuum Science and Technolology, A 21 (2003) S117-S128.

Radnóczi G. and Barna P. B., Formation and characterisation of the structure of thin films and coatings, in Y. Pauleau, Materials surface processing by directed energy techniques, Elsevier-EMRS (2006) Ch. 13, 443-474.

Thornton J. A., Influence of apparatus geometry and deposition conditions on the structure and topography of thick sputtered coatings, Journal of Vacuum Science and Technology, 11(1974)666–670.

Van der Drift A., Evolutionary selection, a principle governing growth orientation of vapour deposited layers, Philips Res Repts, 22 (1967) 267-288.

Chapter 3

Experimental methods

3.1. Introduction

In this chapter, we provide an overview of most generally applied thin film preparation techniques. I will discuss in more details the sputtering process and unbalanced magnetron sputtering (UMS) technique which we used for the preparation of TiN films. In addition, we will review the most important techniques which are lead to determine the structure of these films such as cross-section (X-TEM), plan view transmission electron microscopy and selected area diffraction (SAED), precession electron diffraction PED-ASTAR technique, Energy dispersive X-ray microanalysis (EDX), X-ray diffraction (XRD)**,** Auger (AES) and X-ray photoemission spectroscopy (XPS), Atomic force microscopy (AFM) and Ultra-Micro-Indentation system (UMIS).

3.2. Thin film deposition methods

Thin film on a substrate is generally prepared by the atom-by-atom deposition (there are method when the whole layer is deposited by an explosion). The main difference between the various preparation techniques is the mode of the production of the free species to be deposited. Physical vapor deposition (PVD) and chemical vapor deposition (CVD) methods are mainly used. In the present thesis we will focus on the magnetron sputtering technique ***[Fahrner, 2005]***.

The main aspects of the PVD methods are compiled in Figure 3.1. Preparation of the films takes place in a vacuum chamber characterized by the residual pressure (in the range of 10^{-3} – 10^{-9} Pa) and by the composition and partial pressure of the residual gases/vapors (in the high vacuum (HV) range water vapor, oxygen, nitrogen and hydrocarbons, in the ultrahigh vacuum range (UHV) mainly CO, H and He). The vaporized species of the film material components are produced mainly by evaporation or sputter source(s) ***[Martin, 2010].*** The characteristics of the emitted species are the flux J, energy E, sizes (atoms, clusters) and ionization state (neutrals or ions) which depend on the material(s) and on the type and working parameters of the

source. The kinetic energy, E, of species is 100-200 MeV at thermal evaporation and 5 to 10 eV of sputtered species at floating substrate potential. This last one is in the order of, or larger than the bonding energy in solids. The transport of free species emitted by the sources to the substrate makes possible to manipulate their electrical charge and kinetic energy.

However species of the desorbed or residual atmospheric gases/vapours and the products of the possible interactions between the source and the material have to be also considered. An increase of the pressure in the chamber due to operation of the sources indicates directly that gases or vapors are desorbed. This phenomenon has to

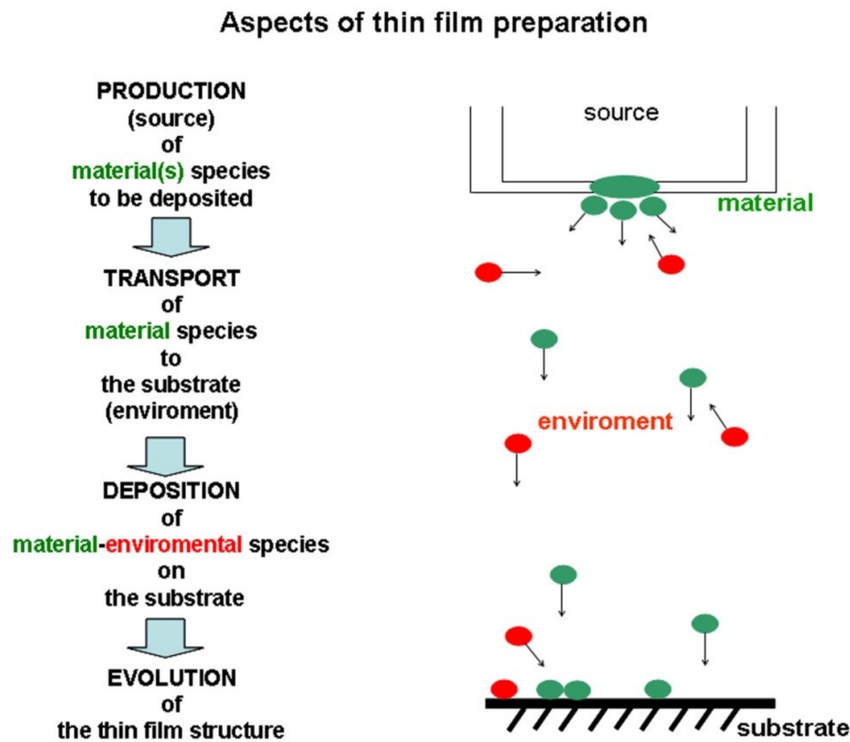

Figure 3.1. Main aspects of the physical vapour deposition.

be considered carefully, because one part of these species impinge directly on the substrate and participate in the structure evolution as unintentional impurities (contaminants). By this way the concentration of contaminant species in the condensing vapor beam might be more significant than could be estimated from the

total pressure measured in some part of the system ***[Barna, 1983], [Barna and Adamik, 1995].*** Most of these contaminants operate as inhibitors, ***[Petrov et al, 2003], [Greene, 2010]***and might have a remarkable effect both on the structure and properties even at low concentration, sometimes below the detection limits of modern analytical techniques. The quantity of impurity species in the condensing vapor beam is characterized by $K_i = J_i/J_d$, the arrival rate ratio of unintentionally depositing, impurity species (J_i) and intentionally deposited material species (J_d). In conventional technologies (experiments) $K_i \geq 10^{-3}$.

In general, PVD consist of sub-methods such as thermal evaporation ***[Qasrawi et al, 2004],*** Molecular Beam Epitaxy (MBE) ***[Gautier et al, 1998]*** electron beam evaporation, Pulsed laser deposition (PLD) and sputter deposition ***[He et al, 2002].***We will briefly describe each method in the following items.

3.2.1. Thermal evaporation technique

Thermal evaporation technique is the most widely used technique for preparation of thin films ***[Holland, 1956].*** In this technique, the material can be evaporated either by the heat generated by the resistance of a metal container. The material vapor finally condenses in form of thin film on the cold substrate surface and on the vacuum chamber walls. Usually low pressures are used, about 10^{-6} or 10^{-5}Torr, to avoid reaction between the vapor and atmosphere.

3.2.2. Molecular Beam Epitaxy (MBE) technique

MBE is an Ultra High Vacuum based technique for producing high quality epitaxial structures with monolayer control. The sources of species are generally specially designed evaporation sources to decrease the interaction of the material and the source as well as the desorption of gases/vapours by the source during functioning. MBE deposition systems are UHV systems completed by various analytical methods (mass spectrometer for analysising the vapour beam impinging to the substrate, reflection high and/or low energy electron diffraction, AES and SXPS analysis system, etc). Despite the conceptual simplicity, a great technological effort is required to produce systems that yield the desired quality in terms of material purity, uniformity and interface control ***[Biasiol and Sorba, 2001].***

3.2.3. Electron beam evaporation technique

In this method the material is bombarded and heated by an electron beam. The electrons are accelerated by 2-6 KV to get high energy. A magnetic field is also applied to focus and bends the electron trajectory.

3.2.4. Pulsed Laser Deposition (PLD)

In the PLD methods a high power pulsed laser beam is focused inside a vacuum chamber to hit the surface of the solid target. The strong absorption of the electromagnetic radiation by the solid surface leads to rapid evaporation of the target materials. The evaporated material consists of highly excited and ionized species. This process can occur in ultra high vacuum or in the presence of a background gas, such as oxygen which is commonly used when depositing oxides to fully oxygenate the deposited films**.**

3.2. 5. Sputtering system

Thin films of high melting point materials, like the titanium oxynitride, which we investigated, can be successfully prepared by dc reactive magnetron sputtering using a titanium metallic target and argon, nitrogen, or other gases. This process offers the advantage of a homogeneous large area coating in the final production. For the production of suitable coatings favorable deposition parameters have to be identified.

3.2.5.1. Principle of sputtering sources operation

In sputtering process, the material is released from the source at a lower temperature than the evaporation. As we shown in Figure 3.2 the substrate (which is the anode) and the source material (target which is the cathode) are placed into a vacuum chamber and an inert gas (usually argon Ar) is introduced at low pressure around 1to100 mTorr ***[Thornton and Greene, 1994], [Aufderheide, 2006].*** A glow discharge is maintained by a direct current (DC) voltage in the KV range between the anode and the cathode. Positive ions are accelerated towards the target surface and create target atom which are condensating on the substrate to form thin films, on the other hand they produce secondary electrons. These electrons cause a further ionization of the gas.

3.2.5.2. Sputtering yield

The sputter yield (S) is defined as the ratio of the number of ejected atoms to the number of incoming energetic ions. The sputtering yield depends on the following factors:

- The kinetic energy of incoming ions,
- The binding energy of the target atoms ***[Lieberman and Lichtenberg, 2005],***
- The angle of incidence,
- The efficiency of momentum transfer between the incoming ions and the target atoms ***[Ohring, 2002].***

The kinetic energy fraction transferred from incident to target atom is:

$$\varepsilon = \frac{4m_i m_t}{(m_i + m_t)^2} \qquad 3.1$$

Where m_i and m_t is the mass of the incoming ion and mass of the target atom, respectively.

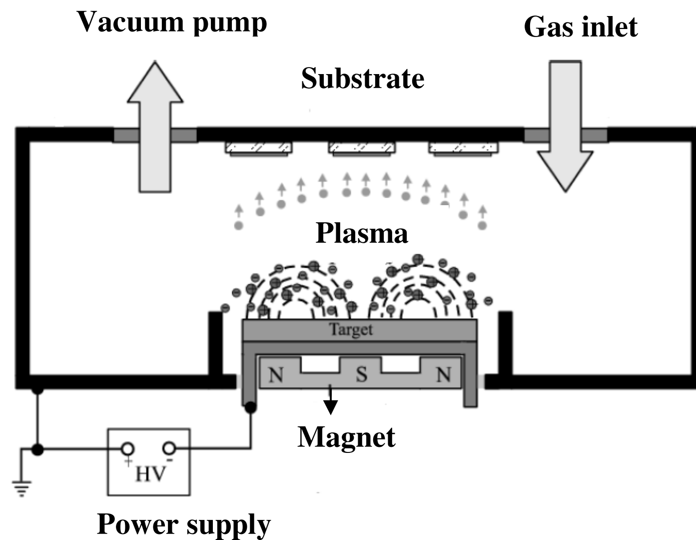

Figure 3.2. Sample schematic of a DC sputters system.

And the sputtering yield (S) can be written in the form ***[Sigmund, 1969]:***

$$S = \frac{3\alpha}{4\pi^2} \frac{m_i m_t}{(m_i + m_t)} \frac{E}{U_0} \qquad 3.2$$

Where U_0 is the surface binding energy of the material being sputtering, E is the bombardment energies and α is a monotonic increasing function of m_t/m_i.

Values of sputtering yield are depending on type of material. The sputtering yield takes the same behavior for the most material but with various values as shown in Figure 3.3 ***[Stuart and Wehemer, 1962]***. In addition, the sputtering yield of pure metal is greater than the sputtering yield of the compounds like oxide.

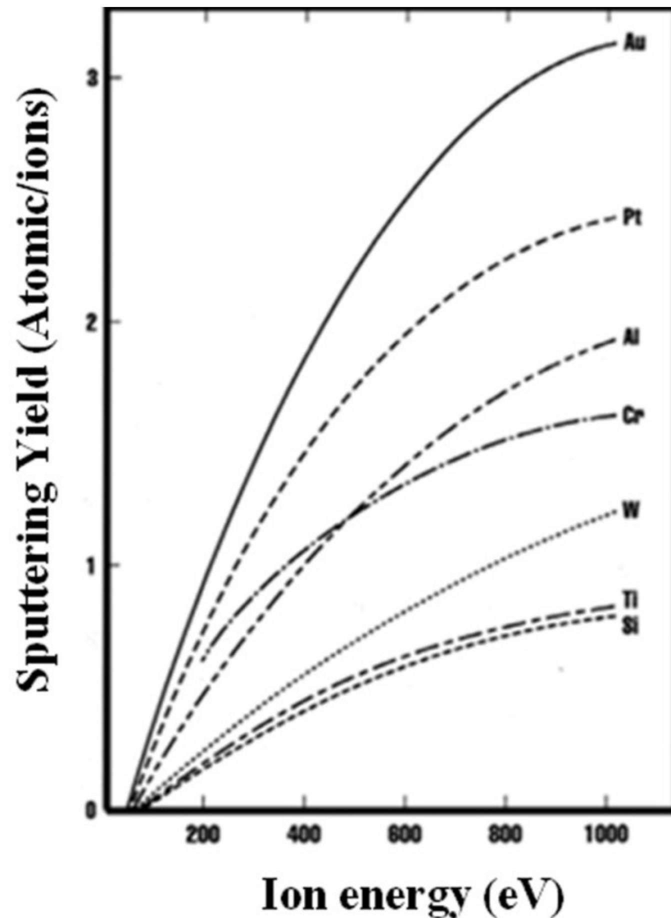

Figure 3.3. Variation of the sputtering yield for different materials at normal incidence ***[Stuart and Wehemer, 1962]***.

3.2.5.3. Processes at the target

The positive ions will be attracted by the negative target potential and may sputter away target atoms if the energy of the impacting ions is high enough. The efficiency of this process depends on the sputtering yield of the target material.

Besides ejection of target atoms, a number of other processes might occur as energetic ions hit the target such as secondary electron, photons and reflected ions as shown in Figure 3.4.

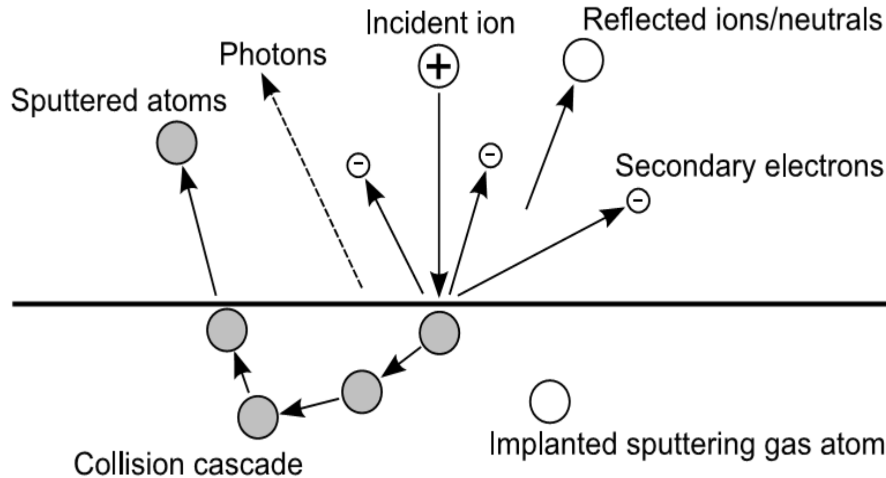

Figure 3.4. Events that occur on a surface being bombarded with energetic atomic-sized particles.

3.2.5.4. Magnetron sputtering

Magnetron Sputtering is the most commonly used process for the deposition of high quality metal and compound thin films for a variety of applications. The principle of this technique is to place permanent magnets in a suitable configuration behind the cathode (target) in order to increase the efficiency of the sputtering process. As shown in Figure 3.5 the electrons move in orbits close to the cathode. The electrons will then be acted on by the Lorentz force, given by

$$F = m\frac{d\nu}{dt} = q(E + \nu x B) \qquad 3.3$$

where m, q, and **v** are the electron mass, electron charge, and electron velocity, respectively. E and B are the electric and magnetic fields, respectively. Solving the equations of motion, the electrons are found to follow cycloidal trajectories along the target (if initially launched slightly of the target normal) to increase the probability of ionization of the sputtering gas.

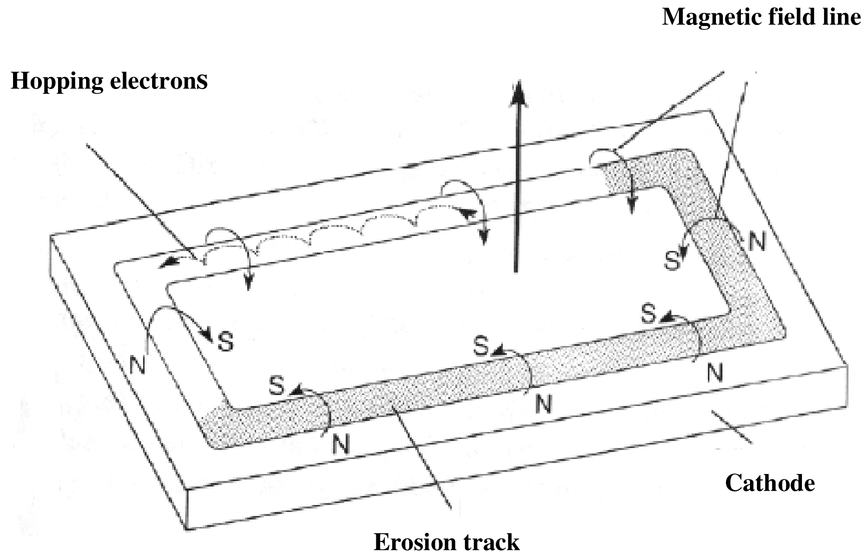

Figure 3.5. Schematic showing the effect of a planar magnetron.

3.2.5.4.1. Unbalanced magnetron sputtering

The unbalanced magnetron (UM) sputtering source takes use of a highly non-symmetric distribution of magnetic fluxes. Magnetic field intensities of the exterior pole pieces are usually made much stronger than the inner ones and the unclosed magnetic field lines are pushed towards the substrate position in view of an independently control of substrate current density from the discharge power applied to the sputtered target. By this modification a highly dense plasma stream is conducted far from the target surface and an increased ion current density is generated on the substrate surface. In scientific literature there are presented some technical solutions for magnetic control of the substrate ion current density by configuration of coupled magnetic fields in view of reducing of the charge leakage (Figure 3.6) ***[Biró, 1998]***.

3.2.5.5. Reactive sputter deposition

The desired compound such as oxides, nitrides and carbides can be formed from an elemental or alloy target by introducing a reactive gas such as O_2, N_2 and CH_4 together with the noble gas usually argon (Ar), this process called the reactive sputter deposition. Reactive sputtering process is very non-linear and usually exhibits hysteresis curve as shown in Figure 3.7. The figure shows the variation of the discharge voltage and deposition rate with increasing and decreasing reactive gas flow ***[Rossnagel, 1999].***

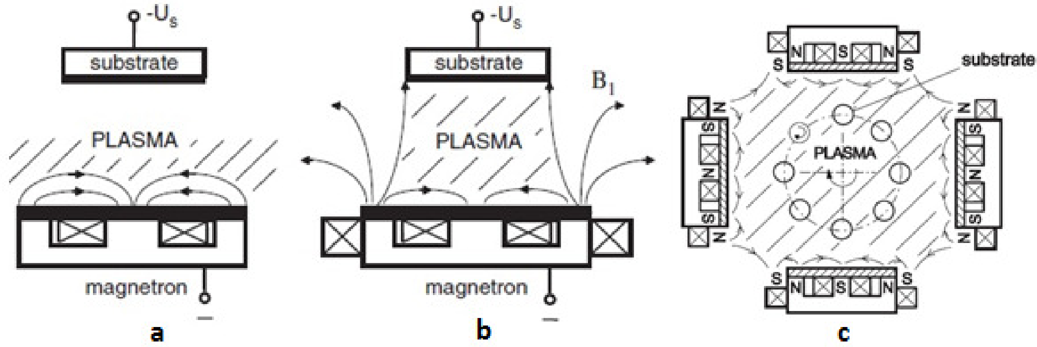

Figure 3.6. Schematic presentation of magnetic field distribution and plasma stream configuration for: a). conventional magnetron (CM); b) unbalanced magnetron (UM) of a single sputtering source, c.) coupled closed magnetic field of cuadrupol magnetron arrangement in view of reducing the charge carrier leakage from the plasma volume ***[Petrova et al, 1992],[Musil et al, 1996], [kadlec, et al, 1990].***

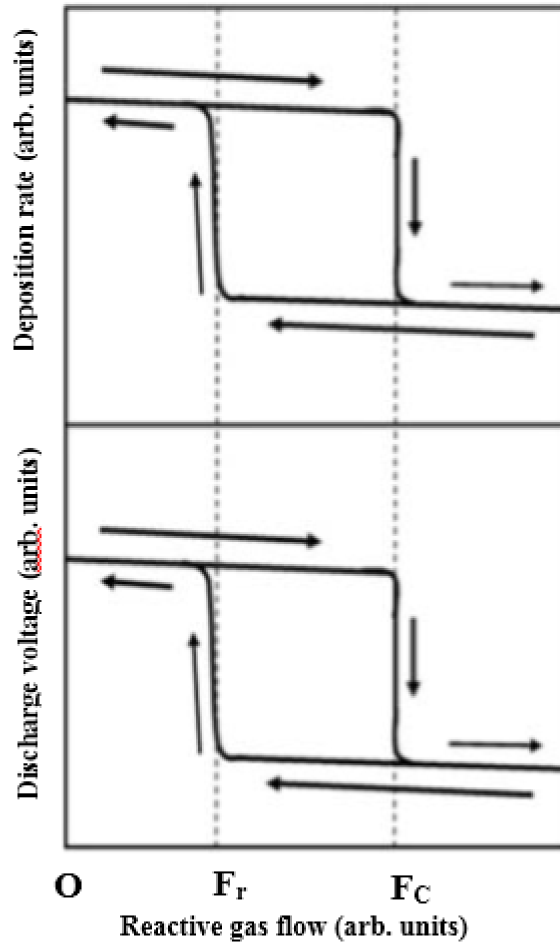

Figure 3.7. (Top) the deposition rate and (bottom) the discharge voltage as a function of reactive gas flow ***[Musil et al, 1996].***

There are two cases regarding this issue:

- First case, if the reactive gas flow is low that means the sputtering rate is high, compounds are preferentially formed on the substrate. In this situation, the compound layer on the target will be removed faster than it is formed. This mode of operation is referred to as the metallic mode and is characterised by high growth rates, but may result in under stoichiometric compositions of the deposited films due to the low partial pressure of the reacting gas.
- Second case, if the reactive gas flow is high that means the sputtering rate is very low. In this case, the partial pressure of the reactive gas is so high that compound formation on the target happens faster than the material can be sputtered, causing target contamination. Generally, it is found that no simple relationship between the flow rate and the partial pressure of the reactive gas exists. The transition from metallic to reactive mode exhibits hysteresis, as illustrated in Figure 3.7.

3.3. X-ray diffraction

3.3.1. Basic operation

There is no doubt that the X-ray diffraction (XRD) techniques are well known and provide us more information about the atomic structure, characterize the crystallographic structure, crystallite size, strain and preferred orientation in polycrystalline or powdered solid samples.

In this process the X-ray beam strike a crystal and scatters into many different directions according to the crystal orientation (texture).This phenomenon is known as elastic scattering. A regular array of atoms produces a regular array of spherical waves. Although these waves cancel one another out in most directions through destructive interference, but they add constructively in a few specific directions, determined by Bragg's Law:

$$2d_{hkl}\sin\theta = n\lambda \qquad 3.4$$

Where λ is the wavelength of the incident X-ray, θ is the incidence angle of electromagnetic radiation, n is the diffraction order (assumed to be 1) and d_{hkl} is the lattice spacing.

The Bragg's law is one of most important laws used for interpreting X-ray diffraction data as shown in Figure 3.8.

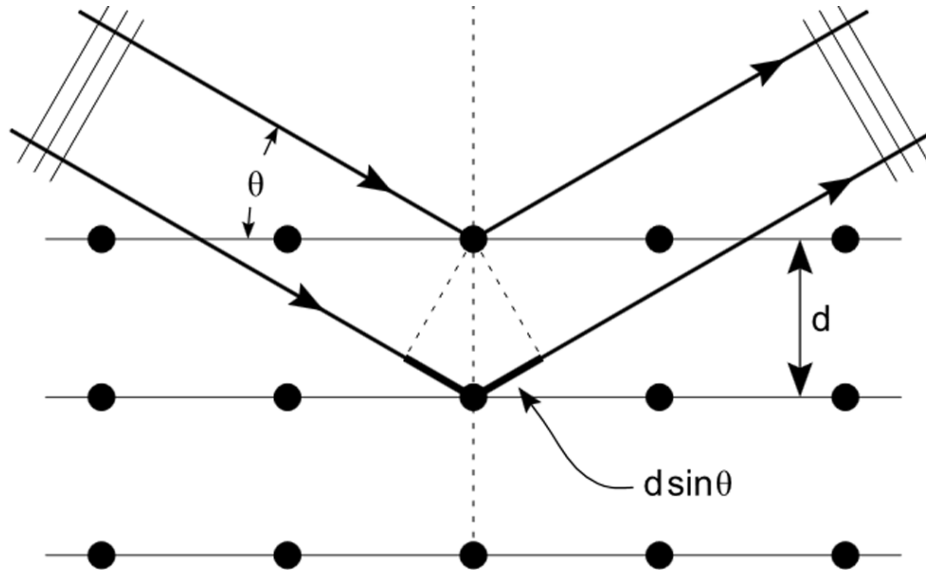

Figure 3.8. Bragg's reflection from a set of hkl planes having interplanar distance d.

3.3.2. Bragg-Brentano (θ-2θ) geometry

The Bragg–Brentano geometry (or θ-2θ) mode is illustrated in Figure 3.9**.** In this mode, the distance between the sample and detector is constant. It is essentially requires that distance from the source to the sample and the sample to the detector be equal. The detector and sample are linked such that as the detector rotates, the sample rotates through θ.

In the cubic system, the plane spacing is related to the lattice constant *a* and the Miller indices by the following relation:

$$d_{hkl} = \frac{a}{\sqrt{h^2+k^2+l^2}} \qquad 3.5$$

where d_{hkl} is the plane spacing between parallel closest planes with Miller indices h, k, and l, a = lattice constant (edge of unit cube).

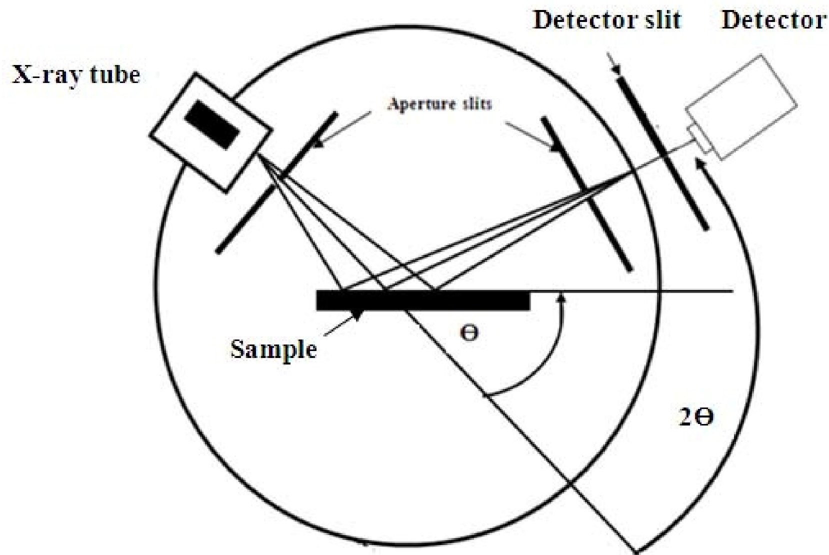

Figure 3.9. Schematic of Bragg–Brentano geometry.

3.3.3. Grain size estimation

Grain size can be considered as one of the most essential properties of the nano structured materials. Scherrer formula ***[Scherrer, 1918]*** is the most common method to determine the grain size from XRD pattern. The Scherrer formula is given by the following relation:

$$D_{\text{Scherrer}} = \frac{c\lambda}{\Delta(2\theta)\cos\theta} \qquad 3.6$$

Where $D_{Scherrer}$ is the average grain size, Δ(2θ) the full width at half maximum in radian, C is a constant which depends on the crystallite-shape (0.8 – 1.0), λ the X-ray wavelength and θ the Bragg-angle.

3.3.4. Determination of texture by X-ray diffraction

The texture is defined by the orientation distribution function of the crystallites irrespective of their sizes, shapes and arrangements***[Bunge, 1982].***The most common measurement technique of macro textures is X-ray diffraction ***[Cullity, 1956], [Barrett and Massalski, 1966].*** The two traditional techniques are the measurement of θ- scans by diffractometer, and measurement of pole figures at fixed

θ- angles. In case of thin films generally reflections methods are used (Figure 3.10), whereas transmission methods are used for self supporting thick films which can be detached from the substrate *[Adamik, 2000]*.

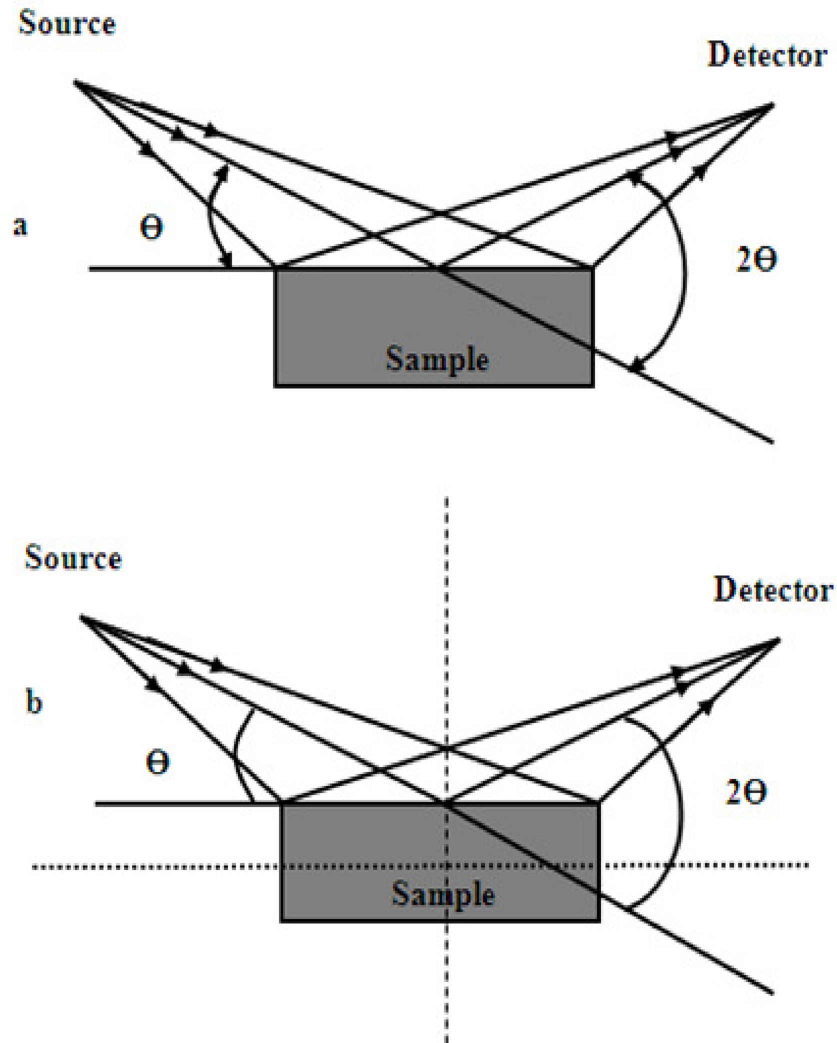

Figure 3.10. Schematic figures of arrangements of x-ray diffraction measurements of θ-2θ scans and pole figure ***[Adamik, 2000].***

The degree of preferred orientation can be estimated through a texture index:

$$T_{hkl} = \frac{I_{hkl/R_{hkl}}}{\frac{1}{n}\sum I_{hkl/R_{hkl}}} \quad 3.7$$

for n independently measured peaks, where R_{hkl} are the theoretical intensities of random orientation distribution ***[Valvoda and Jarvinen, 1990].***The texture index for randomly oriented films is T =1***[Adamik, 2000]***.

3.3.5. Pole figure

The measured intensities cannot be directly used for the evolution of textures, but correction should be made originating from the structure, absorption, multiplicity, etc. On traditional way to describe preferred orientations is by means of pole figure: this is a stereographic projection which shows the variation in pole density of a specific crystal direction with respect to the sample co-ordinates (Figure 3.11), or by inverse pole figure: which gives the poles of the sample co-ordinate system with respect to the crystal co-ordinate system in stereographic projection. This method of describing textures was first used by waver ***[Wever, 1924].***

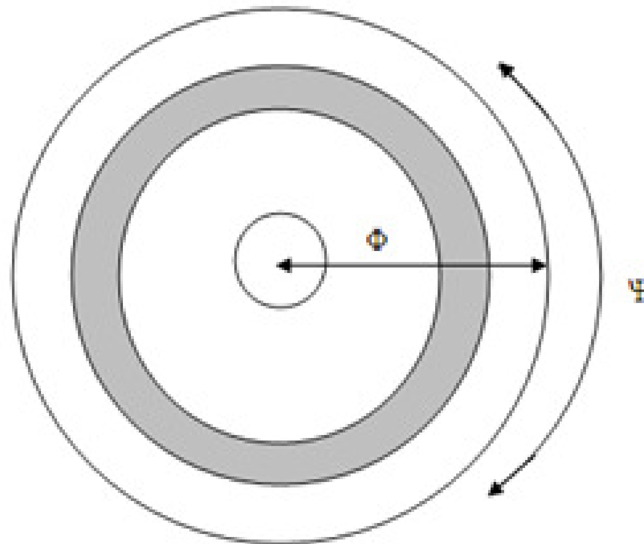

Figure 3.11.Schematic drawing a pole figure in case of a fiber texture.

Volume fractions can be calculated from pole figures also in case of multicomponent textures ***[Tomov and Bunge, 1979]. [Tomov et al, 1999], [Zeng et al, 1997].*** XRD intensity ratios of θ-2θ scans can be used for the rough evolution of textures.I_{111}/I_{200} is used for structure like Al ***[Vaidya and Sinha, 1981], [Mitsuzuka, 1992], [Campbell et al, 1993], [Yaspair et al, 1989],*** Cu ***[Gotoh et al, 1996],*** Ag

[Hoshi et al, 1985], Pd [Ziemann and kaz, 1983], and TiN [Meng and Eesley, 1995], [Petrov et al, 1993], [Jiang et al, 1995].

Pole densities at $\Phi = 0^0$ of specific (hkl) planes are appropriate for texture characterization in case of fiber textures. The pole density can be given as the ratio of crystalline volumes having a selected crystallographic orientation in the measured sample and in randomly orientated sample ***[Dunn and Walter, 1960].***

3.4. Transmission Electron Microscopy (TEM) for thin film microstructure analysis

The microstructure of thin films was investigated by transmission electron microscopy (TEM) using a Philips CM20 microscope. In the transmission electron microscopes monochromatic illumination (electron beam with energy from 100 KeV up to 1 MeV) is used to enhance the resolution of TEM Figure 3.12 ***[Williams and Carter, 1996].***The principles of image formation in the TEM are the following (figure 3.12): (1) the focused electron beam impinge on the extremely thin (30-60 nm) specimen, (2) the electron beam interacts with the specimen. This interaction results in the scattering of the transmitted electron beam. (3) The objective lens forms a diffraction pattern in the back focal plane with electrons scattered by the sample and combines them to generate an image in the image plane (first intermediate image). Thus, diffraction pattern and image are simultaneously present in TEM.

In selected area diffraction mode (SAED), an aperture in the plane of the first intermediate image defines the region for which the diffraction is obtained (Figure 3.12a). Which of them appears in the plane of the second intermediate image and is magnified by the projective lens on the viewing screen depends on the intermediate lens. Switching from real space (image) to reciprocal space (diffraction pattern) is easily achieved by changing the strength of the intermediate lens ***[Madou, 2012].***

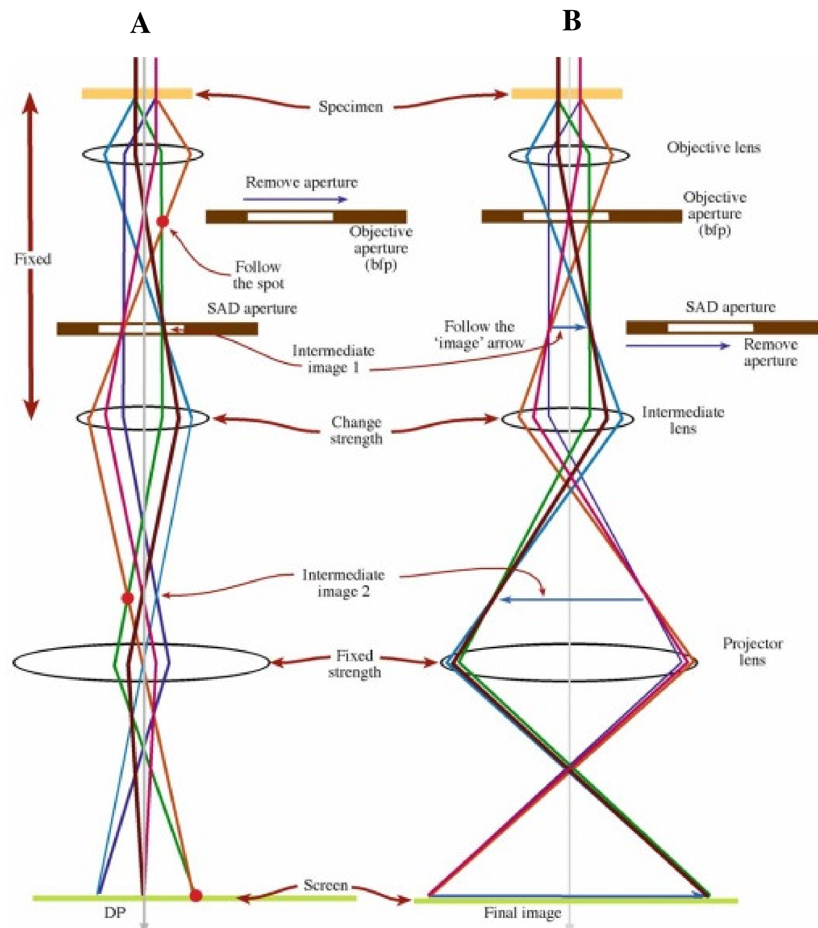

Figure 3.12. Schematic of a TEM ***[Williams and Carter, 1996], [Madou, 2012].***

When taking image (Figure 3.12b), an objective aperture is inserted in the back focal plane of the objective lens to select one or more beams that contribute to the final image (BF, DF, and HRTEM). Including the direct beam into the objective aperture bright field image is formed (BF), while selecting only scattered beams, dark field image (DF) can be received. Switching from real space (image) to reciprocal space (diffraction pattern) is easily achieved by changing the strength of the intermediate lens ***[Madou, 2012].***

3.5. Precession Electron diffraction PED-ASTAR technique

Precession Electron Diffraction (PED) was prepared by Vincent and Midgley in 1994 ***[Vincent and Midgley, 1994].*** PED technique has become a versatile tool of

Transmission Electron Microscopy (TEM) for enhancing its nanoscale characterization abilities. Detection and mapping of different crystallographic phases and orientations in a crystal structure required collection of high quality ED patterns. Electron beam Precession diffraction is extremely useful to obtain patterns with a large number of spots–almost twice as many compared with conventional selected area electron diffraction (SAED) and without dynamical effects (eg Kikuchi lines). Therefore, phase and orientation identification based on pattern matching between experimental procession patterns and simulated templates is very reliable and precise.

Some of the capabilities demonstrated by the technique are listed below:

- Pseudo-kinematical intensities are available under some experimental conditions as will be seen below;
- 3-dimensional datasets can be acquired under appropriate conditions from a single zone axis pattern. Low electron energy or large cell dimension in the optic axis are necessary, and Laue zone overlap must be avoided;
- Decreased intensity oscillation with thickness is observed (also occurs with thickness averaging);
- Greater tolerance to orientation errors, and specimens do not have to be perfectly on-zone to obtain symmetric patterns;
- Consistency of intensity values among different projections allows more accurate merging of multiple 2D projections into 3D datasets;
- Enhancement of fine detail in the solution of a large structure over that of conventional TED***;***
- If some structure factors are known, precession can be used to gain crystal thickness information with reasonable accuracy (within 10-15 nm).
-

In the experimental configuration for electron beam precession, the incident illumination (can be convergent or parallel) is tilted off zone to large angle φ typically 25-50 mrad corresponding to a reciprocal resolution on the order of an inverse °Angstrom at 200 kV and processed in a serial manner about the optic axis forming an effective hollow cone of illumination upon the specimen (Figure 3.13). The diffracted intensities, which constitute an off zone diffraction experiment for each individual tilt, are de-scanned in a complementary manner to the tilt scan signal restoring the spots to their default zone axis pattern locations.

This results in an effective integration of all tilts within the hollow illumination cone, i.e. around the edge of the cone. The PED pattern is thus an interpretable ZAP containing integrated intensities from off-zone conditions that are by nature less dynamical because fewer beams are simultaneously excited: strongly excited beams have little opportunity to exchange intensity with others (except for the transmitted).

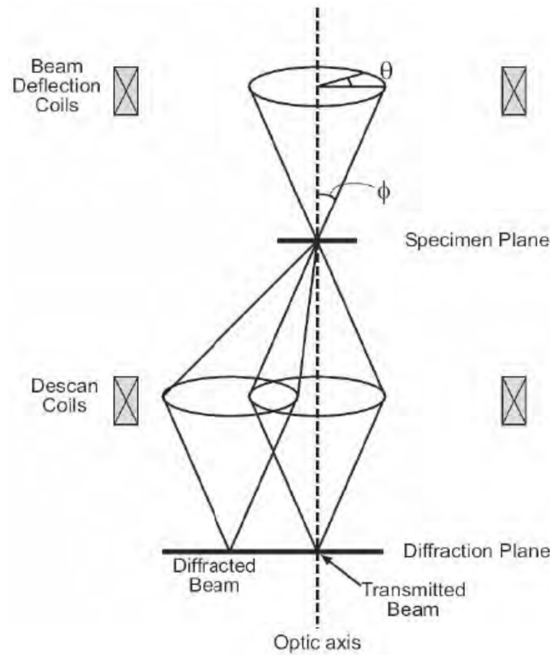

Figure 3.13. The schematic diagram of precession electron diffraction (PED). The beam is tilted off zone by angle φ using the beam tilt coils and serially processed through an angle Θ = 2π. A complementary de-tilt is provided below the specimen by de-scan coils to restore the zone axis pattern.

3.6. Principle of operation of Ultra micro–indentation system (UMIS)

Ultra micro-indentation system (UMIS) is one of the most common methods of hardness testing and elastic modules. As shown in Figure 3.14 this test consists of a hard tip (made from very hard material like diamond) which pressed into the sample surface with a known load.

The applied load increasing by a constant rate up to the maximum load P_{max}then the load is removed by the same rate under computer control. Figure 3.15 shows the relationship between the applied load and penetration depth which called P-h curves.

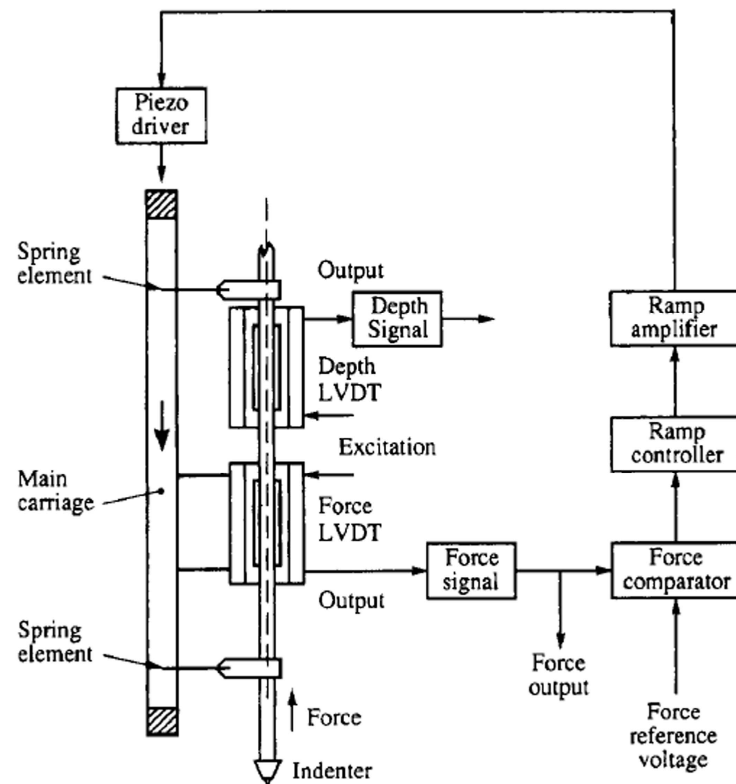

Figure 3.14. The Ultra micro- indentation system UMIS ***[Bell et al., 1991].***

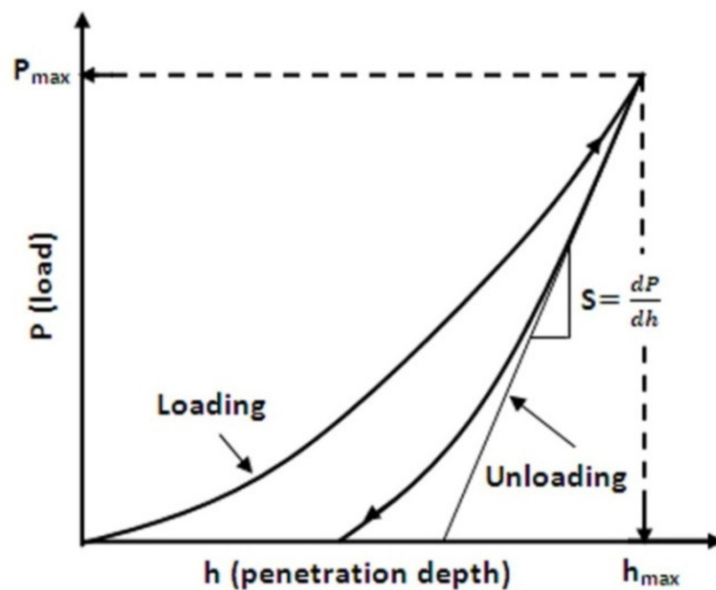

Figure 3.15. Typical form of a load-displacement curve ***[Oliver and Pharr, 1992], [Tuck et al., 2001].***

There are three important quantities must be measured from the P-h curves to calculate the hardness and elastic modules: The maximum load, P_{max}, the maximum penetration depth, h_{max} and the slope of the upper part of the unloading curveduring the initial stages of unloading $s = \frac{dP}{dh}$ as shown in Figure 3.15 ***[Oliver and Pharr, 2004].***The hardness H can be calculated according to the following equation ***[Oliver and Pharr, 1992]:***

$$H = \frac{P_{max}}{A} \tag{3.8}$$

Where A is the contact surface, and for a prefect sharp Berkovich indenter is given by where h_c is the contact depth at the maximum load as shown in Figure 3.16. The Contact depth h_c can be given as ***[Sneddon's, 1965]:***

$$h_c = h_m - h_s = h_m - \delta \frac{P_m}{S} \tag{3.9}$$

Where δ is the geometrical parameter which equal 0.75 for the case of Vickers and Berkovich indenters, h_m the maximum penetration depth, P_m the maximum load and S the slop as we discussed before.

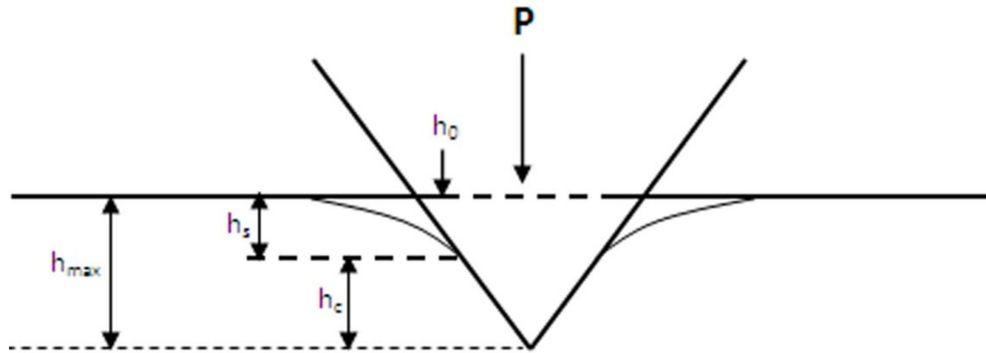

Figure 3.16. Schematic representation of the nanoindentation process **[Bhushan, 1999].**

The reduced elastic modulus E_r and elastic modulus E can be given as ***[Oliver and Pharr, 1992]:***

$$E_r = \sqrt{\frac{\pi}{A}} \frac{S}{2\beta}, \tag{3.10}$$

$$\frac{1}{E_r} = \frac{1-v_s^2}{E} + \frac{1-v_i^2}{E_i} \tag{3.11}$$

Where β is a constant which is specific to the indenter geometry, β_c= 1.034 for Berkovich $\beta = (3tan^2\theta)^{1/2,}$ where Θ is 65.3^0, $\nu_s$is the Poisson's ratio of the sample (TiN=0.25) and ν_i , Eiis Poisson's ratio and elastic modulus of the indenter, respectively.

3.7. Atomic force microscopy (AFM)

The surface morphology was investigated by atomic force microscopy (AFM) in tapping mode, using silicon tips with a tip radius of curvature smaller than 2 nm, purchased from Nanosensors (SSS-NCHR type). A low tip radius of curvature is needed to lessen the effect of tip – surface convolution effects, which blur the surface features that are comparable in size to the tip radius ***[Biro et al, 1999]***. Such a sharp AFM tip has allowed us to measure not only the columnar structure of the surface, but also to resolve the sub 10 nm fine structure of the columns.

3.8. Auger Electron Spectroscopy

Auger electron spectroscopy (AES) provides information about the chemical composition and binding conditions of the sample. This technique bases itself on Auger Effect. The Auger effect is a physical phenomenon in which the transition of an electron in an atom filling in an inner-shell vacancy causes the emission of another electron ***[Feldman and Mayer, 1986].***When an electron is removed from a core level of an atom, leaving a vacancy, an electron from a higher energy level may fall into the vacancy, resulting in a release of energy. Although sometimes this energy is released in the form of an emitted photon, the energy can also be transferred to another electron, which is ejected from the atom. This second ejected electron is called an Auger electron**.** Experimentally kinetic energy of the emitted Auger Electron is measured. In the case of KLL transition (Figure 3.17) kinetic energy of the emitted electron corresponds to the difference between the binding energy of the initial electronic state E_K^B and the binding energy of electrons in the shell L, E_L^B from which the Auger electron was ejected:

$$E_{kin} = E_k - E_{L1} - E_{L2}$$

Considering the many-electron relaxation effects (2 holes and 1 electron), there is:

$$E^z_{kin} = E^z_k - E^z_{L1} - E^z_{L2} - \Delta E(L_1 L_2)$$

in a simple model with

$$\Delta E(L_1 L_2) = ½ * (E^{z+1}_{L2} - E^{z}_{L2} + E^{z+1}_{L1} - E^{z}_{L1}) \quad 3.12$$

The term ΔE takes into account of the work function of the analyzer. These energy levels depend on the type of atom and the chemical environment in which the atom was located. Each emitted Auger electron is resulting from well-defined and identified transitions which are identified from the names of the core level which takes part in the transition.

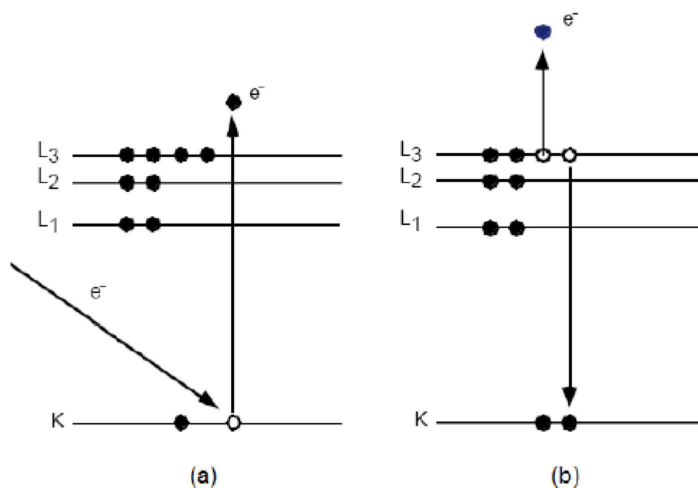

Figure 3.17. Scheme of Auger emission: (a) ionization of an atom by an impinging electron, (b) emission of an Auger electron.

3.9. X-ray photoelectron spectroscopy (XPS)

X-ray photoelectron spectroscopy is an electron spectroscopic method that uses x-rays to eject electrons from inner-shell orbitals. The kinetic energy, E_k, of these photoelectrons is determined by the energy of the x-ray radiation, $h\nu$, and the electron binding energy, E_b, as given by:

$$E_K = h\nu - E_b \quad 3.13$$

The experimentally measured energies of the photoelectrons are given by:

$$E_k = h\nu - E_b - E_w \quad 3.14$$

Where E_W is the work function of the spectrometer.

The electron binding energies are dependent on the chemical environment of the atom, making XPS useful to identify the oxidation state and ligands of an atom (Figure 3.18).

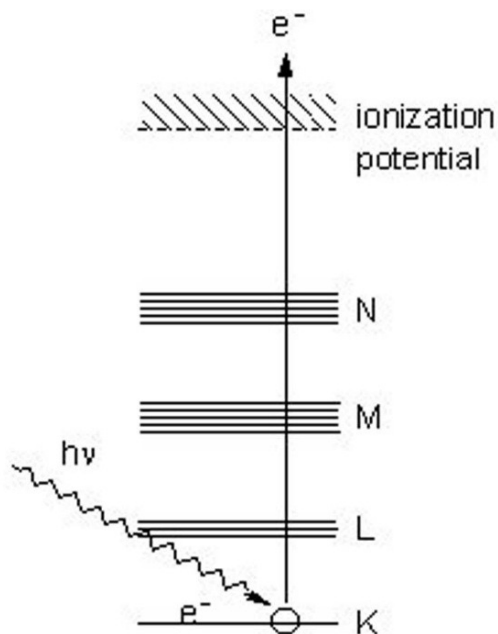

Figure 3.18. X-ray photoemission scheme.

3.9.1. Depth profiling using AES and XPS

While AES and XPS are surface sensitive techniques, a depth profile of the sample in terms of AES and XPS quantities can be obtained by combining a sequence of ion gun etch cycles interleaved with XPS measurements from the current surface. An ion gun is used to etch the material for a period of time before being turned off whilst XPS spectra are acquired. Each ion gun etch cycle exposes a new surface and the XPS spectra provide the means of analyzing the composition of these surfaces. For improving the depth resolution A. Barna and M. Menyhárd worked out a system by applying sample rotation and low energy glancing angle ion beam etching system ***[Barna et al, 1990], [Menyhárd, 1999].***

3.10. References

Adamic M., Texture evolution in polycrystalline thin film, PhD thesis (2000).

Aufderheide B. E., Sputtered thin film coatings, in Coatings technology handbook, Ed. Tracton, A.A., Taylor & Francis Group, Boca Raton, FL, USA, (2006) ch. 30, p. 1-10**.**

Barna A., Barna P. B. and Zalar. A., Analysis of the development of large area surface topography during ion etching, Vacuum, 40(1990) 115-120.

Barna P. B. and Adamik M., Growth mechanisms of polycrystalline thin films, Science and Technology of Thin Films eds.: **Matacotta F. C. and Ottaviani G**., World Scientific Publishing Co., (1995) p. 1-28.

Barna P. B., Impurity effects in the structural development of thin films, in de Segovia J. L., Proceedings of the 9th International Vacuum Congress and 5th International congress on solid surfaces, Madrid, Espanole el Vacio, Madrid, (1983) 382-396.

Barrett C. S. and Massalski T. B., Structure of Metals, 3rd ed., McGraw-Hill Book Company, New York, (1966*)* 343-345.

Bell T. J., Bendeli A., Field J. S., Swain M. V. and Thwaite E. G., The Determination of Surface Plastic and Elastic Properties by Ultra Micro-indentation, Metrologia 28 463 doi:10.1088/0026-1394/28/6/004(1991).

Bhushan B., Handbook of Micro/Nano Tribology, 2nd edition CRC press, Boca roton, FL (1999).

Biasiol G. and Sorba L., Molecular beam epitaxy: principle and applications, Crystal growth of materials for energy production and energy-saving applications, Fornari R, Sorba L, Eds. (Edizioni ETS, Pisa, 2001).

Biró D., Controlul magnetic al bombardamentului ionic de substrat prin confinarea magnetică a plasmei descărcării electrice. Raport de cercetare-contract MCT-Bucureşti (1998).

Biro L. P., I.Márk G., Gyulai J. and Thiry P. A., STM and AFM investigation of carbon nanotubes, Materials Structure 6(1999)104-108.

Bunge H. J., Crystallography of the polycrystalline, Material Science Forum, 157-162(1994)13-30.

Campbell A. N., Mikawa R. E. and Knorr D. B., Relationship between texture and electromigration lifetime in sputtered Al-1% Si thin films, Journal of Electronic Materials, 22(1993)589-596.

Cullity B. D., Elements of X-ray diffraction, Addison-wesley, London, (1956).

Dunn C. G. and Walter J. L., Orientation Density and Its Use in Quantitative Texture Studies, Journal of Applied Physics, 31(1960)827-833.

Fahrner W. R., Handbook of Nanotechnology and nanoelectronics, Materials, Devices, Measurement Techniques, (2005) 39-40.

Feldman L. C. and Mayer J. W, Fundamentals of surface and thin film analysis, (North-Holland, New York, *1986*).

Gautier C., Breton G., Nouaoura M., Cambon M., Charar S. and Averous M., Sulfide films on PbSe thin layer grown by MBE, Thin Solid Films, 315 (1998) 118–122.

Gotoh Y., Yoshi H., Amioka T., Kameyama K., Tsuji H. and Ishikawa J., Structures and properties of copper thin films prepared by ion beam assisted deposition, Thin Solid Films, 288 (1996)300-308.

Greene J. E., Thin film nucleation, growth, and microstructural evolution: An Atomic Scale View, in Martin P M, Handbook of deposition technologies for films and coatings, science, Application and Technology, Elsevier, (2010) 554-620.

He Y. B., Polity A., Alves H. R., Osterreicher I., Kriegseis W., Pfisterer D., Meyer B. K. and Hardt M., Structural and Optical Characterization of RF Reactively Sputtered $CuInS_2$, Thin Solid Films, 403–404 (2002) 62 – 65.

Holland L., Vacuum deposition of thin films, Chapman and Hall, London (1956).

Hoshi T., Proton-coupled transport of organic solutes in animal cell membranes and its relation to Na^+ transport, Japanese Journal of Physiology, 35(1985)179.

Jiang H., Tao K. and Li H., Structure of TiN_x ($0 < x < 1.1$) films prepared by ion beam-assisted deposition, Thin Solid Films 258(1995)51-55.

Kadlec S., Musil J., Munz W. D., Materials surface processing by directed energy techniques, Journal of Vacuum Science and Technology 8 (1990) 1318.

Lieberman M. A. and Lichtenberg A. J., Principles of plasma discharges and materials, Processing, 2nd ed. (John Wiley & Sons, Hoboken (2005) pp. 308-310.

Madou Marc J., Fundamentals of Microfabrication and Nanotechnology, (2012).

Martin P. M., Deposition technologies: an overview, Handbook of deposition technologies for films and coatings, science, application and technology, Elsevier, (2010) 1-31.

Meng W. J. and Eesley G. L., Growth and mechanical anisotropy of TiN thin films, Thin Solid Film 271(1995) 108–116.

Menyhard M., High-depth-resolution Auger depth profiling/atomic mixing, Micron 30(1999) 255-265.

Mitsuzuka T., Highly Preferred [111] Texture in Al films deposited on ultrathin metal underlayers, Japanese Journal of Applied Physics 31(1992) L1280-L1283.

Musil J., Rajsky A., Bell A. J., Matous J., Cepera M., and Zeman J., High-rate magnetron sputtering, Journal of Vacuum Science and Technology, A 14(4) (1996) 2187-219.

Ohring M, In the materials science of thin films, 2nd ed., Academic Press Inc., San Diego, USA (2002) Ch. 3-6.

Oliver W. C. and Pharr G. M., An improved technique for determining hardness and elastic modulus using load and displacement sensing indentation experiments, Journal of Material Research, 7(1992) 1564-1583.

Oliver W. C. and Pharr G. M., Measurement of hardness and elastic modulus by instrumented indentation: Advances in understanding and refinements to methodology, Journal of Material Research, 19 (2004) 3-20.

Petrov I., Adibi F., Greene J. E., Hultman L. and Sundgren J. E., Average energy deposited per atom: A universal parameter for describing ion- assisted film growth, Applied Physics Letters, 63(1993)36-38.

Petrov I., Adibi F., Greene J. E., Sproul W. D. and Munz W. D., Use of an externally applied axial magnetic field to control ion/neutral flux ratios incident at the substrate during magnetron sputter deposition, Journal of Vacuum Science and Technology, A 10(5) (1992) 3283-3287.

Petrov I., Barna P. B., Hultman L. and Greene J. E., Structural evolution during film growth, Journal of Vacuum Science and Technology, A 21 (2003) S117-S128.

Qasrawi A. F., Kayed T. S. and Ercan I., Fabrication and Some Physical properties of AgIn5S8, Thin Films Materials Science and Engineering, B 113 (2004) 73 –78.

Rossnagel S. M., Sputter deposition for semiconductor manufacturing, IBM Journal of Research and Development 43(1999), p. 163, ISSN 0018-8646.

Scherrer P., Bestimmung der Grösse und der Inneren Struktur von Kolloidteilchen Mittels Röntgenstrahlen, Nachrichten von der Gesellschaft der Wissenschaften, Göttingen, Mathematisch-Physikalische Klasse, 2(1918) 98-100.

Sigmund P., Theory of Sputtering. I. Sputtering Yield of Amorphous and Polycrystalline Targets, Physical Review, 184(1969) 383.

Sneddon I. N., The Stress on the boundary of an elastic half-plane in which body forces are acting , Proceedings of the Glasgow Mathematical Association 7(1965)48-54.

Stuart R. V. and Wehemer G. K., Sputtering Yields at Very Low Bombarding Ion Energies, Journal of Applied Physics, 33(1962)2345.

Thornton J. A. and Greene J. E., Handbook of deposition technologies for films and coatings", 2nd ed. (Noyes, Park Ridge, NJ, *1994*), p. 249.

Tomov I. and Bunge H. J., An analytical method for the quantitative determination of the volume fractions in fibre textures, Texture of Crystalline Solids, 3(1979) 73-83.

Tomov I., Adamic M. and Barna P. B., Texture and secondary extinction of vacuum deposition Ag films, Materials Science Forum, 321-324 (1999)400-405.

Tuck J. R., Korsunsky A. M., Bhat D. G. and Bull S. J., Indentation hardness evaluation of cathodic arc deposited thin hard coatings, Surface and Coatings Technology, 139(2001) 63-74.

Vaidya S. and Sinha A. k., Effect of texture and grain structure on electromigration in Al-0.5%Cu thin films, Thin Solid Films, 75(1981)253-259.

Valvoda V. and Jarvinen M., On the Harris texture index, power diffraction, 5(1990)200 -203.

Vincent R. and Midgley P. A., Double conical beam-rocking system for measurement of integrated electron diffraction intensities, Ultramicroscopy, 53 (1994) 271-282

waver F., Uber die Walzstrktur kubish Kristallisierender Metalle, Z. Physics, 28(1924)69-90.

Williams D. B. and Carter C. B., Transmission electron microscopy, A Textbook for Material Science (Plenum, New York, 1996).

Yaspir A. S., You L., Lu T. M. and Madden M., Partially ionized beam deposition of oriented films, Journal of Material Research, 4(1989)343-349.

Zeng Y., Zou Y. L. and Alford T. L., Texture in evaporated Ag thin films and its evolution during encapsulation process**,** Thin Solid Films, 307(1997) 89.

Ziemann P. and Kay E., Correlation between the ion bombardment during film growth of Pd films and their structure and electrical properties, Journal of Vacuum Science and Technology, A 1(1983)512 -1983.

Chapter 4

Literature survey

4.1. Motivation of the present work

Titanium nitride (TiN) has been used in cutting tools, medical device industry and also in the nanotechnology, because of its high hardness, high melting point, low density, chemical resistance, low coefficient of friction, lower wear rate, high evaporation temperature and metallic brightness ***[Sundgren, 1985]***, ***[Ettmayer and Lenguer, 1994]***, ***[Randhawa, 1988], [Subramanian and Strafford, 1993]***. All these properties strongly depend on the coating techniques and deposition conditions such as type of deposition technology and parameters, e.g. contamination, substrate temperature and substrate bias and the kind of charged particles as well.

The TiN based thin film systems are mostly used also as model material system of multicomponent films to understand the possible structures of nanocomposite thin films and their unique structure evolution. That is the reason why very many papers related to these films are published. The evaluation of them is practically not possible not only because of their very high number but also because in numerous of them neither the preparation conditions nor the structure characterizations are well documented. In this part I will review only some selected publications discussing the effect of oxygen doping, substrate temperature and substrate bias - as the most important parameters - on the structure and structure evolution of TiN thin films and to show why I have selected to study the effect of oxygen.

4.1.1. Effect of substrate temperature on structure evolution of TiN thin film

The effect of substrate temperature on the structure properties of magnetron sputtered titanium nitride thin films was investigated by Rao et al ***[Rao et al, 2013].*** In conclusion, they found that all of these films are polycrystalline with a preferred orientation (200). In addition, the hardness and Young modulus of these films ranged between 24–29 GPa and 326–388 GPa, respectively. The Young’s Modulus of these

films directly proportional to T_{200}, whereas inversely to T_{111}. That mean the nano-mechanical properties of TiN films are a function substrate temperature and of crystal orientation.

The microstructure evolution, as revealed by plan view and cross sectional transmission electron microscopy of Titanium nitride (TiN) films deposited by reactive magnetron sputter deposition were examined by L. Hultman et al ***[Hultman et al, 1987].*** They found that, at low temperatures ($T_s \leq 500^0$C) and in the absence of ion bombardment, the films are underdense and exhibit a pronounced columnar morphology. The addition of low-energy ($E_i \leq$ 200eV) ion irradiation during deposition using incident ion-to-neutral ratios Ji/Jn ≤1 in mixed Ar/N_2 plasmas results in the film densification. At higher incident flux ratios (Ji/Jn ≥4), low-energy ion irradiation provides increased apparent ad-atom mobility and hence larger grain size.

4.1.2. Effect of substrate bias on structure evolution of TiN thin film

Nanocrystalline TiN film deposited by reactive magnetron sputtering under different bias voltages was developed by Sung-Yong Chun ***[Chun, 2010].*** They found that, at high negative substrate bias voltage during the deposition of TiN coatings can lead to structural modification in terms of the film's preferred orientation, morphology and mechanical properties. A strong TiN (111) orientation is found when the thin film is deposited with increasing substrate bias voltage whereas a TiN (001) orientation is observed when the film is deposited at a low substrate bias voltage or without a bias. These changes in texture in the TiN films are due to one or a combination of such factors as resputtering, ion bombardment, plasma sheath, strain energy, surface free energy, and ad-atom mobility. The deposited nanocrystalline TiN films exhibit a characteristic pyramidal grain shape with crystallite sizes that decrease with increasing bias voltage, which is corresponds to an increase in the peak width in the XRD patterns. The substrate bias has a strong influence on both the surface roughness and the mechanical properties of TiN films.

Tentardini et al studied the modification of Titanium nitride (TiN) structure which prepared by magnetron sputtering process on <111> silicon under variation of substrate bias between -100V to + 100V ***[Tentardini et al, 2001].*** They found that the

hardness of the films increases with the increase of bias potential. On other hand the chemical composition of the films was analysed by RBS and EDS techniques showing that the films are only composed by Ti, Si, N and O.

Kumar et al ***[Kumar et al, 1988]*** studied the effect of substrate bias on the microstructure of TiN films deposited by reactive sputtering. It is found that the TiN thin films can be divided into two distinct groups depending on the substrate bias. At low substrate bias (< 65 V), the films have long columnar grains separated by voids which result in low density, low stress, and brown color. Atomic peening and ion-bombardment-enhanced surface diffusion result in high density, high compressive stress, and void-free films when proper bias voltage (> 65V) is applied to the substrate. By adjusting the substrate bias, the microstructure of the films can be controlled such that the voids are removed while keeping the intrinsic stress below 1-2 GPa. These films have been shown to be good diffusion barriers in the *AlITiN/Ti/Si* multilayer metallization scheme.

4.1.3. Effect of oxygen doping on structure evolution of TiN thin film

The binding state of incorporated oxygen in TiN thin films and the effect of in situ oxygen doping on their morphology and texture have been investigated by numerous authors ***[Colligon et al, 1994], [Zajac et al, 2009], [Radecka et al, 2011]***, ***[Drogowska et al, 2010], [Ensinger, 1991], [Vaz et al, 2003]***, ***[Braic et al, 2007], [Mehd et al, 2000], [Ismail et al, 2012].***The effect of oxygen addition on TiN films prepared by the arc ion plating method has been studied in details by Y. Makino et al ***[Makino et al, 1998].*** During this work they found that, with increasing the content of oxygen in the deposited films, the texture change from the 111 to 001. In addition, the lattice constant change was attributed to the substitution of nitrogen by oxygen and to the difference of content of interstitial atoms. At an oxygen concentration less than about 12at.%, however, the broadening of the (111) peak has been experienced, ***[Makino et al, 1994].*** This was attributed to the predominant effect of oxygen substitution to nitrogen. It is generally concluded that the texture changed from 111 to 001 with increasing oxygen content. Some authors have found a critical value of 15at.% oxygen concentration for this change of texture orientation ***[Chan and Lu, 2008]***, ***[Wu, 2008].*** Veprek has shown that impurities in general and oxygen in

particular, strongly degrade mechanical properties of the nanocomposites ***[Veprek, 2011]***. To the best of author's knowledge, the detailed structure analysis of the oxynitride thin films is still lacking.

Chen et al ***[Chen et al, 2013]*** studied the effect of various oxygen partial pressure (P_{O2}) on thin films prepared at 700^0C substrate temperature by pulsed laser deposition (PLD) using a TiN target. From the results they concluded that with increasing PO_2 the films evolved sequentially from TiN, TiN–TiO solid solution, TiO, corundum Ti_2O_3, anatase TiO_2 and finally became amorphous at the highest P_{O2} (~0.25 Torr). They undoped TiN film had a pronounced 001 texture and only (200) peak shown up in the XRD pattern. When the P_{O2} was increased slightly (from 2×10^{-6} to 5×10^{-5} Torr), the TiN (200) diffraction peak started to shift to higher diffraction angles and the peak width became broader with increasing P_{O2}. This was attributed to replacement of nitrogen by oxygen due to the higher activity of oxygen. Since the crystal structure of TiN and TiO is the same it is quite natural to conceive that the films are basically consisting of TiN–TiO solid solution, i.e. titanium oxynitride $TiN_{1-x}O_x$. However, the ionic radius of oxygen is smaller than that of nitrogen ion, which in turn might lead to the local lattice constant reduction. Consequently, although the diffraction peak appears to remain the same as that of pure TiN (100), the peaks evidently shifted to larger diffraction angles with increasing P_{O2}.

Zajac et al studied the incorporation of oxygen contamination into TiN which deposited by DC pulsed magnetron reactive sputtering from Ti target under controllable gas flows of Ar, N_2 and O_2 ***[Zajac et al, 2009].*** The authors concludes that, at lowest oxygen flow rate (n_{o2} = 0.46 sccm) display almost the same diffraction pattern corresponding to a well-crystallized structure isomorphic to fcc cubic TiN. Moreover these films show a preferential crystallographic orientation in the (111) direction. With increasing the oxygen flow rate (n_{o2} above 0.46 sccm) the reflections are shifted towards higher diffraction angles in the XRD pattern, attributed to decrease in the lattice constant and substitution of nitrogen by oxygen. At the highest oxygen flow rates n_{o2} = 1.32 sccm and n_{o2}=1.65 sccm the intensity of XRD peaks is quite small and their width is increasing indicating substantial decrease of the crystal size.

Several authors studied the effect of oxygen doping structure and properties of TiN coatings for improving their applicability in the various field of industrial applications:

Crystal orientation

- The crystal orientation change form <111> to <001> with increasing oxygen doping as observed by many authors ***[Wu et al, 2008], [Chan and Lu, 2008], [Makino et al, 1998].*** A careful literature survey on the correlation between mechanical properties and preferred orientation of TiN thin films revealed however quite contradictory results ***[Huang et al, 2005], [Chou et al, 2002], [Ma et al, 2006], [Ljungcrantz et al, 1996], [Chou et al, 2001], [Wittmer, 1981].***

Optical and electrical properties

- Titanium nitride films show low electrical resistivity and also good ohmic contacts to silicon ***[Nose et al, 1999], [Kumar et al, 1988], [Wittmer et al, 1981],*** whereas titanium oxynitride films provide a retarding diffusion barrier at the interface between a metal and silicon. It mainly occurs due to blocking of fast diffusion path by oxygen, which is leaving strong influence on the barrier performance ***[Nicolet and Barture, 1981].***
- Optical and electric properties, which depend significantly on the N/O ratio. Oxygen-poor TiN_xO_y has been widely used in many applications such as anti-reflective coating ***[Oyama et al, 1999],*** and biomaterials ***[Koerner et al, 2002],*** while oxygen-rich TiN_xO_y has been applied in thin film resistors ***[Cuong et al, 2007].*** Thin film resistors find a wide range of applications, such as flat panel displays, multichip modules, and the electrical shock protecting layers of IC tray (polymer) ***[Jung et al, 2003].***
- The transition between covalent metal nitride and ionic oxide controlled by the oxygen doping, which leads to change the band-gap, bandwidth, and crystallographic order between oxide and nitride, and hence the electric properties of materials and thus the optical ones ***[Vaz et al, 2003].***
- The colour of the films varies with the distinct N/O concentration of the films and hence the oxynitride exhibit more colour versatility than TiN, so it can be used as decorative coating ***[Chan and Lu, 2008].*** In addition, with a tuneable N/O ratio showed that they exhibit a complex structure and revealed an

intermediate behaviour between metallic TiN and insulating TiO_2 components ***[Chappe et al, 2003].*** Indeed titanium oxynitrides beneficiate from properties of metallic oxides (colour, optical properties) and nitrides (hardness, wear resistance) ***[Chappe et al, 2007].***

4.2. Motivation and the main aim of the present work

Titanium Nitride (TiN) is one of the most widely applied surface coating. TiN coatings are generally prepared by PVD (Physical Vapor Deposition) techniques. The structural and morphological properties of TiN films depend mainly on the preparation parameters and type of dopant (including contamination) which are incorporated during the film growth. One of the most important dopant is the Oxygen. It is also because Oxygen is the most general contamination in case of PVD deposition techniques and can be present at unexpected high level (up to 20 at.%) in the first stage of deposition if the degassing of the deposition system is not carefully done. On the other hand is has been also shown that a minute amount of Oxygen contamination hinders the formation of stable nanostructure in TiN/Si_3N_4 nanostructures. In TiN films prepared at substrate temperatures $0.2 < T_s/T_m < 0.3$ (Zone T) the <111> preferred orientation (PO) is the most commonly observed orientation of growth, however <001> and <220> PO have also been reported by changing the deposition parameters such as bias voltage N/Ti ion ratio, the ratio of N^+/N_2^+ and the oxygen doping. It has been pointed out that at oxygen contamination beyond 15at.% the 111 texture is changing to 001. On the other hand, Oxygen is used as additive to prepare oxynitride thin films. Therefore, it is important to understand the detrimental role of oxygen contamination in the structure evolution. Though there are case studies presenting information on the effect of oxygen additive on the structure and properties of TiN films the comprehensive structure characterization of the oxygen doped TiN films and the analysis by which mechanisms the oxygen can influence the structure evolution are practically missing.

The aim of this work is to follow the effect of oxygen additive on the structure and the texture evolution in TiN films deposited by reactive unbalanced magnetron sputtering. Experiments were carried out in the 0 < 20at.% Oxygen concentration range. The structure and structure evolution were investigated in details both in undoped films and in films with 20at.% oxygen content to be able to understand the

influence of oxygen on the structure and on the fundemental phenomena of film growth. As an application of these results it has been shown that crossover can develop between the 001 and 111 textures when changing the oxygen concentration during the film deposition.

For realizing a more comprehensive characterization of the film structure various methods were applied:

1. Cross-section(X-TEM), plane view transmission electron microscopy and selected area diffraction (SAED),
2. PED-ASTAR techinque adapted to the TEM for visuailizing the local orientation of crytals,
3. Energy dispersive X-ray microanalysis (EDX),
4. X-ray diffraction (XRD),
5. Auger (AES) and X-ray photoemission spectroscopy (XPS),
6. Atomic force microscopy (AFM),
7. Ultra-Micro-Indentation system (UMIS),
8. ProcessDiffraction computer program for quantitive determination of the phases and the degree of texture.

4.3. References

Braic M., Balaceanu M., Vladescu A., Kiss A., Braic V., Epurescu G., Dinescu G., Moldovan A., Birjega R. and Dinescu M., Preparation and characterization of titanium oxynitride thin films, Applied Surface Science, 253(2007)8210–8214.

Chan M. H. and Lu F. H., Preparation of titanium oxynitride thin films by reactive sputtering using air/Ar mixtures, Surface Coating and Technology, 203(2008) 614-618.

Chappe J. M., Martin N., Lintymer J., Sthal F., Terwagne G. and Takadoum J., Titanium oxynitride thin films sputter deposited by the reactive gas pulsing process, Applied Surface Science, 253 (2007) 5312–5316.

Chappe J. M., Martin N., Terwagne G., Lintymer J., Gavoille J. and Takadoum J., Water as reactive gas to prepare titanium oxynitride thin films by reactive sputtering, Thin Solid Films, 440 (2003) 66–73.

Chen S. C., Sung K. Y., Tzeng W. Y., Wu K. H., Juang J. Y., Uen T. M. , Luo C. W., Lin J. Y., Kobayashi T. and Kuo H. C., Microstructure and magnetic properties of oxidized titanium nitride thin films in situ grown by pulsed laser deposition, Journal Physics D: Applied Physics 46 (2013) 075002.

Chou W. J., Yu G. P. and Huang J. H., Deposition of TiN Thin Films on Si100/by HCD Ion Plating, Surface and Coating Technology, 140 (2001)206–214.

Chou W. J., Yu G. P., and Huang J. H., Mechanical Properties of TiN Thin Film Coatings on 304 Stainless Steel Substrates, Surface and Coating Technology, 149(2002)7–13.

Chun S. Y., Bias Voltage Effect on the Properties of TiN Films by Reactive Magnetron Sputtering, Journal of the Korean Physical Society, 56(2010)1134-1139.

Colligon J. S., Kheyrandish H., Lesnevsky L. N., Naumkin A., Rogozin A., Shakarban I. I., Vasilyev L. and Yurasova V. E., Composition and chemical state of titanium nitride films obtained by different methods, Surface and Coating Technology, 70(1994)9-17.

Cuong N. D., Kim D. J., Kang B. D., Kim C. S. and Yoon S. G., Characterizations of high resistivity TiN_xO_y thin films for applications in thin film resistors, Microelectronics Reliability, 47(2007) 752.

Drogowska K., Kim-Ngan N. T. H., Balogh A G, Radeck M, Brudnik A, Zakrzewska K and Tarnawski Z, Diffusion and chemical composition of TiN_xO_y

thin films studied by Rutherford Backscattering Spectroscopy, Surface Science, 604(2010)1010-1014.

Ensinger W., The influence of the process mode of ion beam assisted deposition on oxygen impurities in titanium nitride films, Nuclear Instruments and Methods in Physics Research B 56/57(1991)648-651.

Ettmayer P. and Lenguer W., Transition metal nitrides: solid state chemistry", in Encyclopedia of Inorganic Chemistry, R. B.King, Ed., John Wiley & Sons, 2nd edition (1994).

Huang J. H., Lau K. W., and Yu G. P., Effect of Nitrogen Flow Rate on Structure and Properties of Nanocrystalline TiN Thin films produced by unbalanced magnetron sputtering, Surface Coating and Technology, 191(2005)17–24.

Hultman L., Helmersson U., Barnett S. A., Sundgren J. E., and Greene J. E.," Low energy ion irradiation during film growth for reducing defect densities in epitaxial TiN(100) films deposited by reactive magnetron sputtering", Journal of Applied Physics, 61(1987)552.

Ismail I. M., Abdallah B., Abou-Kharroub M. and Mrad O., XPS and RBS investigation of TiN_xO_y films prepared by vacuum arc discharge, Nuclear Instruments and Methods in Physics Research B 271(2012)102-106.

Jung M. J., Nam K. H., Chung Y. M., Boo J. H. and Han J. G., The physiochemical properties of TiO_xN_y films with controlled oxygen partial pressure, Surface and Coatings Technology, 171(2003)71–74.

Koerner R. J., Butterworth L. A., Mayer I. V., Dasbach R. and Busscher H. J., Bacterial adhesion to titanium-oxy-nitride ($TiNO_X$) coatings with different resistivities: a novel approach for the development of biomaterials, Biomaterials 23 (2002) 2835.

Kumar N., Mc G. J. T., Pourrezaei K., Lee B. and Douglas E. C., Transmission electron microscopy studies of brown and golden titanium nitride thin films as diffusion barriers in very large scale integrated circuits, Journal of Vacuum Science and Technology A, 6(1988)1602.

Ljungcrantz H., Oden M., Hultman L., Greene J. E., and Sundgren J. E, Nanoindentation Studies of Single-Crystal (001), (011), and (111) Oriented TiN Layers on MgO, Journal of Applied Physics, 80 (1996) 6725–6733.

Ma C. H., Huang J. H., and Chen H., Nanohardness of Nanocrystalline TiN Thin Films, Surface and Coating Technology, 200(2006)3868–3875.

Makino Y., Nose M., Tanaka T., Misawa M., Tanimoto A., Nakai T., Kato K., and Nogi K., Characterization of Ti(N_xO_y) coatings produced by the arc ion plating method, Surface and Coating Technology, 98(1998)934-938.

Makino Y., Setsuhara Y. and Miyake S., Microstructure of titanium oxide films synthesized by ion beam dynamic mixing, Nuclear Instruments and Methods B91 (1994) 696.

Mehdi K. H., Alexander A. B. and Nobuhiko F., Formation of thin TiN_xO_y films by using a hollow cathode reactive DC sputtering system, Thin Solid Films, 372(2000)70-77.

Nicolet M. A. and Bartur M., Diffusion barriers in layered contact structures, Journal of Vacuum Science and Technology, 19(1981) 786.

Nose M., Nagae T., Yokota M., Saji S., Zhou M. and Nakada M., Electrical and colorimetric properties of TiN thin films prepared by DC reactive sputtering in a facing targets sputtering (FTS) system, Surface and Coatings technology, 119(1999)296-301.

Oyama T., Ohsaki H., Tachibana Y., Hayashi Y., Ono Y. and Horie N., A new layer system of anti-reflective coating for cathode ray tubes", Thin Solid Films 351(1999) 235.

Radecka M., Pamula E., Zajac A. T., Zakrzewska K., Brudnik A., Kusior E. Kim-Ngan N. T. H. and Balogh A. G., Chemical composition, crystallographic structure and impedance spectroscopy of titanium oxynitride TiN_xO_y thin films, Solid State Ionics, 192(2011)693-698.

Randhawa H., Hard coatings for decorative applications, Surface and Coating Technology, 36(1988)829–836.

Rao S. P., Rajagopalan R., Feby J., Sitaram D., Ashok Kumar T. and Nukala R., evolution of structure and mechanical properties of TiN films on SS 304LN, International Journal of Applied Ceramic and Technology, 10 (2013) 45–50.

Subramanian C. and Strafford K. N., Review of multicomponent and multilayer coatings for tribological applications, Wear 165 (1993)85–95.

Sundgren J. E., Structure and properties of TiN coatings, Thin Solid Films, 128 (1985) 21–44.

Tentardini E. K., Blando E. and Huber R., TiN structural modifications induced by bias voltage in a new dynamics controlled magnetron sputtering apparatuses, Nuclear instrument and methods in Physics Research, B 175-177(2001) 626-629.

Vaz F., Cerqueira P., Rebouta L., Nascimento S. M. C., Alves E., Goudeau P. and Riviere J. P., Preparation of magnetron sputtered TiN_xO_y thin films, Surface and Coating Technology, 174 –175 (2003) 197–203.

Veprek S., Recent attempts to design new super- and ultrahard solids leads to nanonized and nano-structured materials and coatings, Journal of Nanoscience and Nanotechnology, 11(2011) 14-35.

Wittmer M., Noser J. and Melchior H., Oxidation kinetics of TiN thin films, Journal of Applied Physics 52(1981)6659.

Wu Y., Wu X., Li G. and Li G., Microstructure and mechanical properties of reactively sputtered Ti(O,N) coatings, International Journal of Refractory Metals and Hard Materials, 26(2008)461-464.

Zajac A. T. Radecka M., Zakrzewska K., Brudnik A., Kusior E., Bourgeois S., Marco de Lucas M. C. and Imhoff L., Structural and electrical properties of magnetron sputtered Ti(ON) thin films: The case of TiN doped in situ with oxygen, Journal of Power Sources, 194 (2009) 93–103.

Chapter 5

Experimental results

5.1. Thin film preparation and measurements

Titanium oxynitride thin film coatings were deposited in a home made laboratory scale magnetron sputtering equipment. The octagonal all-metal high vacuum chamber of 75 liter volume was evacuated by a 540 l/s turbo-molecular pump producing $2x10^{-4}$ Pa base pressure. Three independent sputter sources were closely arranged side by side on the neighboring vertical walls. The magnetic fields of closely disposed UB magnetrons arranged on an arc segment were highly interacting, leading to a far extended active plasma volume. In the present deposition experiments only the centrally positioned magnetron source was active, while the adjacent two magnetron sources contributed only in generating the closed magnetic field. A planar rectangular metallic Ti target (165 x 85 x 12 mm^3 in size) of 99.95 % purity (PLANSEE GmbH) was used. The discharge plasma was excited reactively in a mixture of Ar, N_2 and O_2 by a close-loop controlled dc power supply. The discharge power for each deposition run was 500 W ***[Jakab-Farkas et al, 2009].***

The flow rate of Ar gas was stabilized by a solenoid valve actuated mass flow controller (MFC-Granville Phillips S 216), and measured by a GFM 17 Aalborg mass flow meter. The N_2 throughput was controlled by Aalborg DFC 26 digital mass flow controller. Admission of oxygen gas was manually controlled by using a high precision needle valve (Granville Phillips type). In the deposition process the total pressure of mixed gases were maintained at constant value by changing the conductance in down stream of the gases via adjusting a throttle valve in the pumping system. The undoped sample TO_4 discussed in the present work was deposited in a mixture of Ar+N_2 atmosphere with a total pressure $p_{N2+}p_{Ar}$ = 0.5 Pa. The flow rate of N_2 was 3 sccm establishing P_{N2}= 0.1 Pa partial pressure. Titanium oxynitride thin film coatings have been prepared at the same nitrogen flow rate while the oxygen flow rate was varied. The partial pressure in case of samples TO_12 and TO_11 is P_{O2}=$4x10^{-2}$ Pa and Po_2=$1.1x10^{-2}$ Pa respectively.

The thin films were deposited on <100> Si single crystal covered by native oxide. The target-to-substrate distance was kept constant at d_{T-S} =110 mm in all experiments. The substrates have been positioned in static mode on a substrate holder maintained at ground potential. The substrate holder was electrically heated for a temperature of T_s= 400 ºC measured by a K-type chromel-alumel thermocouple which was positioned on the back side of the substrate holder. The thickness and growth rate of the deposited thin films was determined by an oscillating quartz crystal monitor.

Prior to starting the reactive deposition process the target surface was plasma-etched for 10 min at 0.8 Pa by dc glow discharge in argon atmosphere. During the sputter cleaning of the target surface the substrate was shielded from deposition of vapor flux.

The microstructure of the films was investigated by transmission electron microscopy technique both on cross sectional and plane view specimens. PHILIPS CM20 transmission electron microscope working at 200 kV and equipped with a Ge-detector NORAN EDX analyzer was applied for the conventional TEM investigation and chemical analysis. The high resolution TEM investigation was carried out in a 300 kV JEOL 3010 TEM and an attached GATAN TRIDIEM Image FILTER was used for elemental mapping. The ProcessDiffraction software ***[Lábár, 2005]*** made possible both the qualitative and quantitative evaluation of the selected area electron diffraction patterns.

The surface morphology was investigated by atomic force microscopy (AFM) in tapping mode, using silicon tips with a tip radius of curvature smaller than 2 nm, purchased from Nanosensors (SSS-NCHR type). A low tip radius of curvature is needed to lessen the effect of tip – surface convolution effects, which blur the surface features that are comparable in size to the tip radius ***[Biro et al, 1999].*** Such a sharp AFM tip has allowed us to measure not only the columnar structure of the surface, but also to resolve the sub 10 nm fine structure of the columns.

The nanohardness was measured by Ultra-Micro-Indentation system (UMIS) instrument at 10 mN load and 10 mN/min rate ***[Bell et al, 1991], [Latellaa et al,***

2006], [Ma et al, 2005], [Dirras et al, 2011]. The maximum penetration depth of the tip was 150 nm.

The chemical composition and its variation along the thickness of the films were investigated by Auger electron spectroscopy (AES) and x-ray photon electron spectroscopy (XPS) depth profiling. At the evaluation of the XPS spectra, the atomic concentrations were calculated by applying the relative sensitivity factor (RSF) method after removing the background using the Shirley method. The used RSF parameters were: 1.8 for Ti_2p, 0.42 for N1s and 0.66 for O_1s ***[Briggs and Seah, 1990], [Guillot et al, 2001].*** The structure and texture of the films were investigated by X-ray diffraction (XRD in Bregg-Brentano configuration using a Bruker AXS D8 Discover diffractometer equipped with a 2D position sensitive (GADDS) detector.

5.2. Structure of undoped Titanium nitride (TiN) thin film (Sample TO_4)

5.2.1. X-ray diffraction

Figure 5.1 shows the θ-2θ XRD spectrum of the undoped TiN coating. According to this analysis the film has a strong <111> fiber texture with a texture coefficient $T_C \approx 1$. This value was calculated according to the equation 3.7; also the <222> peak is observed in the pattern this peak is original also from the {111} plane. In addition, the other reflections such as <200> are extremely weak but we can estimate the intensities of these refractions from the original sheet.

The structure parameters of undoped TiN are summarized in Table 5.I. The undoped TiN film has peaks at 2θ values of 36.7°, 42.45° and 78.1° which correspond to the reflections from the (111) , (200) and (222) planes of the cubic TiN structure according to JCPDS card number 38-1420. One can identify that, the lattice distances (d) and lattice constants (a) almost agree with the standard values. As shown in Table 5.I, the full width at half maximum (FWHM) values are 0.295, 0.468 and 0.283 for the {111}, {200}, and {222} planes respectively.

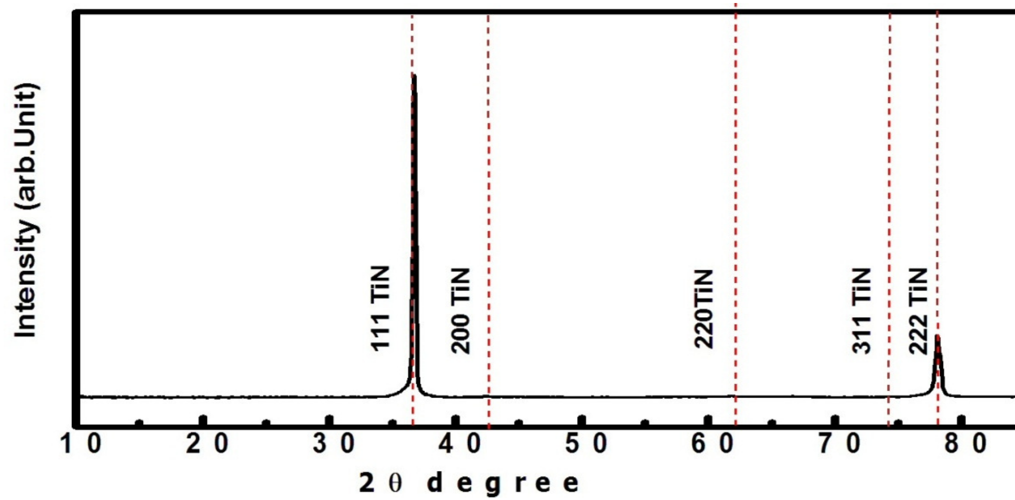

Figure 5.1. The θ - 2θ XRD spectrum of the undoped TiN film.

Table 5.I. Structure parameters calculated for undoped TiN thin film

Planes	*2Θ*	*Lattice distance, d (A)*	*Lattice constant a (A)*	*FWHM*	*Grain size D(nm)*
111	*36.70*	*2.446*	*4.236*	*0.295*	*6.2*
200	*42.45*	*2.126*	*4.253*	*0.468*	*3.2*
222	*78.1*	*1.222*	*4.233*	*0.283*	*6*

5.2.2. ProcessDiffraction analysis of the SAED

Figure 5.2 shows the selected electron diffraction patterns (SAED) taken on the whole thickness of film analyzed by "ProcessDiffraction" program and confirm that the structure of the sample is TiN (JCPDS card number 38-1420) ***[Lábár, 2005].*** On other hand the strong <111> texture is in accordance with the XRD pattern shown in Figure 5.1.

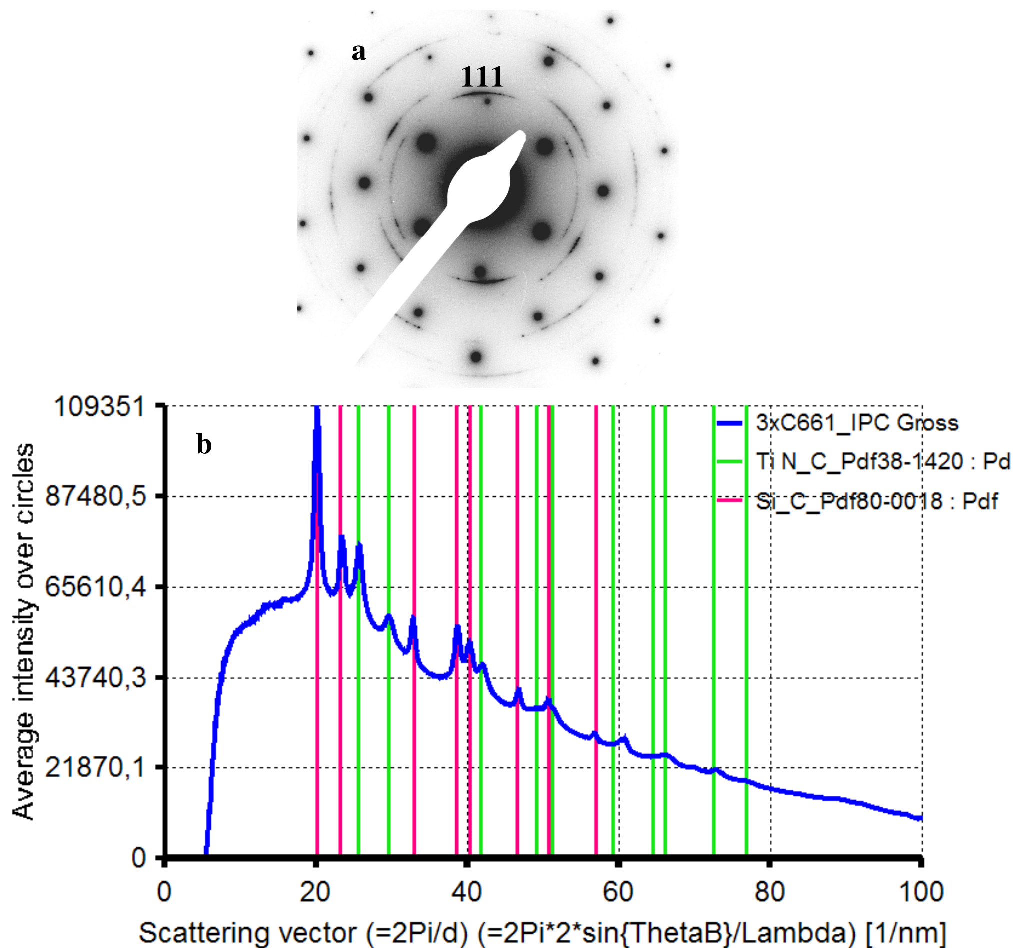

Figure 5.2. a)-Selected-area electron diffraction (SAED) pattern and b)-Circularly averaged intensity in SAED as a function of the length of the scattering vector for undoped TiN film.

5.2.3. X-ray photoelectron spectroscopy (XPS) and Auger electron spectroscopy (AES) analysis

The chemical composition of the film determined by Auger electron spectroscopy (AES) depth profiling was homogenous along the thickness. X-ray photoelectron spectroscopy (XPS) measurements provided information about the N/Ti ratio in the film which was 1.12 and also the film contained 4at.% oxygen concentration.

5.2.4. Cross section transmission electron microscopy (X-TEM)

The cross sectional transmission electron (X-TEM) microscopic image of the undoped TiN (containing 4 at.% oxygen) film together with the selected area diffraction patterns taken from the various domains along the thickness are shown in Figure 5.3.

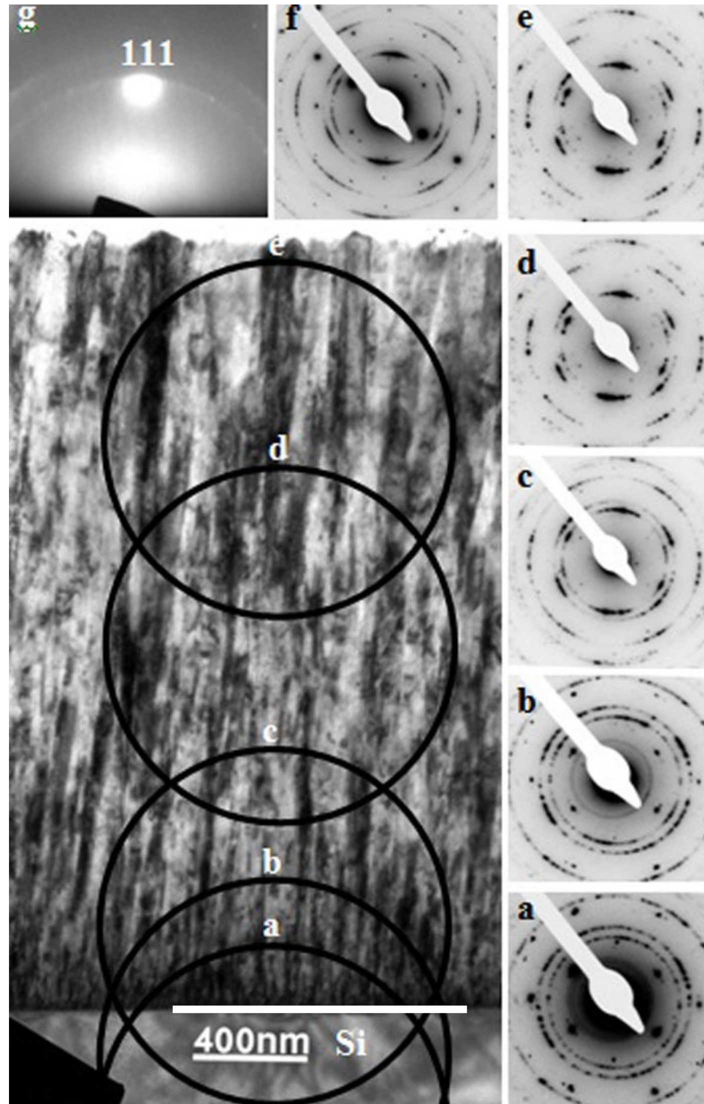

Figure 5.3. X-TEM image of the undoped TiN film and selected area electron diffraction patterns (SAED) taken on the thickness domains marked by circles. Inset g is the reflection high energy electron diffraction pattern taken on the surface of the as deposited film. The area of SAED pattern of inset f includes the substrate Si single crystal and the whole cross section of the film.

The selected area diffraction pattern (SAED) including the substrate Si crystal and the whole cross section of the film (Figure 5.3 inset f) clearly demonstrate the <111> fiber texture in accordance with the XRD pattern shown in Figure 5.1. The reflection high energy diffraction pattern taken on the surface of the film (Figure 5.3 inset g) show that the film surface is composed only by <111> oriented crystals. SAED pattern (Figure 5.2 inset a) including the 100 oriented silicon single crystal Si substrate and the very thin thickness domain of the film at the substrate indicates that the small TiN crystals developed on the substrate are randomly oriented. The diffraction patterns taken successively from thicker domains of the film (Figure 5.3 insets c and d) clearly demonstrate that the <111> texture becomes stronger with the thickness. According to Figure 5.3 insets e and f the upper part of the film is composed mainly from <111> oriented columns, which is also supported by the dark field image taken by the 111 reflection (Figure 5.4).

Figure 5.4. Dark field X-TEM image of the undoped TiN film taken by the 111 TiN reflection the crystals marked by arrow demonstrate the V-shaped morphology of the <111> oriented crystals in the thickness domain near to the substrate.

The crystal marked by an arrow is representative for this structure. It forms a column with V-shaped morphology near to the substrate which is continued in a parallel sided column. That is the characteristic structure of zone T of the structure zone models.

It can be concluded that under our experimental conditions the structure of TiN with low oxygen contamination has columnar morphology with V-shaped grains and the preferred orientation is <111> along the thickness (zone T structure).

5.2.5. Nanoidentation measurements

During the loading period of the test the indenter penetrates into the sample at constant velocity till the load reaches it maximum value (P_m). The same velocity is applied in the unloading period when the pyramid moves upwards. Figure 5.5 shows a typical load-displacement curve with the 10mN maximum load and the maximum indentation depth was about 150 nm. The hardness and Young's modulus for the undoped TiN (containing 4at. % oxygen) films are 18 GPa and 432 GPa respectively.

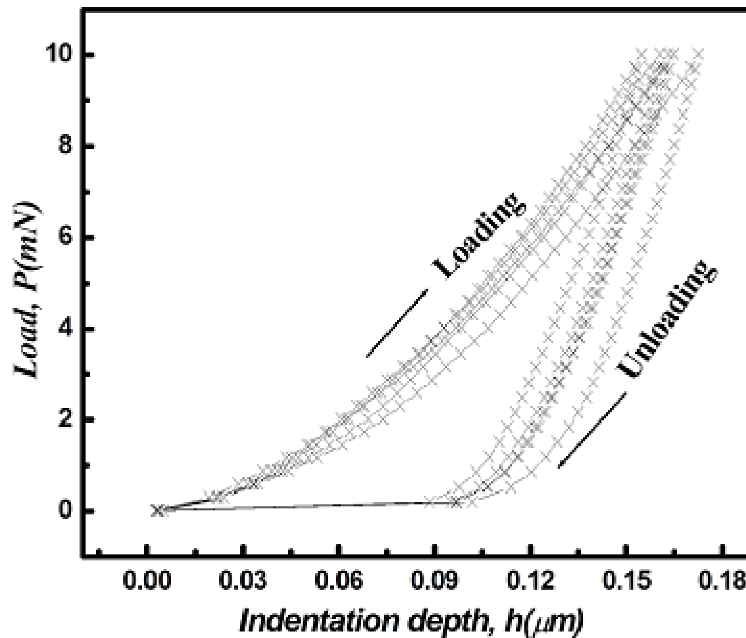

Figure 5.5. Typical load vs. displacement curves for umdoped TiN thin film at 10mN load.

5.3. Structure of oxygen doped $Ti_{0.45}O_{0.20}N_{0.35}$ oxynitride thin film (Sample TO_12)

5.3.1. X-ray diffraction

Figure 5.6 shows θ-2θ X-ray diffractogram of oxygen doped $Ti_{0.45}O_{0.20}N_{0.35}$ oxynitride film. The film has a strong <200> fiber texture with a texture coefficient $T_C \approx 1$ instead of <111> fiber texture for undoped TiN as seen in figure 5.1. The other reflections are extremely weak but we can estimate the intensities of these reflections from the original sheet. The $Ti_{0.45}O_{0.20}N_{0.35}$ oxynitride film has peaks at 2θ values of 37.1°, 43.19°, 62.75° and 75.2° which correspond to the reflections coming from the {111},{200}, {220} and {311} planes, respectively. The XRD peak positions are shifted towards higher angles when compared with the undoped TiN film and the JCPDS card number 38-1420. It means that lattice parameter decreases with increasing the oxygen content. Table 5.II shows the lattice distance (d), lattice constant (a), full width at half maximum (FWHM) and grain size (D).

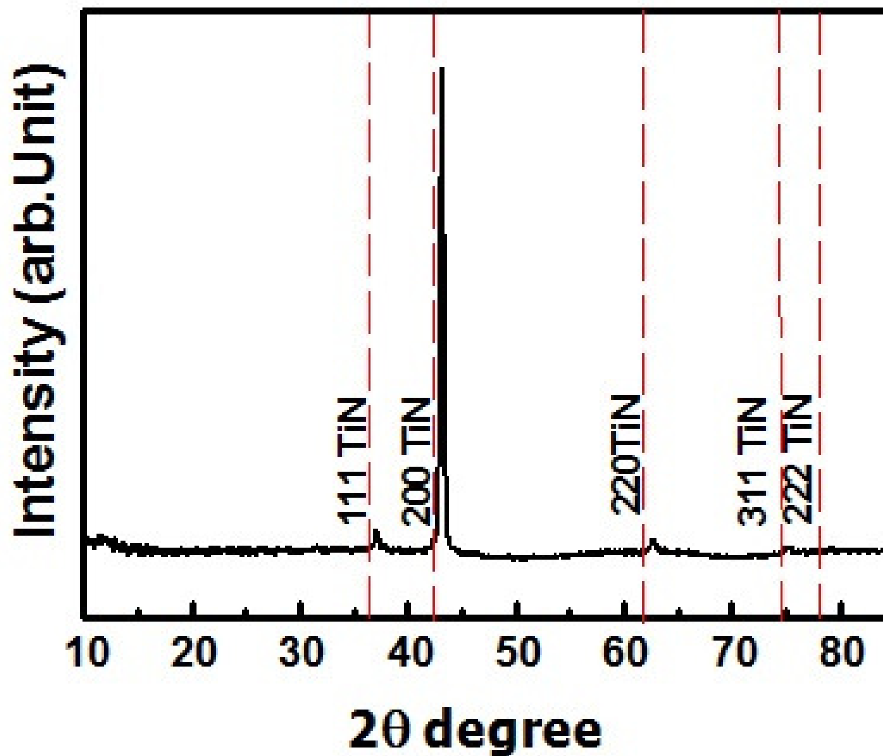

Figure 5.6. The θ - 2θ XRD spectrum of the oxygen doped $Ti_{0.45}O_{0.20}N_{0.35}$ oxynitride film.

Table 5.II. Structure parameters calculated for $Ti_{0.45}O_{0.20}N_{0.35}$ oxynitride film

planes	*2Θ*	*Lattice distance, d (A)*	*Lattice constant a (A)*	*FWHM*	*Grain size D(nm)*
111	*37.1*	*2.4245*	*4.199*	*0.44*	*3.32*
200	*43.19*	*2.090*	*4.180*	*0.326*	*4.57*

5.3.2. X-ray photoelectron spectroscopy (XPS) and Auger Electron Spectroscopy (AES) analysis

The chemical composition and the chemical states of constituents present in the $Ti_{0.45}O_{0.20}N_{0.35}$ oxynitride film have been determined by Auger electron spectroscopy (AES) depth profile analysis and by X-ray photoelectron spectroscopy (XPS). Figure 5.7 shows part of the AES depth profile; it shows the O/Ti ratio as a function of the depth. It is clear that the ratio of O/Ti is constant along the thickness. XPS analyses were taken at various depth, to reveal the more detailed chemical composition. According to the XPS measurements the N/Ti ratio in the film was 1.12 and the film contained 20at.% oxygen concentration. The XPS can also identify the various compound formations present; the deconvolution procedure is shown in Figure. 5.8.

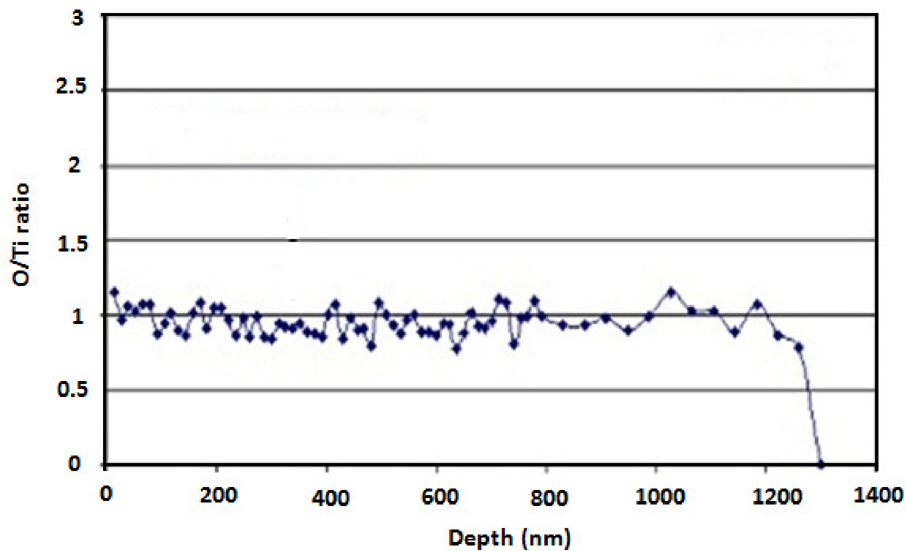

Figure 5.7. Auger electron spectroscopy (AES) depth profile of oxygen doped $Ti_{0.45}O_{0.20}N_{0.35}$ oxynitride film.

Figure 5.8 shows the XPS spectrum for $Ti_{0.45}O_{0.20}N_{0.35}$ oxynitride film. There are two principal peaks close to 464 and 458 eV which most likely correspond to Ti2 p1/2 and Ti2p3/2 contributions of titanium nitride, and also contained the constituents spectra TiN, TiO_2 and TiN_XO_y. The fitted spectrum is the sum of the spectra of constituents also shown in Figure 5.8.

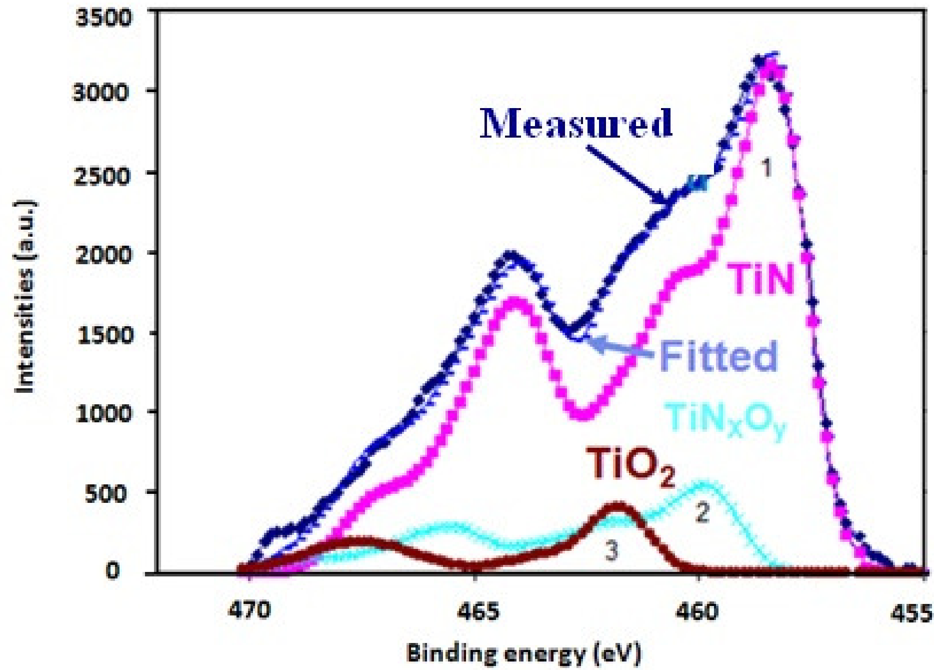

Figure 5.8. X-ray photoelectron spectroscopy (XPS) spectrum for oxygen doped $Ti_{0.45}O_{0.20}N_{0.35}$ oxynitride film.

Table 5.III shows the distribution of Ti in the various compounds on oxygen doped $Ti_{0.45}O_{0.20}N_{0.35}$ oxynitride film (concluded from XPS analysis). The TiO_2 second phase revealed by XPS were not recognized by XRD.

Table 5.III. Distribution of Ti in the various compounds on $Ti_{0.45}O_{0.20}N_{0.35}$ oxynitride film

TiN, TiN_uO_v $u > v$, $u >> v$	TiN_XO_y $X < y$	oxides TiO_2
79at.%	*13 at.%*	*8at.%*

5.3.3. Determination of the phase composition by the ProcessDiffraction analysis of the SAED

The XRD like intensity distribution in Figure 5.9 b of the SAED pattern evaluated by the ProcessDiffraction tool ***[Lábár 2005].*** The markers are related to the cubic TiN (JCPDS card: No.38-1420) and tetragonal TiO_2 (JCPDS card: No.82-0514) phases. We can conclude that this film consist of two phases the cubic TiN and tetragonal TiO_2. The types of diffraction rings indicated that the TiN crystals are larger while the TiO_2 phase consist of very small crystallites. It is also to be shown that, both phases are textured and orientationally related.

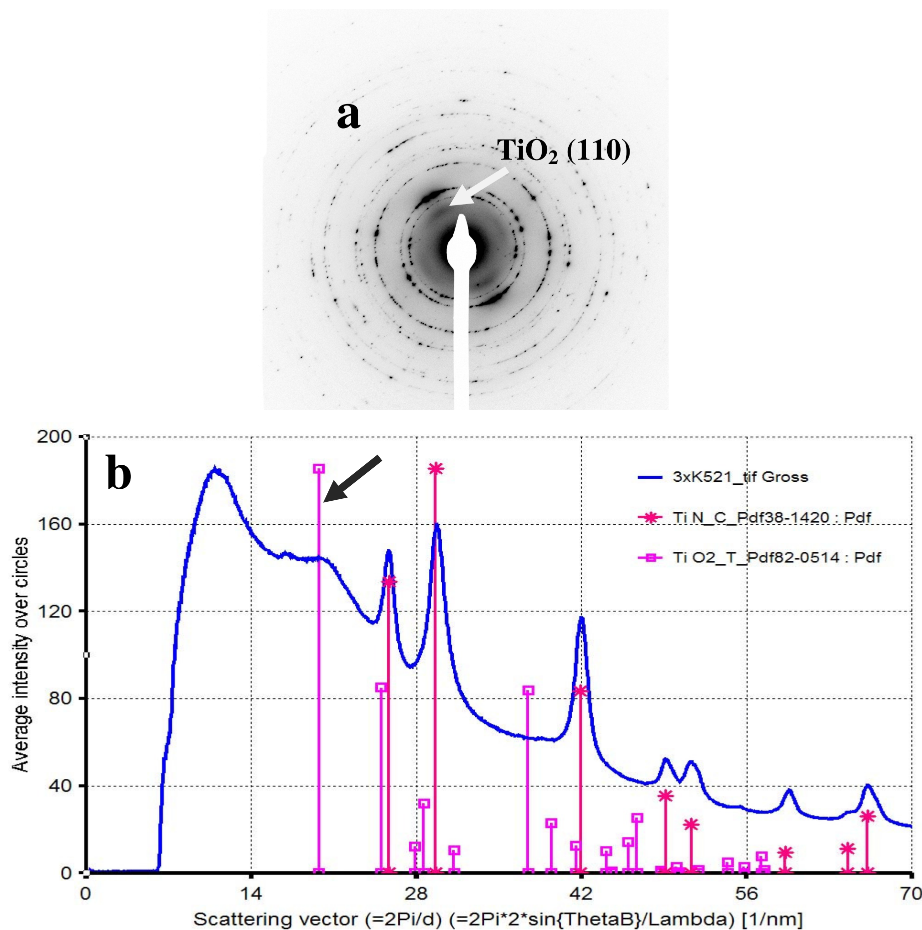

Figure 5.9. ProcessDifraction software analysis for oxygen doped $Ti_{0.45}O_{0.20}N_{0.35}$ oxynitride film.

5.3.4. Cross section transmission electron microscopy for oxygen doped $Ti_{0.45}O_{0.20}N_{0.35}$ oxynitride film

The X-TEM microscopic image of the $Ti_{0.45}O_{0.20}N_{0.35}$ oxynitride film together with the selected area diffraction patterns (SAED) taken from the various domains along the thickness are shown in figure 5.10. The SAED including the substrate Si crystal and the whole cross section of the film (figure 5.10 inset e) clearly demonstrates the <100> fiber texture, these results agree well with the XRD pattern shown in Figure 5.6. The reflection high energy electron diffraction pattern taken on

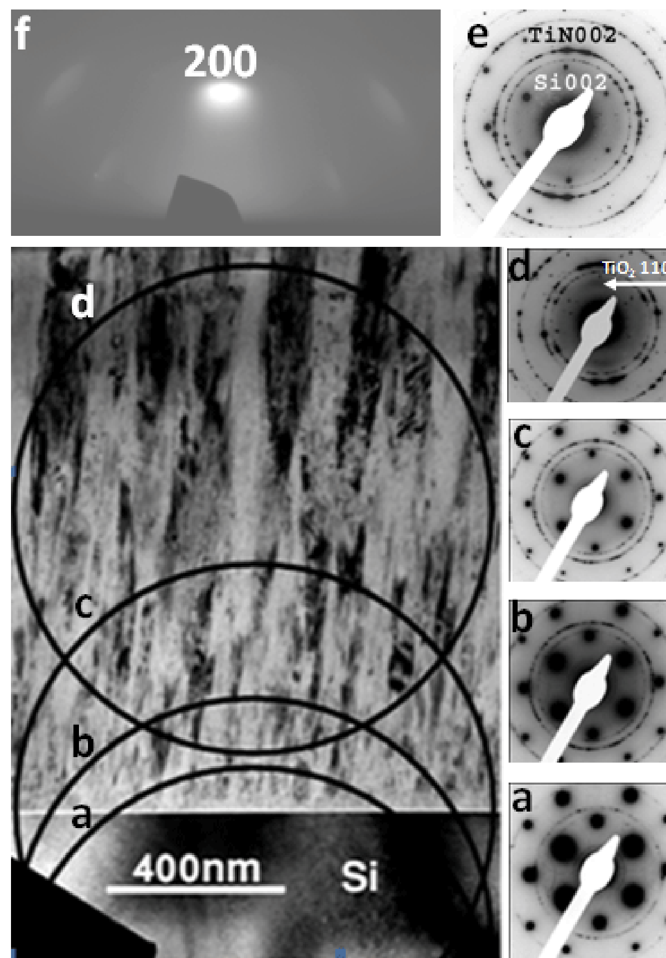

Figure 5.10. X-TEM image of the $Ti_{0.45}O_{0.20}N_{0.35}$ and selected area electron diffraction poatterns (SAED) taken on the thickness domains marked by circles. Inset f is the reflection high energy electron diffraction pattern taken on the surface of the as deposited film. The area of SAED pattern of inset e includes the substrate Si single crystal and the whole cross section of the film.

the surface of the film (Figure 5.10 inset f) shows that the film surface is composed only by <001> oriented crystals. SAED pattern (Figure 5.10 inset a) including the <100> single crystal Si substrate and the very thin thickness domain of the film at the substrate indicates that the small TiN crystals developed on the substrate are randomly oriented. The diffraction patterns taken successively from thicker domains of the film (Figure 5.10 insets c and d) clearly demonstrate that the <001> texture become stronger with the thickness. According to figure 5.10, inset d the upper part of the film is composed mainly from <001> oriented columns. The dark field image (DF) taken by the 002 reflection clearly demonstrates the V-shaped morphology of crystals growing with <001> orientation (e.g. the crystal marked by A in Figure 5.11). That is the characteristic structure of zone T of the structure zone models.

Figure 5.11 shows the bright field image (BF) and the dark field image (DF) of other part of the film. The BF image clearly demonstrates that the film is composed of V-shaped crystals of columnar morphology marked by A in Figure 5.11 a in addition, the <001> texture appears in the upper part of film as seen in SAED (igure 5.11a inset). The DF image taken by the 002 reflection demonstrates the V-shaped morphology of crystals growing with <001> orientation as seen in Figure 5.11 b.

It can be concluded that under our experimental conditions the structure of oxygen doped $Ti_{0.45}O_{0.20}N_{0.35}$ oxynitride film has columnar morphology with V-shaped crystals and the preferred orientation is <100>.

5.3.5. Precession electron diffraction analysis for oxygen doped $Ti_{0.45}O_{0.20}N_{0.35}$ oxynitride film.

Figure 5.12 shows the cross sectional images of the film taken by the precession electron diffraction (PED) and ASTAR technique. The crystals with <100> axis nearly parallel to the substrate surface normal are shown in red, the crystals with other orientation are represented by different colors. The pole figure of the <100> oriented silicon single crystal is shown in inset 1. The pole figure of inset 2 demonstrated the random orientation of crystals near to the substrate surface. In the insets from 3 to 6 one can see that the 001 texture becomes stronger with increasing

thickness. These results clearly visualize the improvement of the texture with thickness determined by successively taken SAED pattern.

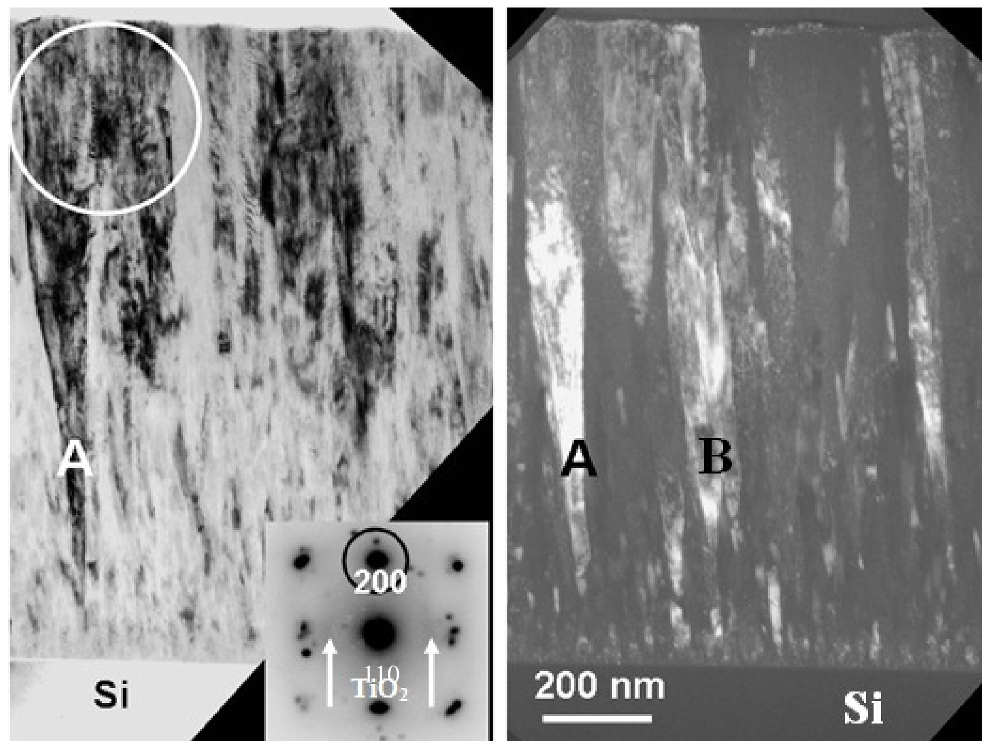

Figure 5.11. (a) The bright field image (BF), (b) the dark field image (DF) taken by the 002 reflection.

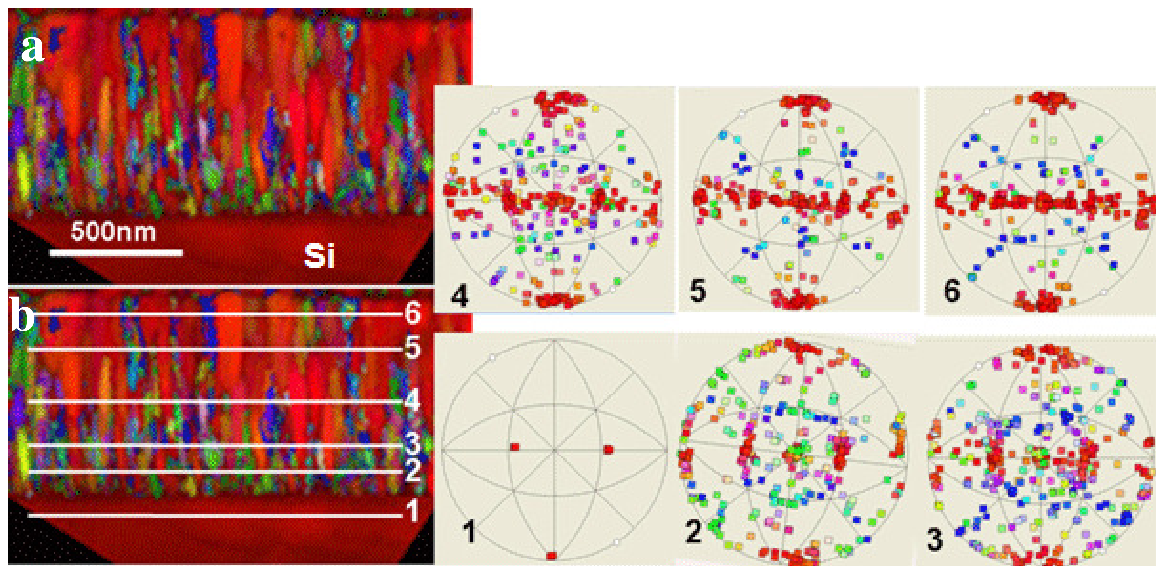

Figure 5.12. <100> pole figures taken along the thickness in oxygen doped $Ti_{0.45}O_{0.20}N_{0.35}$ oxynitride film

5.3.6. Nanoidentation measurements

Figure 5.13 shows typical load vs. displacement curves for $Ti_{0.45}O_{0.20}N_{0.35}$ oxynitride nanocomosite thin film coating at 10mN load. The maximum indentation depth was about 150 nm for the $Ti_{0.45}O_{0.20}N_{0.35}$ oxynitride thin film while in the undoped $Ti_{0.45}N_{0.51}O_{0.04}$ film prepared at the same parameters it was 175nm. The hardness and the Young's modulus of the $Ti_{0.45}O_{0.20}N_{0.35}$ oxynitride thin film are 28 GPa and 346 GPa respectively. While the undoped $Ti_{0.45}N_{0.51}O_{0.04}$ film prepared at the same parameters has a lower value, 18 GPa in agreement with the literature ***[Makino et al, 1998], [Wittling et al, 1995], [Barhai et al, 2010], [Patsalas et al, 2000].***

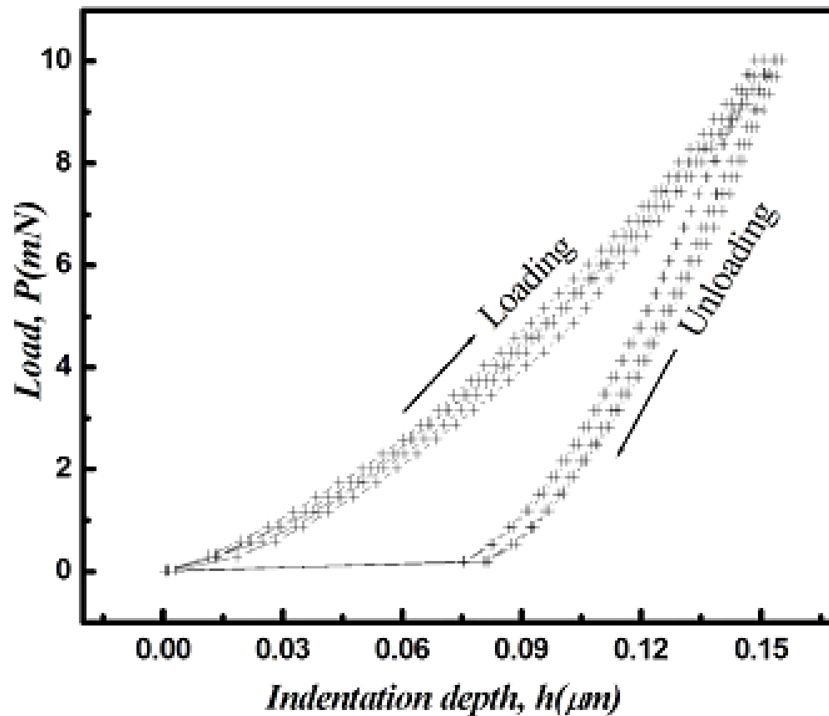

Figure 5.13. Typical load vs. displacement curves for $Ti_{0.45}O_{0.20}N_{0.35}$ oxynitride thin film at 10mN load.

5.4. Substructure in the columnar crystals of the $Ti_{0.45}O_{0.20}N_{0.35}$ oxynitride thin film

In the cross sectional transmission electron microscopy (X-TEM) images a substructure is showing up in form of fibre-like morphology parallel to the axis of the

columnar crystals and in a honeycomb-like supernetwork in the cross section of the single crystal columns in the plane view TEM specimens. The fibre-like substructure proceeds to the film surface and manifests itself in the morphology of the dome-shaped surface areas of the single crystal columns as revealed by atomic force microscopy analysis**.**

The cross sectional (XTEM) and plane view TEM images of the specimens representing the thickness range near to the surface of the film are shown are shown in Figures 5.14 and 5.15. According to figure 5.14a the film surface is quite smooth.

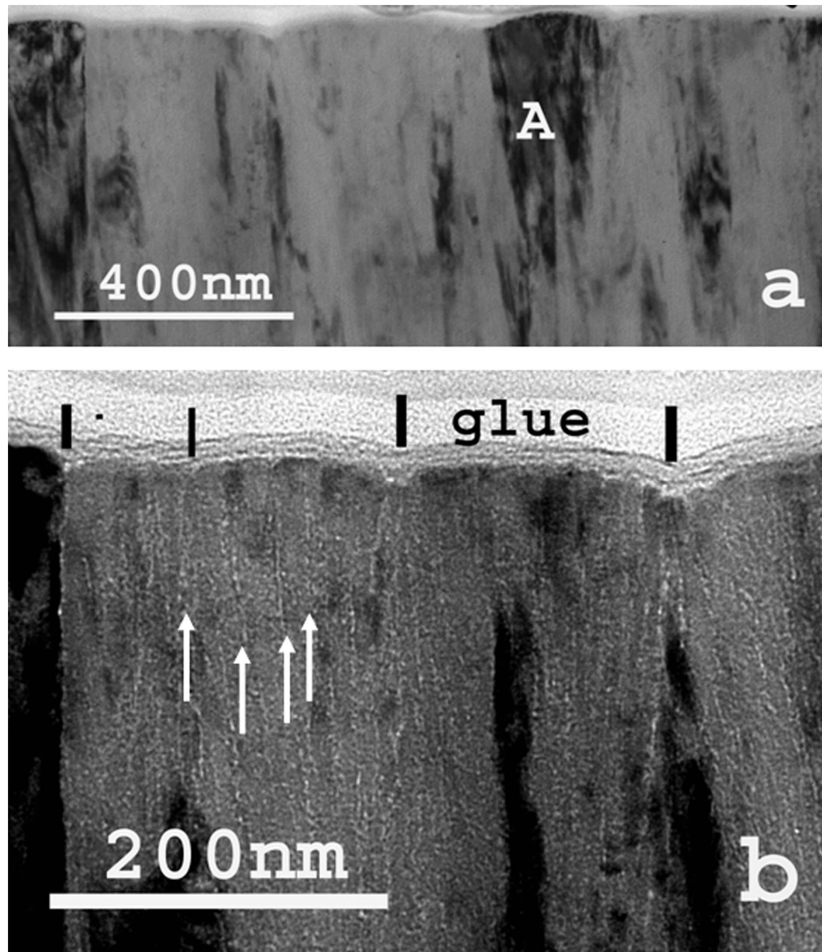

Figure 5.14. Cross sectional TEM images taken on the thickness range near to the surface of the $Ti_{0.45}O_{0.20}N_{0.35}$ oxynitride film: a) shows the shallow dome shaped surface morphology of the columns; the groves at the column boundaries are marked by slabs; b) the phase contrast image is visualising the fibre-like substructure in the bulk of columnar crystals; the boundaries between the fibres are marked by arrows ***[Hasaneen et al, 2012].***

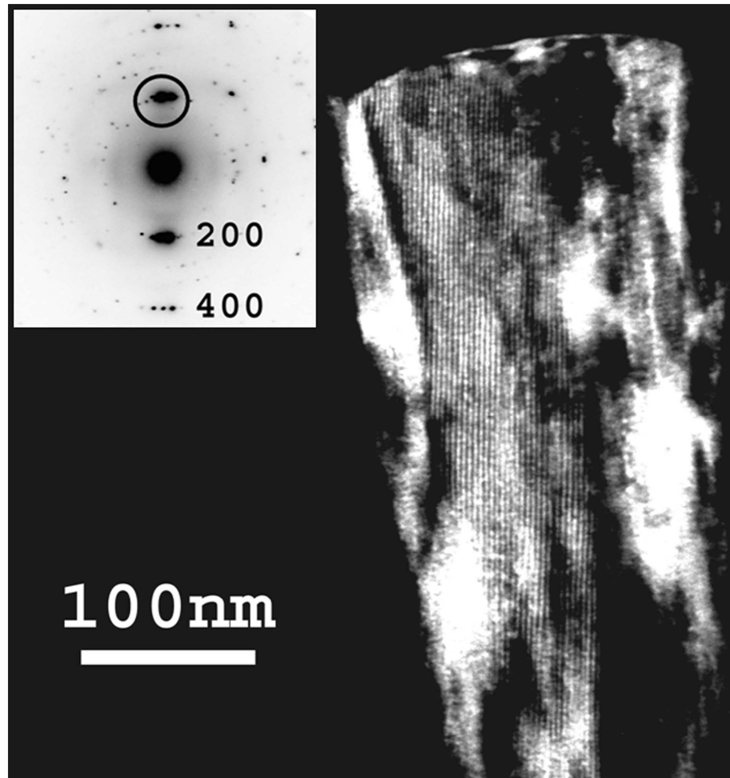

Figure 5.15. The Moiré pattern showing up on the dark field image (DF) of the crystal marked by A in figure 5.14a. demonstrates the high quality of the overlapping columnar crystals in the $Ti_{0.45}O_{0.20}N_{0.35}$ oxynitride film. The dome shaped surface morphology of the columnar crystal is also clearly shown. The DF image is taken by the 200 reflection ***[Hasaneen et al, 2012]*****.**

The low waviness is related to the shallow dome shaped surface morphology of the columns. The column boundaries are decorated by grooves marked by slabs in Figure 5.14a. The width of columns is between 10 and 150 nm. In the phase contrast image (Figure 5.14b) a pronounced fibre-like substructure with diameters of 10-20 nm can be identified in the bulk of the columnar single crystals. The fibres are parallel to the axis of the columnar crystals. The boundary of fibres marked by arrows, manifests themselves in well defined lines in the phase contrast image. The fibres proceed to the surface of the columns producing fine dome shaped morphology features. Figure 5.15 shows the selected area electron diffraction (SAED) pattern and the dark field (DF) TEM image of the crystal marked by A in figure 5.14a. The SAED pattern represents three crystals grown in the <100> directions with small deviations from the substrate

normal. The corresponding, very regular Moiré pattern in the DF image taken by the 200 reflection demonstrates the high quality of the overlapping columnar crystals ***[Hasaneen et al, 2012].***

In the phase contrast TEM image of the plane view specimen within the domains representing the cross sections of the columnar crystals (Figure 5.16a) the fibre-like substructure appears in form of a honeycomb-like supernetwork. The dark field image (Figure 5.16b) taken by the strong 002 reflection of the SAED pattern proves that this domain is a single crystal and the honeycomb-like supernetwork shown up in the phase contrast image is in the bulk of the single crystal ***[Hasaneen et al, 2012]***.

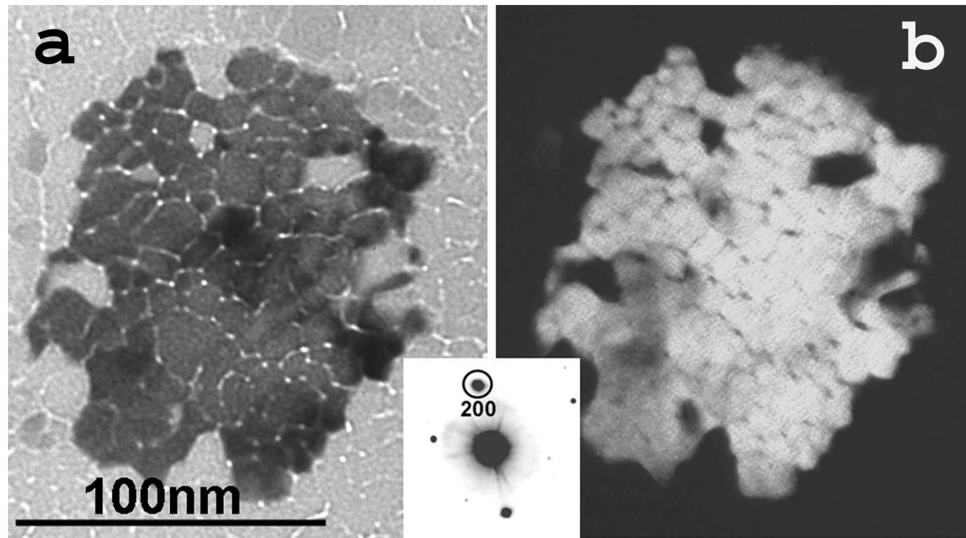

Figure 5.16 Phase contrast bright field (a) and dark field (b) TEM images of a column in the plane view specimen taken on the thickness range near to the surface of the $Ti_{0.45}O_{0.20}N_{0.35}$ oxynitride film show the substructure in the bulk of the single crystal column. DF image is take by the TiN 200 reflection ***[Hasaneen et al, 2012].***

The dome shaped morphology of the column surfaces and the fine, also dome-shaped morphology features within them related to the fibres can be well identified on the AFM image and line cut profile (Figure 5.17). The lateral sizes of the fine morphology features are in the range of 10-20 nm in accordance with the phase contrast X-TEM image (Figure 5.14b) and their height is in the range of 1-3 nm as

shown in the line cut profile (Figure 5.17c). Similar morphology features have been found in TiN_xO_y films prepared by hollow cathode reactive DC sputtering methods ***[Mehdi, et al, 2000].***

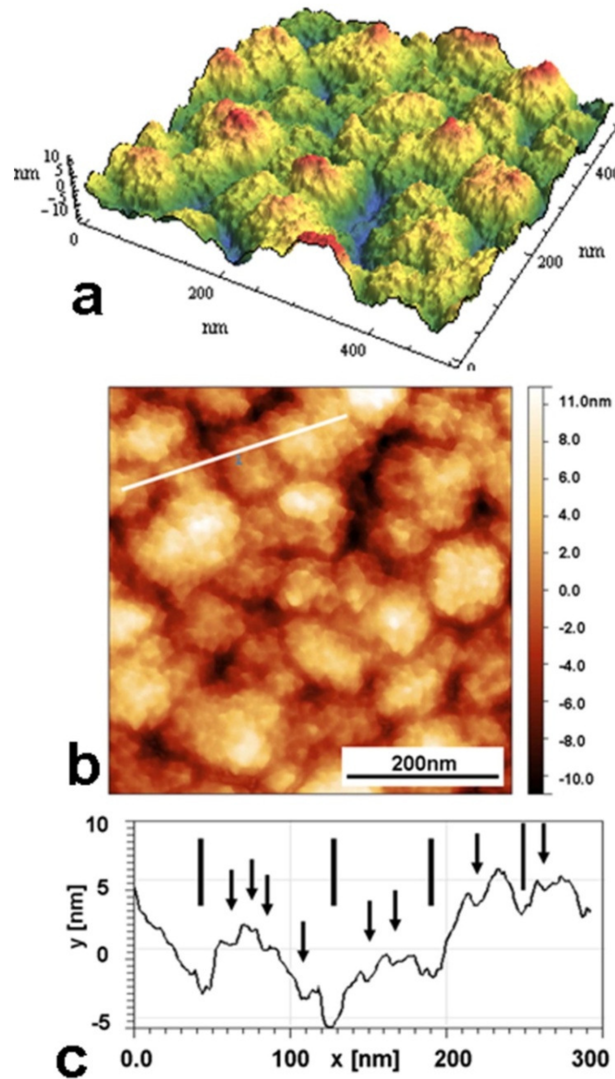

Figure 5.17. AFM images of the $Ti_{0.45}O_{0.20}N_{0.35}$ oxynitride film: a) topographic AFM image of the sample surface shows both the dome shaped surface morphology of columnar crystals and the fine morphology features within the surface area of columns; b) topographic AFM image shows the place of the height profile shown in c); slabs mark the column boundaries, while arrows the fiber boundaries ***[Hasaneen et al, 2012].***

5.5. Oxynitride film prepared at varying oxygen concentration (TO_11)

5.5.1. X-ray diffraction

Figure 5.18 shows θ-2θ X-ray diffractograms for oxynitride film prepared at varying oxygen concentration. From this figure we can conclude the coexistence of the 001 and 111 textures. The other reflections such as 220 and 311 are extremely weak. Furthermore the peaks are shifted to higher diffraction angles when compared with the JCPDS card: No.38-1420. The results from the analysis are presented in Table 5.IV

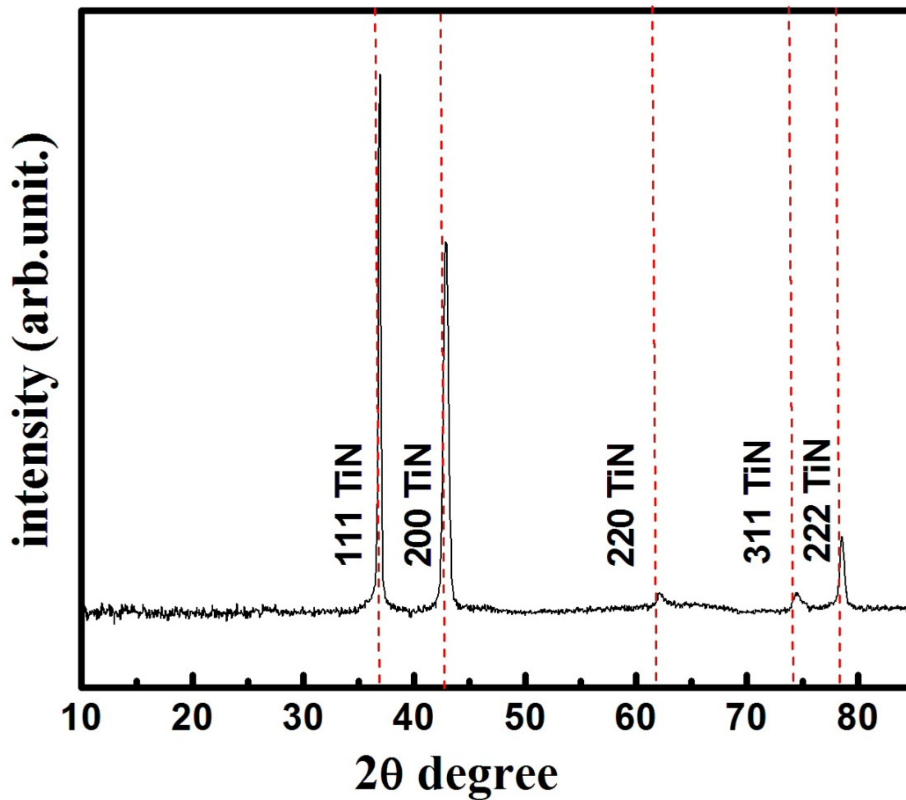

Figure 5.18. The θ-2θ XRD spectrum of the oxynitride film prepared at varying oxygen concentration.

Table 5.IV. Structure parameters calculated for oxynitride film prepared at varying oxygen concentration.

Peaks (hkl)	*2Θ*	*Lattice distance, d (A)*	*Lattice constant a (A)*	*FWHM*	*Grain size D(nm)*
111	*36.88*	*2.435*	*4.217*	*0.2753*	*5.3*
200	*42.87*	*2.107*	*4.214*	*0.5443*	*2.7*

5.5.2. Cross section transmission electron microscopy for oxynitride film prepared at varying oxygen concentration

Figure 5.19 shows the X-TEM microscopic image of the oxynitride film prepared at varying oxygen concentration with the SAED taken from the various domains along the thickness. Figure 5.19 inset (a) shows the SAED pattern of the 100 silicon single crystal substrate and the very thin thickness domain of the film at the substrate. The SAED pattern inset b demonstrates that in the thickness domains near to the substrate the <001> reflection intensified. The SAED pattern inset (c) taken from the central region of the film shows the coexistence of 001 and 111 textures. The SAED pattern inset d clearly shows that the upper part of the film is composed of large <111> oriented crystals. That proved by the reflection high energy diffraction pattern shown in inset e. the TEM image demonstrates also that both the 001 and 111 textures have V-shape morphology. That of <111> oriented crystals is more clearly shown in BF and DF images in Figure 5.20.

Figure 5.20 shows the <111> oriented crystals nucleated on the substrate and with the thickness increase the survived the competitive growth regime at high oxygen pressure promoting the growth <001> oriented crystals. When the oxygen pressure is decreased, the growth of <111> oriented crystals was promoted and these crystals were grown in V-shaped columns

It is clearly seen that, in the thickness domain near to the substrate the competitive crystal growth development with 001 texture, while at 11at.% oxygen concentration the competitive crystal growth development with 111 texture. In addition, both type of crystals exhibit V-shaped columns.

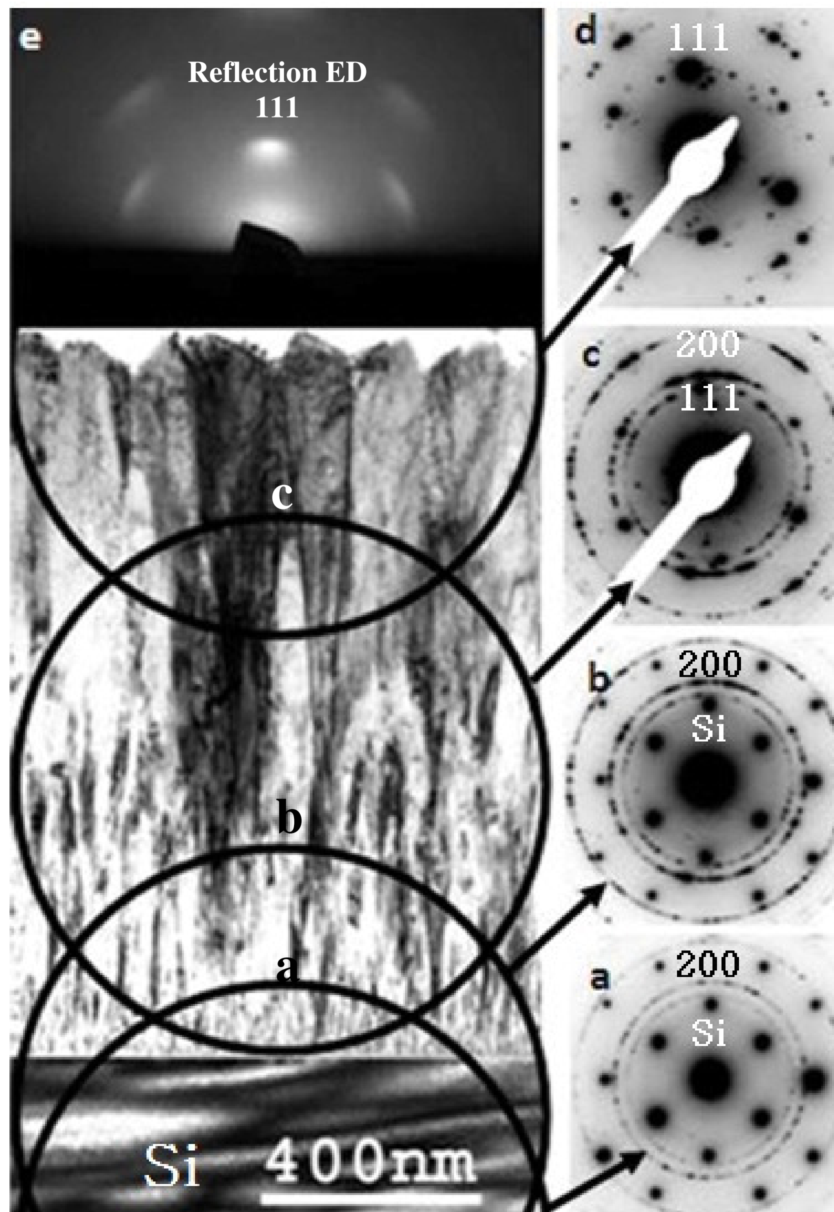

Figure 5.19. X-TEM image of the oxynitride film prepared at varying oxygen concentration and selected area electron diffraction patterns (SAED) taken on the thickness domains marked by circles. Inset e is the reflection high energy electron diffraction pattern taken on the surface of the as deposited film.

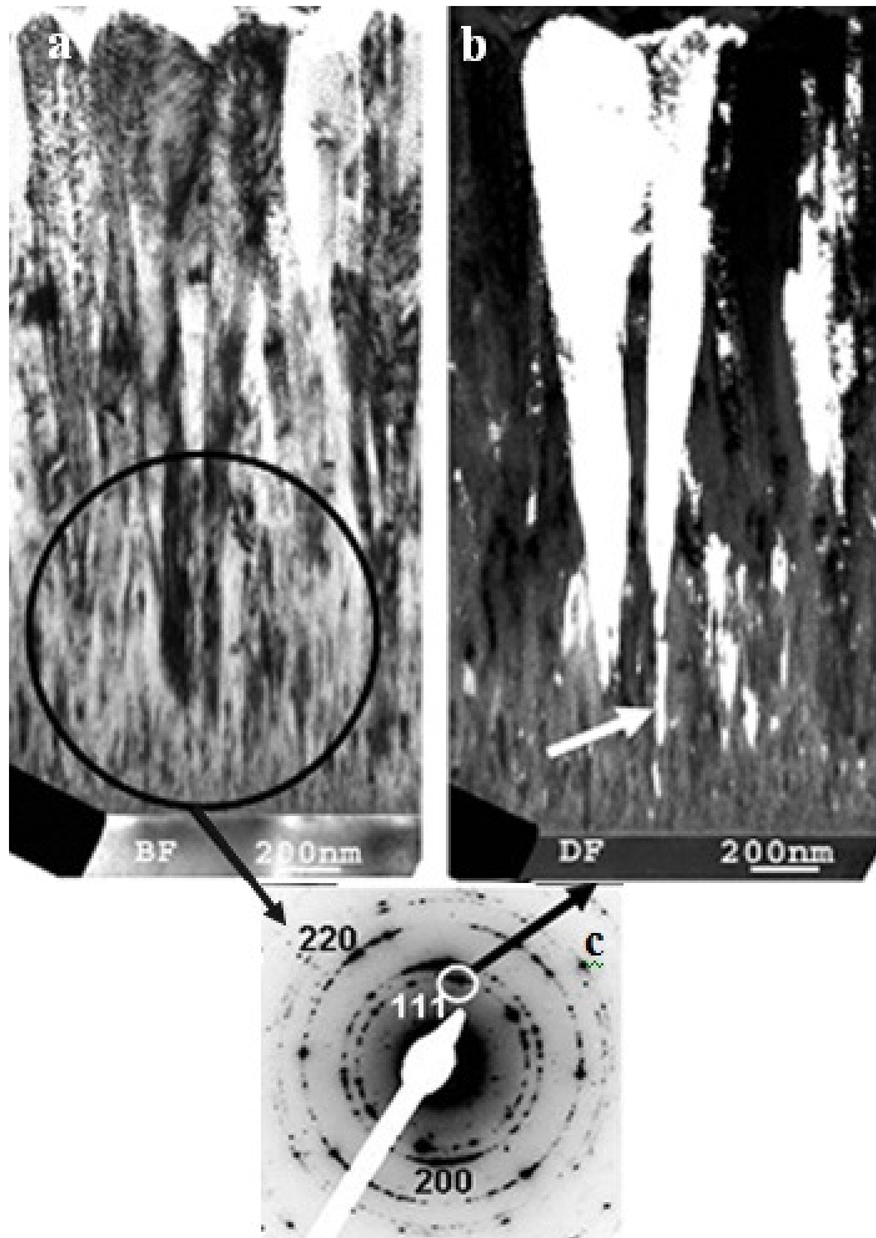

Figure 5.20. (a) The bright field image (b) the dark field image (DF) (c) and SEAD patterns of the oxynitride film prepared at varying oxygen concentration.

5.5.3. X-ray photoelectron spectroscopy (XPS) and Auger Electron Spectroscopy (AES) analysis

Figure 5.21 shows the AES depth profile of the O/Ti ratio. According to the AES measurements the N/Ti ratio in the film was 1.28. The film contained 20at.% oxygen concentration near to the substrate and 11at.% oxygen concentration in the upper part of film.

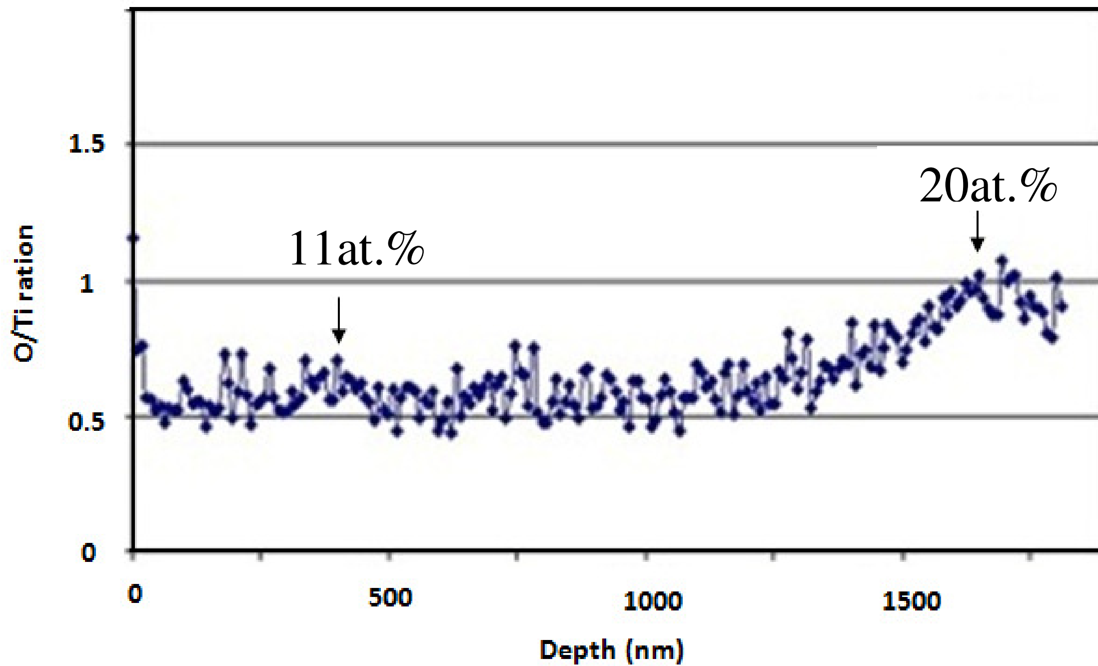

Figure 5.21. Auger electron spectroscopy (AES) depth profile of the oxynitride film prepared at varying oxygen concentration.

5.5.4. Precession electron diffraction analysis of Oxynitride film prepared at varying oxygen concentration.

Figure 5.22 shows the colored cross sectional image taken by the precession electron diffraction (PED) and ASTAR technique. The crystal with <100> orientation perpendicular to the substrate are shown in red while the <111> oriented onces in blue. At high oxygen concentration ≈ 20at.% the <001> oriented crystals are grown preferentially in V–shaped columns. While at low oxygen concentration ≈11at.% the <111> oriented crystals are grown preferentially in V-shaped columns (5.22 inset A).

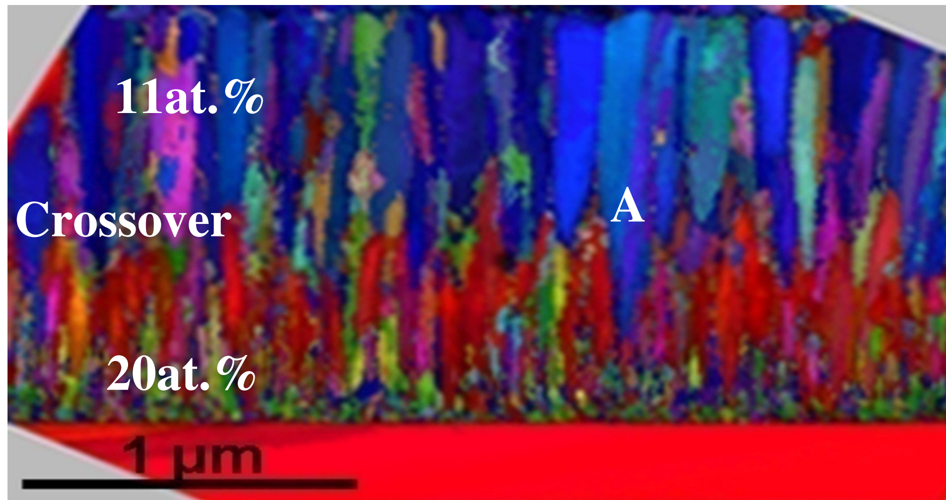

Figure 5.22. PED-ASTAR image for oxynitride film prepared at varying oxygen concentration: crystals with <001> in red, with <111> in blue.

5.5.5. Nanoidentation measurements

Figure 5.23 shows typical load vs. displacement curves for oxynitride film prepared at varying oxygen concentration at 10mN load. The maximum indentation depth was about 165nm while the undoped $Ti_{0.45}N_{0.51}O_{0.04}$ film prepared at the same parameters has 175nm. The hardness and the Young's modulus of the oxynitride film prepared at varying oxygen concentration is 18.2 GPa and 332 GPa respectively,

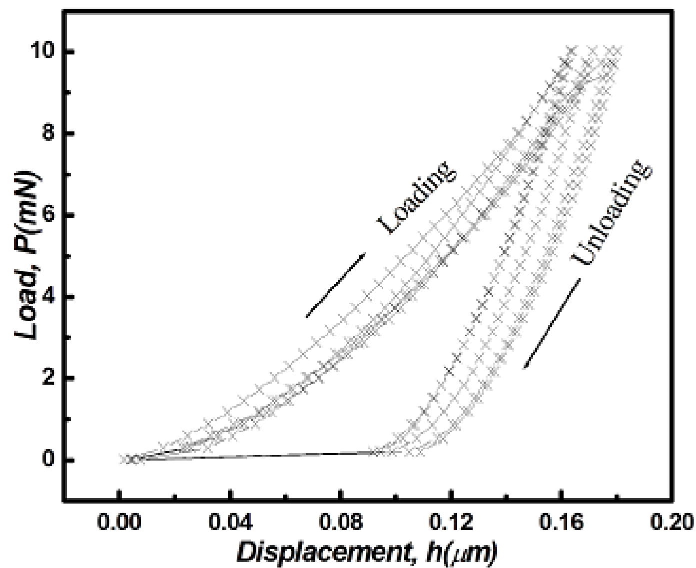

Figure 5.23. Typical load vs. displacement curves for Oxynitride film prepared at varying oxygen concentration at 10 mN load.

5.6. References

Bell T. J., Bendeli A., Field J. S., Swain M. V., and Thwaite E. G., The determination of surface plastic and elastic properties by ultra micro-indentation, Metrologia 28(1991)463-469.

Biro L. P., Márk G. I., Gyulai J. and Thiry P. A., STM and AFM investigation of carbon nanotubes, Materials Structure, 6(1999)104-108.

Briggs D. and Seah M. P., Auger and X-ray Photoelectron Spectroscopy, Practical Surface Analysis, Volume 1 (John Wiley and Sons, Chichester, UK, 1990).

Dirras G., Ouarem A., Couque H., Gubiza J., Szommer P. and Brinza O., Microstructure and nanohardness in a polycrystalline Zn deformed by high strain rate impact, Materials Characterization, 62(2011)480-487.

Guillot J., Fabreguette F., Imhoff L., Heintz O., Marco de Lucas M. C., Sacilotti M., Domenichini B. and Bourgeois S., Amorphous TiO_2 in LP-OMCVD TiN_xO_y thin films revealed by XPS, Applied Surface Science, 177(2001)268–272.

Jakab-Farkas L., Papp S. and Biró D., Effect of N concentration on microstructure Evolution of the nanostructured (Al, Ti, Si)N coatings prepared by d.c. reactive magnetron sputtering, scientific bulletin of the Petru Maior university of Tirgu Mures Vol. 6 (XXIII) (2009)ISSN 1841-9267.

Lábár J. L., Consistent indexing of a (set of) SAED pattern(s) with the ProcessDiffraction program, Ultramicrosc 103 (2005) 237-249.

Latellaa B. A., Ganb B. K., Daviesb K. E., McKenzieb D. R. and McCulloch D. G., Titanium nitride/vanadium nitride alloy coatings: mechanical properties and adhesion, Surface and Coating Technology, 200 (2006)3605–3611.

Ma L. W., Cairney J. M., Hoffman M., and Munroe P. R., Deformation mechanisms operating during nanoindentation of TiN coatings on steel substrates", Surface and Coating Technology, 192(2005)11-18.

Makino Y., Nose M., Tanaka T., Misawa M., Tanimoto A., Nakai T., Kato K., and Nogi K., Characterization of $Ti(N_xO_y)$ coatings produced by the arc ion plating method, Surface and Coating Technology, 98(1998)934-938.

Hasaneen M. F., Biro D., Székely L, Nemes-Incze P., Barna P. B., Substructure in the columnar crystals of the Ti0.45O0.20N0.35 oxynitride thin film, Vacuum, 86, (2012) 2105-2108.

Mehdi K. H., Alexander A. B. and Nobuhiko F., Formation of thin TiN_xO_y films by using a hollow cathode reactive DC sputtering system, Thin Solid Films, 372(2000)70-77.

Wittling M., Bendavid A., Martin P.J., Swain M.V., Influence of thickness and substrate on the hardness and deformation of TiN films, Thin Solid Films 270 (1995) 283-288.

Barhai P.K., Kumari Neelam., Banerjee I., Pabi S.K., Mahapatra S.K., Study of the effect of plasma current density on the formation of titanium nitride and titanium oxynitride thin films prepared by reactive DC magnetron sputtering, Vacuum 84 (2010) 896–901.

Patsalas P., Charitidis C., Logothetidis S., The effect of substrate temperature and biasing on the mechanical properties and structure of sputtered titanium nitride thin films, Surface and Coatings Technology 125 (2000) 335–340.

Chapter 6

Discussion

In this discussion we will point to the fundamental questions of the texture evolution in oxygen doped titanium nitride (TiN) films deposited at the same substrate temperature (400^0C, T_s/T_m= 0.21). In TiN films prepared by physical vapor deposition (PVD) at substrate temperatures 0.2 < T_s/T_m< 0.3 (Zone T) the <111> preferred orientation (PO) is the most commonly observed orientation of growth ***[Sundgren, 1985], [Oh and Je, 1993],*** however <001> and <220> PO have also been reported by changing the deposition parameters such as bias voltage ***[Kobayashi and Doi, 1978],*** N/Ti ion ratio ***[Jeong et al, 1991]***, the ratio of N^+/N_2^+***[Gall et al, 2003]*** and the oxygen doping ***[Makino et al, 1998]***.

Most explanations on the development of the PO in thin films were determined by the interplay of thermodynamic and kinetic driving forces, considering the surface energies and ad-atom mobilities and interactions ***[Petrov et al, 2003], [Veprek, 1985], [Gall et al, 2003]***, ***[Mahieu and Depla, 2009]***, ***[Makino et al, 1998]***, ***[Castaldi et al, 2008]***. These strongly depend on the deposition temperature and on the Miller indices of the growing crystal faces as well. In case of substrate temperature used in our experiments (T_s/T_m= 0.21) the kinetics operates preferentially, because the bulk diffusivity of the atoms is very limited. In that case the development of PO is controlled by the difference in the growth rates of the crystal faces with different Miller indices both in elemental and strictly monophase systems as discussed in details by ***[Barna and Adamik, 1998]*** and ***[Petrov et al, 2003]***. In case of TiN films the dependence of surface atomic processes and interactions controlling the growth rates of the various crystal faces on the deposition parameters was analyzed in details by ***[Gall et al, 2003]***. They used *ab initio* calculations to determine the atomistic processes on the {111} and {001} TiN crystal faces in dependence of the parameters. They have concluded that in case of excess N the formation of 111 texture is promoted when Ti and N_2 species are present, while if mostly atomic nitrogen species are impinging, the 001 texture develops. That was confirmed by ***[Mahieu and Depla, 2009].***

Presence of impurities such as oxygen and carbon, which were found in all deposits also influences both the internal stress and texture evolution of thin films ***[Ehiasarian et al, 2011]***. Oxygen is generally present in the whole thickness of the films. This indicates that it is incorporated during the film growth from the environment. The co-deposition of oxygen during the growth of the film might modify the pathway of structure evaluation.

We can conclude that most of the literature discussed the texture change from 111 to 001 in general, but neither the structure nor the possible pathways of structure evolution have been analyzed in details. In this chapter we try to answer the following questions:

1. In which state (phase) is the oxygen incorporated in to the film with 001 texture?
2. What is the characteristics of the microstructure of the <001> oriented film making possible to select between the mechanisms of texture evolution?
3. What are the specific structural characteristics of the <001> oriented film which could be used at considering the growth mechanism?
4. What is the real structure of the film deposited at varied oxygen concentration having a crossover between the 001 and 111 textures?

To answer these questions we will evaluate and discuss our experimental results which are included in chapter 5.

First of all we can conclude that the present results clearly approve that the change of 111 texture to 001 in the TiN film is related to the effect of oxygen. It is because the TiN film deposited at the same deposition parameters without oxygen doping was grown with 111 texture.

6.1. In which states (phases) is the oxygen incorporated in to the film with 001 texture?

According to Auger depth profile analysis (Figure 5.7) the concentration of oxygen is the same along the thickness of the film. The detailed analysis of the Ti peak in the XPS Spectrum (Figure 5.8 and Table 5.III) clearly demonstrates that

beside TiN both TiN_xO_y solid solution and TiO_2 phases are present in the film. Existence of the TiO_2 phase is approved also by SAED investigation. According to these results it is in nanocrystals which are in orientation relation to the <001> oriented TiN crystals ***[Biró et al, 2011], [Biró et al, in preparation].*** The formation of TiO_2 phase indicates that during the structure evolution of the film one part of the oxygen had to be segregated. An interesting question is in which form this phase is present and where is situated in the film. That is discovered by the detailed structure analysis of the upper part of the film which is composed of <001> oriented crystals.

6.2. What is the characteristics of the microstructure of the <001> oriented film making possible to select between the mechanisms of texture evolution?

In Figure 6.1 XRD diffraction patterns of the TiN films with different oxygen contents are shown and compared with the values given in card JCPDS 38-1420. Figure 6.1b related to film with 20at.% oxygen contains a high and sharp 002 reflection. The 111, 220 and 311 reflections are showing up with very low intensity ***[Hasaneen et al, 2012] [Biró et al, in preparation].***

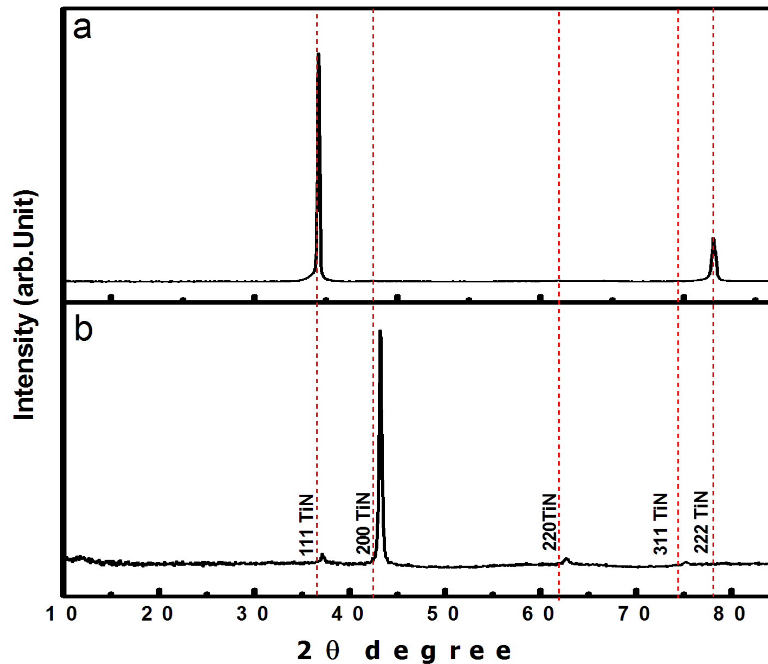

Figure 6.1: XRD patterns of the TiN films with different oxygen contents at 4at.% and 20at.% compare with original value coming from JCPDS card: No.38-1420.

These indicate that beside crystals with <001> orientation randomly oriented crystals are also present. Figure 6.1a shows the diffraction pattern of TiN film with 4at.% oxygen. Here the strong 111 is clearly shown together with weak 200, 220 and 311 reflections. The broadening of the diffraction peaks with increasing oxygen content, and consequently, the decrease of the mean grain size (size of coherent scattering domains) is clearly shown and summarized in Table 5.I and 5.II. It can be also noticed that, the diffraction peaks are shifted towards higher angels as a function of increasing oxygen content. This means that, oxygen atoms with a smaller radius substitute nitrogen atoms ***[Shannon, 1976], [Jin and Maruno, 1991], [Makino et al, 1998]*** and form the solid solution phase shown also by XPS. In the TiN_xO_y oxynitride solid solution the lattice parameters calculated by the Vegard's low (considering the lattice values given for TiN in JCPDS card No 38-1420 a = 4.24A and for TiO JCPDS card No 08- 0117 a = 4.177A) and the values determined from the present XRD patterns are compared in Figure 6.2. The interpretation of the negative deviation of lattice parameter from Vegard's line in case of 20at.% oxygen needs further analysis, namely because the presence of segregated TiO_2 phase, to be discussed in 6.3, would result in positive deviation ***[Castaldi et al, 2008].***

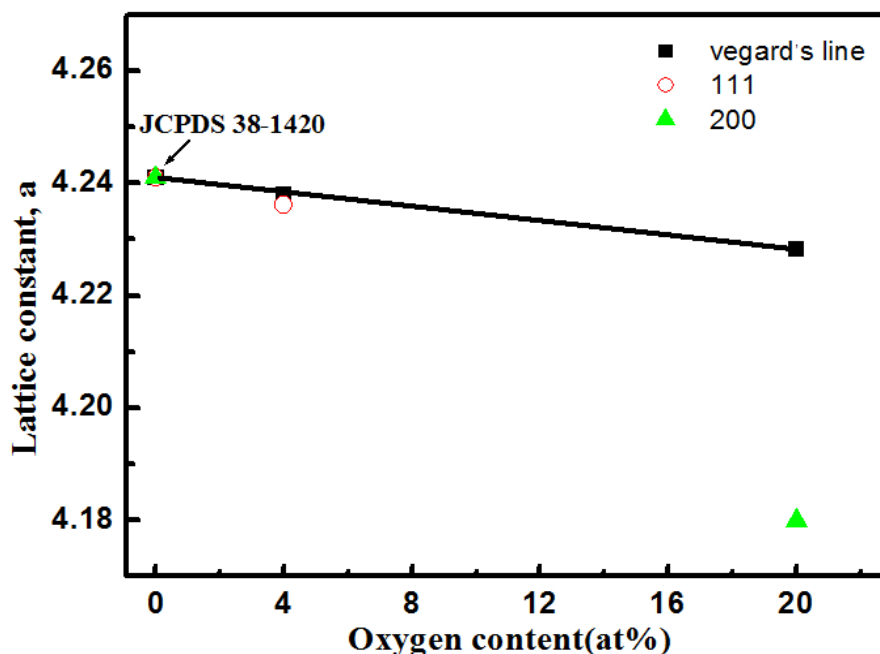

Figure 6.2. Deviation of lattice constant for 111 and 200 peaks from Vegard's law with different oxygen contents at 4at.% and 20at.% compared with original value coming from JCPDS card: No.38-1420.

Figure 6.3 depicts the texture coefficient (T_C) of the 111 and 001 textures as a function of oxygen content. The presence of the weak 220 and 311 reflections indicate that crystals also with random orientation are present in both films. The detailed analysis of the cross sectional specimens by SAED (Figures 5.3 inset a and 5.10 inset a) and analysis carried out by PED ASTAR technique (Figure 5.12 inset 2) revealed that the random oriented crystals are developed on the substrate surface in both films. SAED analysis of the cross sectional specimen (Figure 5.10) and by the thickness section of the cross section image taken by the PED ASTAR technique of the film with 20at.% oxygen clearly show that the 001 texture is developed stepwise. High energy electron diffraction clearly proved that the surface of the film is composed completely by <001> oriented crystals. On the other hand the bright field and dark field images (Figure 5.11) demonstrate that the <001> oriented crystals are present in V-shaped columns. These results approve that the structure evolution is governed by the competitive growth of crystal and the preferential growth direction is controlled by the kind of participation of oxygen species in the surface atomic processes.

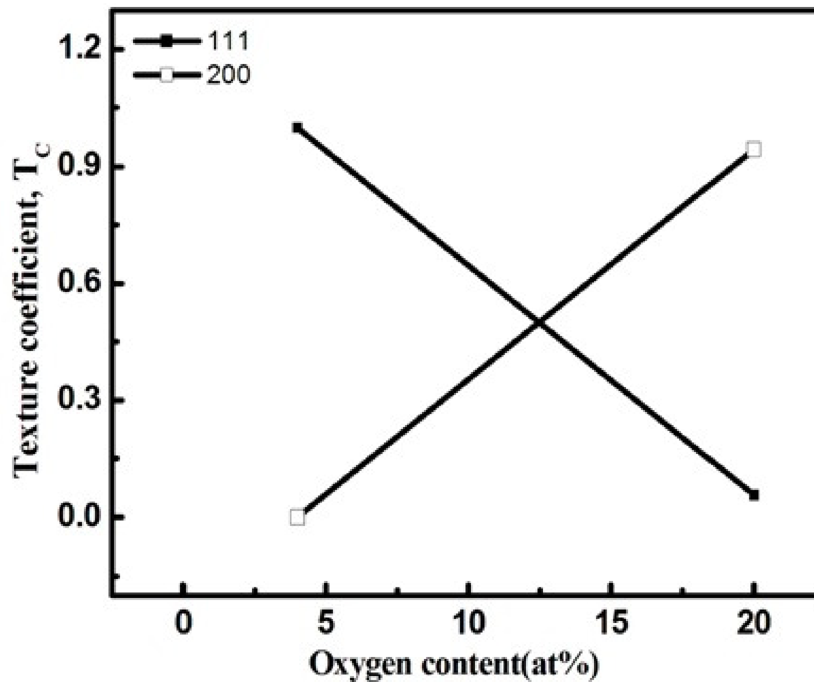

Figure 6.3. Texture coefficients as a function of the oxygen contents.

6.3. What are the specific structural characteristics of the <001> oriented film which could be used at considering the possible growth mechanisms?

The detailed analysis of the bulk structure and surface morphology of the single crystal columns grown in the upper part of the film presented more information on the distribution and morphology of TiO_2 phase ***[Hasaneen et al, 2012].*** The phase contrast TEM image indicates that the TiO_2 as a lower density phase is distributed in fine fibers within the bulk of the single crystals (Figure 5.15 and 6.4) and at the boundaries of single crystal columns. TiO_2 fibers are proceeding to the surface of the crystals and related to dents in the surface morphology. This dents show up in a fine submorpology within the cup-shaped surface area of the columns. This is clearly demonstrated in AFM images shown in Figure 5.17.

Bright field and dark field analysis of the plane view specimen containing the cross section of the columns discovered that the fibers of TiO_2 phase are arranged in a honeycomb-like structure. The fibers showing up in these images as spots of about 0.5-1 nm diameter seem to be connected by very narrow layers also with bright contrast.

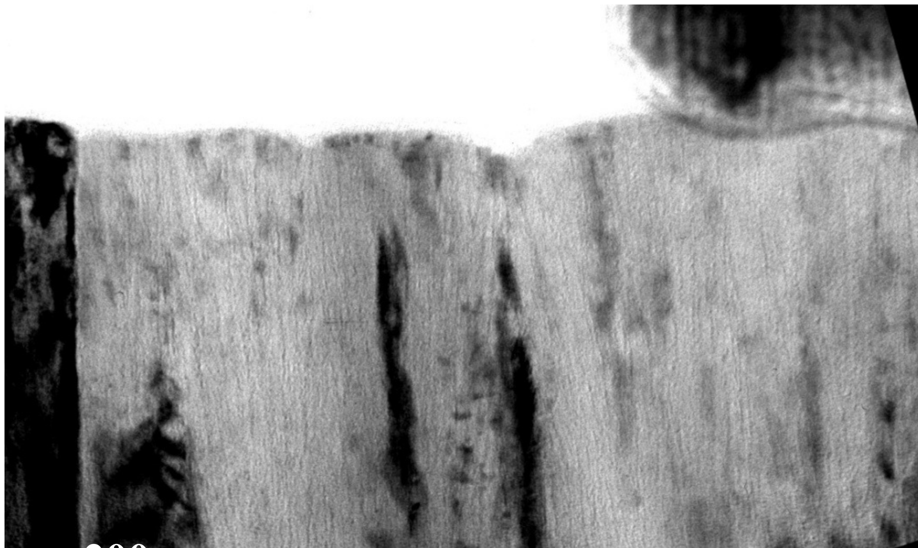

Figure 6.4. Cross sectional over focuses X-TEM image taken on the thickness range near to the surface of the oxygen doped $Ti_{0.45}O_{0.20}N_{0.35}$ oxynitride film.

By summarizing the results discussed in 6.1-6.3 one can make the following conclusions. The present results clearly demonstrated that at high level of oxygen doping the 001 texture in the cubic TiN films is developing by competitive growth of crystals and the competition is governed by the faster growth of crystals with <001> orientation. By this way I confirmed and experimentally approved that the competitive growth model which was proposed by ***[Ehiasarian et al, 2011]*** in case of very specific deposition process can be used for describing the structure evolution of oxygen doped films. In their experiment they only started the deposition at high level of oxygen contamination but continued at a very low oxygen concentration. In the present experiments thicker films have been deposited at the same doping level, and by this way all three growth regimes of competitive growth (nucleation of random oriented crystals, competitive growth of crystal and oriented growth of crystals) have been developed. By this way in our film it was possible to study the structure developing at the continuous growth of 001 oriented crystal which contained all structural features which could make possible to reconstruct the elementary atomic processes of self organizing structure evolution. That would not be possible in the case of films prepared by ***[Ehiasarian et al, 2011]***. My results demonstrated that the oxygen species incorporating into the film are not dissolved completely in the TiN lattice, but some part of them is segregated and form a TiO_2 phase. The SAED patterns indicated that this phase is nanocrystalline and orientationally related to the TiN crystals. The formation of TiO_2 phase resulted in the development of a substructure in the bulk of TiN crystalline columns ***[Hasaneen et al, 2012].*** Consequently the growth of these films has to be considered as the growth of a two phase system and the nucleation and simultaneous growth of phases has to be studied in more details to be able to develop the pathway of structure evolution.

6.4. What is the real structure of the film deposited at varied oxygen concentration having a crossover between the 001 and 111 textures?

The θ-2θ XRD diffractogram clearly demonstrated that the film deposited at first at high (20at.%) and latter at lower (11at.%) oxygen concentration is composed of crystals with both <001> and <111> orientations (Figure 5.18). I have shown by detailed TEM and SAED analysis (Figure 5.19 and 5.22) that crystals with these orientations are situated in tow thickness domains and these domains correlate to the

concentration level of oxygen (Figure 5.21). ***[Biró et al in preparation].*** The thickness domain near to the substrate is with 001 texture and contains 20at.% oxygen, the second thickness domain, beyond of that, is with 111 texture and contains 11at.% of oxygen. Both domains are composed of V-shaped crystals well shown in the coloured image of Figure 5.22 (red coloured are the <001>, blue coloured the <111> oriented crystals). Between the two textures there is a thickness domain in which both texture coexist but the <001> oriented red coloured crystals are with V-shaped morphology down while the <111> oriented crystals (blue coloured ones) are V-shaped upwards. This thickness domain is the crossover between the two textures.

Crystals with V-shaped upwards are the faster growing crystals developing the competitive growth textures. The red crystals with V-shaped upwards are characterized the first thickness domains indicating that in the presence of high oxygen concentration the 001 texture was developing as discussed in 6.4. From the crossover the <111> crystals have the V-shape upwards indicating that from this growth stage they are growing faster. That means they are over growing the <001> crystals which are growing from this stage in V-shape downwards.

The key issue was to discover where are originating the <111> oriented crystals starting to grow in columns with V-shaped upwards from the crossover? I have clearly shown (Fig. 5.20). Here is clearly shown that the <111> oriented crystals showing up in the dark field image nucleated on the substrate surface and are grown in a narrow column surviving the growth competition dominated by the <001> crystal. So, the question above can be answered as follows:

- The <111> oriented crystals composing the thickness domain with 111 texture are nucleated on the substrate.
- These urvived the competitive growth regime at high oxygen pressure dominated by preferential growth of <001> oriented crystals.
- When the oxygen pressure is decreased, the growth of <111> oriented crystals became promoted and these crystals were grown in V-shaped columns

By considering these results I suggested that a crossover between the 001 and 111 textures can be formed when the development of the 001 texture is not completed when the oxygen concentration is decreased to a value at which the growth of <111>

oriented crystals is preffered. In other words that means that the oxygen concentration has been decreased during the deposition at the film thickness at which the surface of the growing film contained also columns terminated with {111} crystal faces. These <111> oriented crystals will grow faster and dominate the new competitive growth regim due to the lower oxygen concentration.

In the light of this image we can interpret the results of ***[Ehiasarian et al, 2011]*** on films deposited at 30A peak current (Figures 17,18 and Table II). According to the depth analysis, the deposition of the film started also at rather high oxygen concentration (near to 20at.%) because of the not enough degassing of the deposition system. The coexistences of the 111 and 001 textures at the surface thickness domains (plane view specimen C shown in Figure 17) is quantitatively demonstrated by the evolution of the SAED pattern (Table II). In that case the thickness of the film during the growth arrived only the thickness domain of the crossover.

6.5. References

Barna P. B. and Adamik M., Fundamental structure forming phenomena of polycrystalline films and the structure zone models, Thin Solid Films, 317(1998)27-33.

Biró D., Hasaneen M. F., Székely L., Menyhárd M., Gurbán S., Pekker P., Dódony I., and Barna P. B., Effect of oxygen doping on the evolution of 001 texture and the crossover between 001 and 111 textures in TiN films, Yearbook 2011 for Research Institute for Technical Physics and Materials Science-Hungarian Academy of Sciences.

Biró D., Hasaneen M. F., Székely L., Menyhárd M., Gurbán S., Pekker P., Dódony I., and Barna P. B., Evolution of the 001 texture in $Ti_{0.45}O_{0.20}N_{0.35}$ oxynitride thin film, , in preparation.

Biró D., Hasaneen M. F., Székely L., Menyhárd M., Gurbán S., Pekker P., Dódony I., and Barna P. B., Development of the crossover between 001 and 111 textures in TiN films due to the variation of oxygen concentration , in preparation.

Castaldi L., Kurapov D., Reiter A., Shklover V., Schwaller P. and Patscheider J., Effect of the oxygen content on the structure, morphology and oxidation resistance of Cr–O–N coatings**,** Surface and Coatings Technology, 203 (2008) 545–549**.**

Ehiasarian A. P., Vetushka A., Aranda Gonzalvo Y., Sáfrán G., Székely L. and Barna P. B., Influence of high power impulse magnetron sputtering plasma ionization on the microstructure of TiN thin films, Journal of Applied Physics, 109(2011) 104314.

Gall D., Kodambaka S., Wall M. A., Petrov I., Greene J. E., Pathways of atomistic processes on TiN(001) and (111) surfaces during film growth: an *ab initio* study, Journal of Applied Physics, 93 (11)(2003) 9086.

Hasaneen M.F., Biro D., Székely L., Nemes-Incze P. and Barna P.B., Substructure in the columnar crystals of the $Ti_{0.45}O_{0.20}N_{0.35}$ Oxynitride thin film Vacuum, 86 (2012)2105-2108.

Jeong J. I., Hong J. H., Kang J. S. , Shin H. J., and Lee Y. P., Analysis of TiC and TiN films prepared by an arc-induced ion plating, Journal of Vacuum Science and Technology A: Vacuum, Surfaces, and Films, 9(1991) 2618 – 2622.

Jin P. and Maruno S., Stress relaxation in reactively sputter deposited TiO_xN_y Films, Japan Journal of Applied Physics, 30 (1991) 2058.

Kobayashi M. and Doi Y., TiN and TiC coating on cemented carbides by ion plating, Thin Solid Films, 54(1978)67-74.

Mahieu S. and Depla D., Reactive sputter deposition of TiN layers: modelling the growth by characterization of particle fluxes towards the substrate, Journal of Physics D: Applied Physics, 42 (2009) 053002.

Makino Y., Nose M., Tanaka T., Misawa M., Tanimoto A., Nakai T., Kato K. and Nogi *K.*, Characterization of Ti(N*x*O*y*) coatings produced by the arc ion plating method, Surface Coatings and Technology, 98 (1998) 934–938.

Oh U. C. and Je J. H., Effects of strain energy on the preferred orientation of TiN thin films, Journal of Applied Physics, 74(1993)1692.

Petrov I., Barn P. B., Hultman L. Greene J. E., Microstructure evolution during film growth, Journal of Vacuum Science and Technology A: Vacuum, Surfaces and Films, 21(2003)117-S128.

Shannon R. D., Revised effective ionic radii and systematic studies of interatomic distances in halides and chalcogenides, acta crystallographica Section A Crystal Physics, Diffraction, Theoretical and General Crystallography, 32 (1976) 751-767.

Sundgren J. E., Structure and properties of TiN coatings, Thin Solid Films, 128 *(*1985*)* 21–44.

Veprek S., Plasma-induced and plasma-assisted chemical vapour deposition, Thin Solid Films, 130(1985)135-154.

Chapter 7

Conclusion and new scientific results

7.1. Summary of the results

The pure and doped TiN coatings are widely used in industrial applications due to their superior physical and chemical properties. Oxygen is used as doping element to improve the properties by developing oxinitride structures. However, oxygen could be also co-deposited as non controlled and non expected contamination during the preparation of the films resulting in the development of peculiar structures unusual in pure TiN films. The most surprising and not yet understood structural peculiarity is the crossover between a first developing 001 and the later appearing 111 textures. At the preparation of oxynitride films it has been found that at oxygen concentrations beyond 15at.% the formation of 001 textures is promoted, however, the formation mechanisms of this structure were not studied in details.

In the present study the effect of the oxygen doping on the structure evolution of TiN films deposited by unbalanced magnetron sputtering on oxidized Si wafers was investigated. The sputter parameters used in the present experiments promoted the formation of 111 texture and V-shaped columnar morphology in undoped TiN films. The films were prepared at 400^0C substrate temperature and $3x10^{-1}$Pa argon-nitrogen atmosphere. The microstructure was investigated by θ-2θ XRD, transmission electron microscopy (TEM) and selected area electron diffraction (SAED), the chemical composition by EDS and XPS applying also depth profiling. The development of the V-shaped columnar morphology and textures developing by competitive crystal growth was demonstrated at first by PED-ASTAR technique in the TEM.

The main results of this work can be summarized as follows:

- Under our experimental conditions the structure of TiN thin film with low oxygen contamination (4at.%) has columnar morphology with V-shaped and the preferred orientation is 111 (zone T structure). The detailed TEM – SAED analysis of the cross sectional specimens revealed the three regimes and the

pathway of structure evolution characterizing the competitive crystal growth mechanism: (i) formation of randomly orientated crystal by nucleation on the substrate, (ii) the competitive growth regime: competitive growth of randomly oriented crystals dominated by the faster growth of <111> oriented crystals developing the 111 texture, (iii) the oriented growth regime: side-by-side growth of <111> oriented crystal columns.

- Under our experimental conditions the structure of oxygen doped $Ti_{0.45}O_{0.20}N_{0.35}$ oxinitride thin film has columnar morphology with V-shaped crystals and the preferred orientation is <001> along the thickness (zone T structure). It is clearly demonstrated at first by detailed TEM-SAED analysis of the cross sectional specimens applying also the PED-ASTAR techiqu**e.** This structure is characterized by (i) V-shaped columnar morphology, (ii) fibre texture with <001> crystal axis parallel to the substrate surface norma**l.** The pathway of structure evolution includes also the three growth regimes: (i) the film growth starts by the nucleation of random oriented crystals, (ii) the thickness growth of the continuous film is controlled by competitive crystal growth, in which the growth of <001> oriented crystals is preferred, (iii) oriented growth regime: side-by-side growth of <001> oriented crystal columns.
- The Auger electron spectroscopy (AES) depth profile analysis show the ratio of O/Ti peaks is constant along the thickness**.** The X-ray photoelectron spectroscopy (XPS) analysis shows that one part of the oxygen is segregated and incorporated into the bulk of TiN single crystalline columns forming crystalline TiO_2 phas**e**
- In the upper part of the $Ti_{0.45}O_{0.2}0N_{0.35}$ oxynitride thin film the columnar single crystals have a well developed fiber substructure in their bulk. The fibers are parallel to the axis of the columnar crystals. The fiber structure manifests itself in a honey-comb like supernetwork in the cross section of the columnar crystals as observed in the plane-view TEM specimens. Correlation has been found between the coexisting bulk columnar and fiber like structures and the surface morphology features. The 30-150 nm sized dome shaped surface morphology features correlate to the columns, while the 10-30 nm sized fine dome shaped features within the column surface area correlate to the fibers. The evolution of this complex structure could be related to some phase

segregation taking place on the growth surface and/or in the surface near domain.

- Under our experimental conditions the oxynitride film prepared at varying oxygen concentration exhibit the coexistence of the 001 and 111 textures with crossover between them due to the variation of oxygen concentration according to the AES depth profile analysis. The dark field X_TEM images indicated that the <111> oriented crystals composing the upper part of the film are nucleated on the substrate and survived the first competitive growth regime dominated by the faster growth of <001> oriented crystals due to the high oxygen concentration.

7.2. New scientific results

1. By dedicated experiments and comprehensive structure analysis of $Ti_{0.45}O_{0.20}N_{0.35}$ film I have confirmed and demonstrated the competitive growth mechanism of the 001 texture evolution proposed in the literature. [P1, P3, L1 – L6].
    1.1 I confirmed that in the applied deposition system and deposition parameters (substrate temperature, deposition rate, N and Ar pressure) the undoped TiN films are growing with 111 fiber texture perpendicular to the substrate.
    1.2 By this way I demonstrated unambiguously that the change of the 111 texture to 001 is directly related to the oxygen doping.
2. I have shown at first that one part of incorporated oxygen is present in segregated TiO_2 phase and determined its distribution. [P2, L5, L7].
    2.1 The TiO_2 phase is situated both at the boundaries of the V-shaped TiN single crystal columns and within their bulk.
    2.2 The TiO_2 phase incorporated into the bulk of single crystal columns segregated in discrete fibers parallel to the axes of columns; the fibers are distributed in a honey comb-like network in the cross section of the columns.
3. I concluded that the variation of the 111 texture to 001 at increased oxygen concentration could be related to the different surface chemical interaction of oxygen on the {111} and {001} TiN crystal faces resulting in the faster growth rate of the <001> oriented crystals. The most probable difference could be that on the {001} crystal faces the oxygen is incorporated into the growing crystal lattice by subsurface adsorption while on the {111} faces it is segregated and forms a surface oxide phase limiting the growth of the <111> oriented crystals [P3, L5].

4. By detailed structure analysis of TiN thin films prepared at varied oxygen concentration I could demonstrate at first the crossover between the 001 and 111 textures. [P4, L4, L5, L8].
   4.1 The thickness domain with 20at.% oxygen developed on the substrate is with 001 texture, while the second thickness domain with 11at.% oxygen beyond of that is with 111 texture.
   4.2 Both domains are composed of crystals with V-shape upwards indicating their competitive growth.
   4.3 Between the two domains with textures there is a thickness domains in which both textures coexist but the 001 oriented crystals are with V-shaped morphology down while the 111 oriented crystals are with V-shaped upwards. These morphologies clearly demonstrate that the <001> oriented crystals are deceased and overgrown by the <111> oriented ones. That thickness domain is the crossover between the two textures.
5. I have shown by dark field X-TEM imaging that the <111> oriented crystals present in the upper thickness domain are nucleated on the substrate. I concluded that a crossover between the 001 and 111 textures can develop when the oxygen concentration is decreased at the growth stage at which <111> oriented crystal are still present surviving the first competitive growth regime dominated by faster growing <001> oriented crystals. [P4, L4, L5, L8].

7.3. Publications of our results

7.3.1 Scientific papers

P1. Effect of oxygen doping on the evolution of 001 texture and the crossover between 001 and 111 textures in TiN films,
D. Biró, **M. F. Hasaneen**, L. Székely, M. Menyhárd, S. Gurbán, P. Pekker, Dódony, and P. B. Barna,
Yearbook 2011 for Research Institute for Technical Physics and Materials Science-Hungarian Academy of Sciences.

P2. Substructure in the columnar crystals of the $Ti_{0.45}O_{0.2}0N_{0.35}$ Oxynitride thin film
M.F. Hasaneen, D. Biro, L. Székely, P. Nemes-Incze1and P.B. Barna,
Vacuum, 86 (2012)2105-2108.

P3. Evolution of the 001 texture in $Ti_{0.45}O_{0.2}0N_{0.35}$ oxynitride thin film
D. Biro, **M.F Hasaneen**, L. Székely, M. Menyhárd, S. Gurbán, P. Pekker, I. Dódony, P.B. Barna,
in preparation.

P4. Development of the crossover between 001 and 111 textures in TiN films due to the variation of oxygen concentration

D. Biro, **M.F Hasaneen**, L. Székely, M. Menyhárd, S. Gurbán, P. Pekker, I. Dódony, P.B. Barna,
in preparation.

7.3.2. Lectures presented at conferences

L1. Influence of Oxygen doping on titanium nitride thin films prepared by DC magnetron sputtering,
M. F. Hasaneen,
International workshop for PhD student, Austria, Vienna, 2 May 2011.

L2. Effect of oxygen doping on the structure evolution of TiN thin film,
M.F. Hasaneen, D. Biro, L. Székely, M. Menyhárd, S. Gurbán, P. Pekker, I. Dódony, P.B. Barna,
International workshop for PhD student, Prague, Czech Republic, 2 May 2012.

L3. Effect of oxygen on the structure evolution of TiN thin films deposition by unbalanced magnetron sputtering,
M.F. Hasaneen, D. Biro, L. Székely, M. Menyhárd1, S. Gurbán, P. Pekker, I. Dódony, P.B. Barna,
Hungarian National Conference on Microscopy, SIÓFOK, LAKE BALATON, 10-12 May 2012.

L4. Effect of oxygen doping on the evolution of 001 texture and the crossover between 001 and 111 textures in TiN films,
D. Biro, **M.F. Hasaneen**, L. Székely, M. Menyhárd, S. Gurbán, P. Pekker, I. Dódony, P.B. Barna,
International conference on thin film physics, JVC-14/ EVC-12/AMDVG-11/CroSloVM-19 Conference, Dubrovnik, Croatia, 04-08 June 2012.

L5. The role of dopants in the formation of nanograin Thin Film Materials**,**
P.B. Barna, D. Biro, F. Misják, **F.M. Hasaneen,** L. Székely, G. Radnóczi,
The 67th IUVSTA Workshop "High temperature amorphous and nanostructure ceramic coating: challenges and opportunities" CERAMAX) in Manchester, 23-27 September, 2012.

L6. Evolution of 001 texture under effect of oxygen concentration,
D. Biro, **M.F Hasaneen**, L. Székely, M. Menyhárd, S. Gurbán, P. Pekker, I. Dódony, P.B. Barna,
International workshop for PhD student, Austria, Vienna, May 2013.

L7. Substructure in the columnar crystals of the $Ti_{0.45}O_{0.20}N_{0.35}$ oxynitride thin film,
M.F. Hasaneen, D. Biro, L. Székely, P. Nemes-Inczeand P.B. Barna,
Hungarian National Conference on Microscopy, SIÓFOK, LAKE BALATON, 23-26 May 2013.

L8. Crossover between the 001 and 111 textures in TiN hard coatings related to the variation of the oxygen concentration,

D. Biro, **M.F. Hasaneen**, L. Székely, M. Menyhárd, S. Gurbán P. Pekker, I. Dódony, P.B. Barna,
Hungarian National Conference on Microscopy, SIÓFOK, LAKE BALATON, 23-26 May 2013.

Acknowledgment

First and foremost, all praise is due to Allah, who gave me the opportunity, strength, and patience to carry out this work.

I would like to offer my heartfelt thanks to my supervisor Professor Péter Barna for his support and expert guidance throughout my time here. I would also to thank Professor Biró Domokos for his advance on sample preparation.

I pleasure to thank Dr. Zs. J. Horváth (MTA TTK) for carrying out the XRD analysis, Dr. M. Menyhárd and S. Gurbán (MTA TTK) for performing the AES and XPS analysis and Dr. N.Q. Chinh, (Department of Materials Physics, Eötvös Loránd University, Budapest) for the microhardness measurements. P. Pekker Bay Zoltán Nonprofit Ltd, Miskolc and professor I. Dódony Eötvös Loránd University Department of Mineralogy for carrying out the PED ASTAR investigation

It has been my privilege to be a member of the Thin Film Physics Group in the Research Institute for Technical Physics and Materials Sciences.

Many thanks for all my friends and colleagues in Hungary and also in Egypt, they played a very important role in my life.

The last, but the most important thanks to my family: my wife, my daughter and my son for their love, also for keeping me in their prayers.

This work is supported by cooperation between Hungarian and Egyptian scholarship